Electronic Properties of Various Two-Dimensional Materials

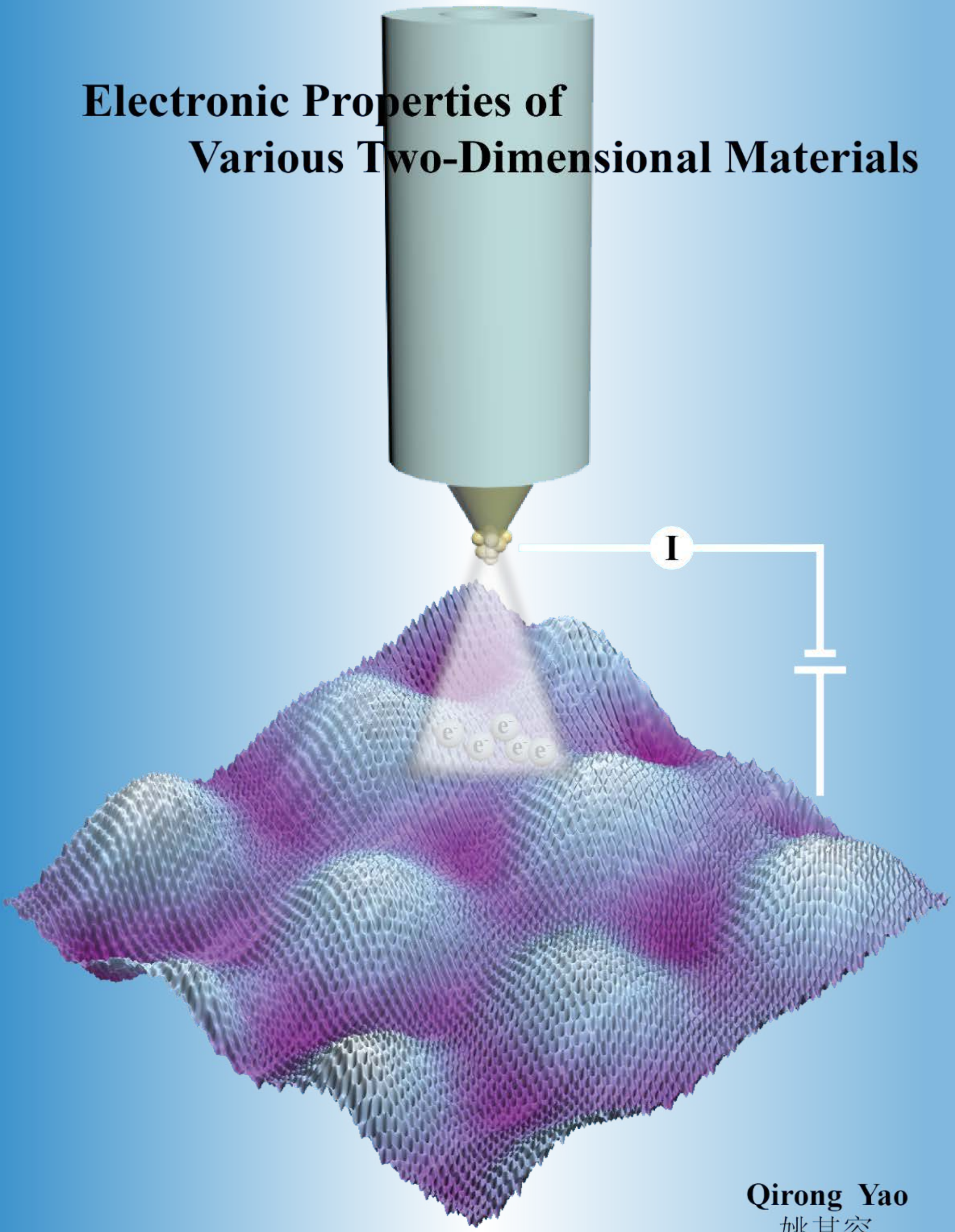

Qirong Yao
姚其容

ELECTRONIC PROPERTIES OF VARIOUS TWO-DIMENSIONAL MATERIALS

Qirong Yao

Graduation Committee:

Chairman / secretary:	Prof. dr. J.L. Herek
Supervisor:	Prof. dr. ir. H.J.W. Zandvliet
Committee Members:	Prof. dr. M.A. Stöhr
	Prof. dr. O. Gurlu
	Prof. dr. ir. J.W.M. Hilgenkamp
	Prof. dr. ir. J.E. ten Elshof
	Dr. A. van Houselt

ELECTRONIC PROPERTIES OF VARIOUS TWO-DIMENSIONAL MATERIALS

DISSERTATION

to obtain
the degree of doctor at the Universiteit Twente,
on the authority of the rector magnificus,
Prof.dr. T.T.M. Palstra,
on account of the decision of the graduation committee
to be publicly defended
on Wednesday 11 September 2019 at 12.45

by

Qirong Yao

born on 16 October 1989
in Hubei, China

This dissertation has been approved by the supervisor:
Prof. dr. ir. H.J.W. Zandvliet

Cover design: Qirong Yao

Printed by: Gildeprint drukkerijen, Enschede, The Netherlands.

ISBN: 978-90-365-4846-5

DOI: 10.3990/1.9789036548465

Contents

1 Introduction 1
  1.1 Preamble 1
  1.2 graphene and other 2D materials 2
  1.3 Modification of electronic structure in 2D materials 3
    1.3.1 thickness and stacking 3
    1.3.2 Intrinsic defects 4
    1.3.3 Chemical functionalization 5
  1.4 Motivation 5
  1.5 Outline 6
2 Experimental Methods 12
  2.1 Scanning tunneling microscopy 12
    2.1.1 The basic principle 12
    2.1.2 Scanning tunneling spectroscopy 13
    2.1.3 Omicron STM-1 14
  2.2 Conductive Atomic Force Microscopy 15
3 Moiré band structure in twisted graphene 17
  3.1 Introduction 17
  3.2 Experimental and calculation details 18
  3.3 Spatial resolved electronic structure of twisted graphene 19
  3.4 Conclusions 26
4 Intercalation of silicon in transition metal dichalcogenides 30
  4.1 Introduction 30
  4.2 Experimental details 31
  4.3 Growth of silicon on tungsten diselenide 31
  4.4 Conclusions 36
5 Effect of substrate and hydrogenation on germanene 42
  5.1 Introduction 42
    5.1.1 Charge inhomogeneities in 2D material 42
    5.1.2 From germanene to germanane 43
  5.2 Experimental details 44
    5.2.1 Growth of germanene on MoS_2 44
    5.2.2 Hydrogenation of germanene terminated on Ge_2Pt nanocrystal 45
  5.3 Charge puddles in germanene 45
  5.4 Bandgap opening in hydrogenated germanene 50

5.5 Conclusions 54
6 Impact of defects and air-stability on $HfSe_2$ 60
6.1 Introduction 60
6.2 Experimental Details 61
6.3 Surface topography and local electronic properties 62
6.4 Schottky barrier height and Fermi level pinning of the $HfSe_2$ crystal 68
6.5 Effect of oxidation on $HfSe_2$ Surface 72
6.6 Conclusions 74
7 Conclusions and Outlook 80
7.1 General conclusions 80
7.2 Outlook and recommendations 81
7.2.1 Twisted graphene 81
7.2.2 Germanene 82
Summary 84
Samenvatting 87
List of publications 90
Acknowledgements 91

Introduction

1.1 Preamble

Graphene, a single layer of carbon atoms packed in a honeycomb structure, was isolated from graphite for the first time by Andre Geim and Konstantin Novoselov in 2004.[1] Due to the excellent electrical, thermal, and mechanical properties, graphene has been widely explored in various areas of physical and chemical applications, including electronic devices, chemical sensors, catalysis, batteries and other energy conversion systems.[2-5] The discovery of graphene opens the door to a total new research field and sets off the continuous waves on the vigorous scientific research of two-dimensional (2D) materials.[6-9] The family of 2D materials involves, metals, semimetals, semiconductors, insulators and even superconductors as shown in Figure 1.1.[10] Among them, most conventional 2D materials have been derived from a limited library of bulk solids consisting of stacked, weakly bound sheets (for example, graphite, MoS_2, hexagonal boron nitride and black phosphorus). In contrast, the growth of an entirely new class of synthetic 2D materials, such as silicene, germanene and stanene, expands the variety of materials with new, tailorable properties based on their composition and substrate.[11-13]

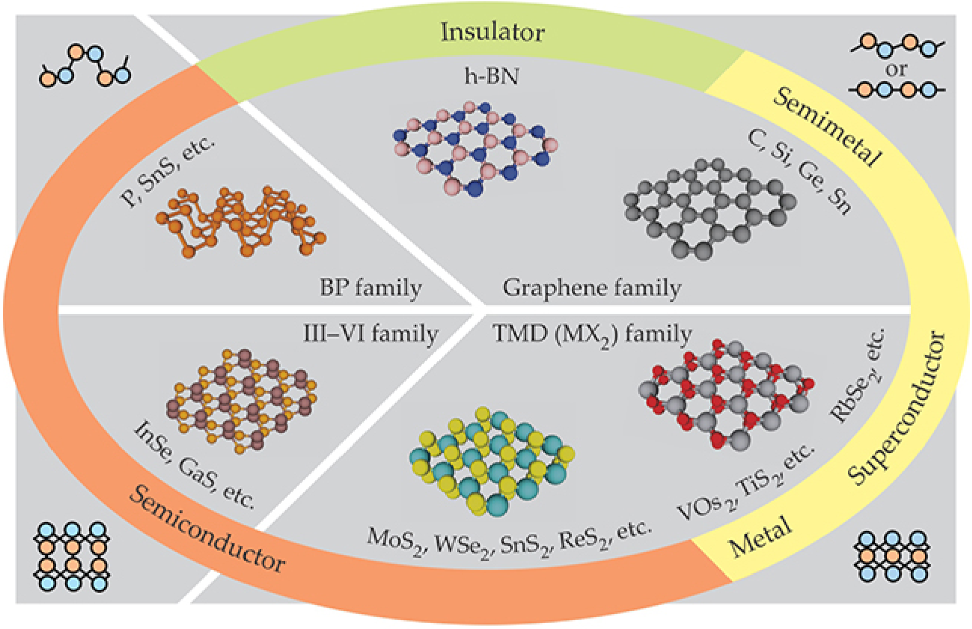

Figure 1.1: The family of two-dimensional materials[10]

1.2 graphene and other 2D materials

Graphene, a monolayer of sp^2 hybridized carbon atoms arranged in honeycomb structure, is shown in Figure 1.2a. The honeycomb lattice of graphene consists of two sub-lattices with a lattice constant of 2.46 Å, while the C-C distance is a=1.42 Å. Graphene is a two-dimensional Dirac material. The electrons in graphene behave as massless relativistic particles obeying the Dirac equation, i.e. the relativistic variant of the *Schrödinger* equation.[2, 14] In the vicinity of the Fermi energy level, the dispersion relation of the electrons is linear resulting in a cone-like band structure referred to as a Dirac cone.

Silicene and germanene, i.e. the silicon and germanium analogues of graphene, are 2D buckled Dirac materials.[12, 15-17] Similar to graphene, the electrons in silicene and germanene near the Fermi energy level also behave as the massless relativistic Dirac fermions. The π and $\pi*$bands are linear and cross at the Fermi level and therefore silicene and germanene are both semimetals. Silicene and germanene exhibit a combined sp^2-sp^3 hybridization, rather than a perfect sp^2 bonding as in graphene. Figure 1.2b shows this honeycomb structure and the buckled nature, where one half of the atoms of the unit cell is located in a lower plane and the other half is located in a higher plane. Each Si (Ge) atom is covalently bonded with three other Si (Ge) atoms, resulting in a simple hexagonal unit cell. The predicted buckling of silicene and germanene is 0.44 Å and 0.64 Å, respectively.[15] Buckled silicene and germanene are stable, whereas perfectly planar silicene and germanene sheets have imaginary phonon modes in a large portion of the Brillouin zone and are therefore not stable. Another difference with graphene is that silicene and germanene have a much larger spin-orbit coupling owing to their larger atomic number.

The spin-orbit gap of silicene and germanene has been calculated to be ~1.5 meV and 24 meV respectively, which is much larger than that of graphene (only a few μeV).[18, 19]

Since the absence of a bandgap in graphene limits its application in the semiconductor industry, the layered transition metal dichalcogenides (TMDs) have received quite some attention during the last decade.[20-22] The formula for transition metal dichalcogenides is MX_2, where M refers to a transition metal atom and X to a chalcogen atom. TMDs consist of a hexagonal packed layer of M atoms sandwiched by two layers of X atoms. The intralayer M-X bonds are predominantly covalent in nature, whereas the sandwiched layers are coupled by weak van der Waals forces. The structure model is shown in Figure 1.2c. The semiconducting 2D TMDs, including MoS_2, $MoSe_2$, $MoTe_2$, WS_2, WSe_2 and $HfSe_2$, have emerged as promising materials for a wide range of applications.[22, 23]

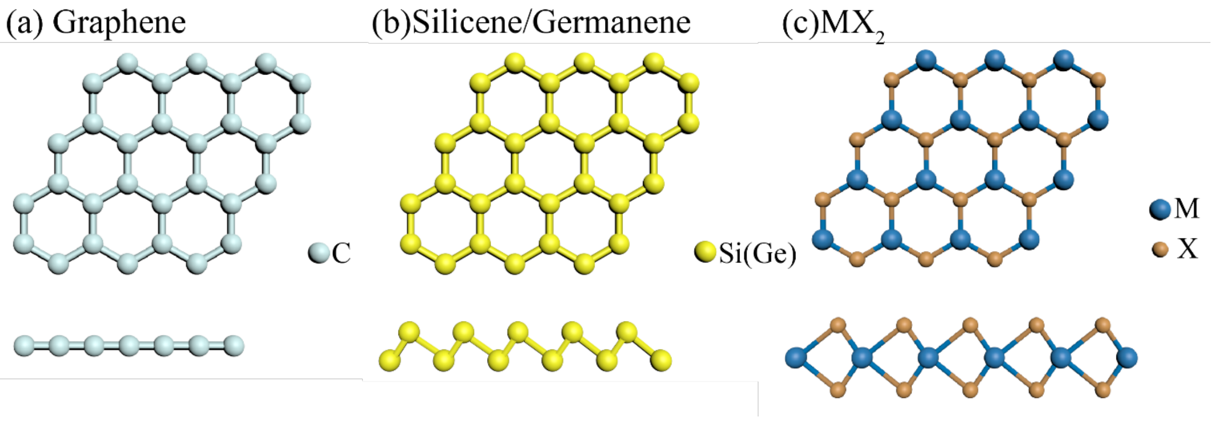

Figure 1.2: Structural models of graphene in (a), silicene/germanene in (b), and MX_2 in (c).

1.3 Modification of electronic structure in 2D materials

1.3.1 thickness and stacking

In 2D materials, both the thickness as well as the stacking order of the 2D flake affects the electronic band structure. The properties of 2D materials are a function of the number of layers. For example, a single-layer graphene has linearly dispersing energy bands resulting in a perfect Dirac cone, but for a Bernal stacked bilayer of graphene the energy bands are parabolic in the direct vicinity of the Dirac point [2, 24]. The Bernal stacked bilayer corresponds to a twist angle of 0 degrees. For small twist angles the two Dirac cones of both graphene layers move towards each other in reciprocal space resulting in hybridization and the formation of Van Hove singularities.

The transition metal dichalcogenides behave differently. For instance, bulk MoS_2 has an indirect band gap of 1.29 eV. However, when it is thinned to a monolayer, the crystal transfers into a direct bandgap semiconductor.[25] A strong photoluminescence emerges in the monolayer MoS_2.[26] Black phosphorus has an intrinsic thickness-dependent direct band gap. The band gap varies from 0.3 eV for bulk to 2.0 eV for a monolayer, which covers a broad range of the solar spectrum and consequently makes this material suitable for numerous optoelectronic applications.[27, 28]

Stacking is also a powerful approach to tailor the electronic properties of 2D materials. When two monolayers of 2D materials are stacked on top of each other to create a bilayer structure, their lattices do not necessarily align with each other. For example, in the most energetically favorable form of bilayer graphene, the layers are shifted over the length of one carbon–carbon bond with respect to each other. This combination is known as AB or Bernal stacked form. On the other hand, AA stacking where two layers are exactly aligned or a twisted structure where one layer is rotated relative to the other is also possible. When a third layer is added to the top of AB stacked bilayer graphene it can align with the bottom layer to create an ABA stacked trilayer graphene or it can be shifted one more carbon–carbon bond length and create an ABC stacked trilayer graphene. ABA and ABC stacked forms of trilayer graphene display qualitatively different electronic properties.[29-31] The dispersion of ABA trilayer is a combination of the linear dispersion of a single layer graphene and the quadratic relation of bilayer graphene; whereas the dispersion of ABC trilayer is approximately cubic, with its conductance and valence bands touching at a point close to the highly symmetric K- and K' -points. By applying an external electric field, a large band gap can be formed in the trilayer graphene with the ABC stacking order rather than the ABA stacking order. Especially, twisted bilayer graphene can result in the large moiré superlattices accompanied by new phenomena, such as stacking-dependent Van Hove singularities near the Fermi energy, unconventional superconductivity and insulating behavior.[32-34] In bilayer MoS_2, proper manipulation of stacking orders can break the inversion symmetry and suppress interlayer hopping, introducing strong valley and spin polarizations that cannot be achieved in natural MoS_2 bilayers with Bernal stacking.[35, 36] Furthermore, flat bands at the valence band edge of twisted bilayer TMDs (MoS_2, WS_2, $MoSe_2$, WSe_2) are predicted to occur.[37]

1.3.2 Intrinsic defects

Atomic defects, such as edges, vacancies, and lattice disorder are localized heterogeneities that can be formed without perturbing the native lattice structure of 2D materials. Defects and vacancies are ubiquitous in 2D materials and can have a significant impact on the electrical properties of these materials. Take graphene as an example, when scrutinized over large-scales it contains point defects, edges, and grain boundaries. The point defects give rise to localized states near the Fermi level, leading to protrusions in STM images.[38] They also act as scattering centers for electron waves. Thus, one can anticipate that these defects will result in the reduction of electronic mobility of graphene.[39] Some vacancy-type and Stone-Wales defects can open a local bandgap (up to 0.3 eV) in graphene.[40] For the grain boundaries, they can suppress the conductivity of both the electron and hole-type charge carriers and trigger a local-doping effect in graphene. In monolayer MoS_2, sulfur vacancies are the most common defects during exfoliation or chemical vapor deposition growth. These sulfur vacancies can introduce unpaired electrons in the lattice and consequently make the material be n-doped. If the material is sulfur atom rich or the molybdenum atom poor, the material exhibits p-type behavior. The grain boundaries in MoS_2 can be either sulfur-deficient or molybdenum-deficient, so it means the in-plane electrical conductivity can be modulated by such kind of defects.[41]

1.3.3 Chemical functionalization

Chemical functionalization is in general an efficient way to tune the electronic properties of 2D materials. Particularly, hydrogenation of 2D materials has shown to be a promising method.[42-45] In principle, when the graphene surface in hydrogenated, it will change the hybridization of carbon atoms from sp^2 to sp^3, thus removing the conducting π-bands and opening up an energy gap. It has also been show that a superlattice structure of graphene-like islands by patterned adsorption of atomic hydrogen onto a moiré superlattice of graphene grown on an Ir(111) substrate can induce a bandgap in the electronic band structure due to confinement.[43] As mentioned before, the sulfur vacancies in MoS_2 flakes can cause the presence of unsaturated electrons in the surrounding molybdenum atoms and act as electrons donors, which is responsible for the n-type doping of MoS_2. By exposing a single layer MoS_2 to atomic hydrogen at room temperature, hydrogen atoms will passivate sulfur vacancies and consequently the electronic properties of single layer MoS_2 can be tuned from intrinsic electron (n) to hole (p) doping without degrading the quality of MoS_2 flakes.[44] Furthermore, by employing first-principles calculations, it has been found that the intrinsic bilayer silicene can be transferred from a semiconductor with an indirect band gap to a direct-gap semiconductor with a widely tunable band gap (from 1 to 1.5 eV) by hydrogenation, which is suitable for solar applications.[45]

1.4 Motivation

Measuring the physical properties of 2D materials and correlating the spatial variation of these physical properties to the structure provides a route to better understand these materials. A very powerful tool for probing the surface structure and local electronic properties is scanning tunneling microscopy. Scanning tunneling spectroscopy allows the observation of electronic spectral properties with a resolution down to the atomic scale. In this thesis, we mainly employed scanning tunneling microscopy and scanning tunneling spectroscopy to study the structure and electronic properties of different types of 2D materials. Such fundamental research can help us to understand the 2D materials at the nano-scale, and pave the way towards the application of these materials in future electronic devices.

1.5 Outline

The following chapter describes the experimental techniques that have been used in this thesis. Chapter 3 deals with the structural and electronic properties of twisted graphene. We show that for small twist angles the electronic structure in the vicinity of the Dirac point alters significantly. Two Van Hove singularities form, one located just below the Dirac point and one located just above the Dirac point. Spatial maps of the local density of states reveals a honeycomb structure, which is composed of two sub-lattices.

In Chapter 4 the growth of silicon on TMDs surfaces is studied. Unfortunately, we found that it is not possible to grow silicene on TMD substrates. The deposited silicon atoms do not reside on the TMD surface, but rather intercalate between the TMD sheets.

Chapter 5 deals with the growth and characterization of germanene on different substrates. We show that electron-hole puddles are present in the germanene on MoS_2 system. Furthermore, we also show that the band structure of germanene can be modified by chemical functionalization. The adsorption of hydrogen on germanene results in the formation of a sizeable bandgap of ~0.5 eV. In Chapter 6 we show and explain why the charge mobilities in $HfSe_2$ are so low. In addition, we also elaborate stability of $HfSe_2$ at ambient conditions.

We end this thesis with conclusions and an outlook.

Bibliography

[1] Novoselov, K. S.; Geim, A. K.; Morozov, S. V.; Giacometti, V.; Jiang, D.; Zhang, Y.; Dubonos, S. V.; Grigorieva, I. V.; Firsov. A. A. Electric Field Effect in Atomically Thin Carbon Films. *Science* **2004**, *306*, 666-669.

[2] Castro Neto, A. H.; Guinea, F.; Peres, N. M. R.; Novoselov, K. S.; Geim, A. K. The Electronic Properties of Graphene. *Rev. Mod. Phys.* **2009**, *81*, 109-162.

[3] Shao, Y.; Wang, J.; Wu, H.; Liu, J.; Aksay, I. A.; Lin, Y. Graphene Based Electrochemical Sensors and Biosensors. *Electroanalysis* **2010**, *22*, 1027-1036.

[4] Bonaccorso, F.; Colombo, L.; Yu, G.; Stoller, M.; Tozzini, V.; Ferrari, A. C.; Ruoff, R. S.; Pellegrini, V. Graphene, Related Two-Dimensional Crystals, and Hybrid Systems for Energy Conversion and Storage. *Science* **2015**, *347*, 1246501.

[5] Huang, X.; Yin, Z.; Wu, S.; Qi, X.; He, Q.; Zhang, Q.; Yan, Q.; Boey, F.; Zhang, H. Graphen-Based Materials: Synthesis, Characterization, Properties, and Applications. *Small* **2011**, *7*, 1876-1902.

[6] Xu, M.; Liang, T.; Shi, M.; Chen, H. Graphene-Like Two-Dimensional Materials. *Chem. Rev*. **2013**, *113*, 3766-3798.

[7] Butler, S. Z.; Hollen, S. M.; Cao, L.; Cui, Y.; Gupta, J. A.; Gutierrez, H. R.; Heinz, T. F.; Hong, S. S.; Huang, J.; Ismach, A. F., et al. Progress, Challenges, and Opportunities in Two-Dimensional Materials Beyond Graphene. *ACS Nano* **2013**, *7*, 2898-2926.

[8] Lv, R.; Robinson, J. A.; Schaak, R. E.; Sun, D.; Sun, Y.; Mallouk, T. E.; Terrones, M. Transition Metal Dichalcogenides and Beyond: Synthesis, Properties, and Applications of Single- and Few-Layer Nanosheets. *Acc. Chem. Res.* **2015**, *48*, 56-64.

[9] Liu, H.; Du, Y.; Deng, Y.; Ye, P. D. Semiconducting Black Phosphorus: Synthesis, Transport Properties and Electronic Applications. *Chem. Soc. Rev.,* **2015**, *44*, 2732-2743.

[10] Ajayan, P.; Kim, P.; Banerjee, K. Two-Dimensional Van der Waals Materials. *Phys. Today* **2016**, *69*, 38.

[11] Kara, A.; Enriquez, H.; Seitsonen, A. P.; Lew Yan Voon L. C.; Vizzini, S.; Aufray, B.; Oughaddou, H. A Review on Silicene — New Candidate for Electronics. *Surf. Sci. Rep.* **2012**, *67*, 1-18.

[12] Acun, A.; Zhang, L.; Bampoulis, P.; Farmanbar, M.; Houselt, A. V.; Rudenko, A. N.; Lingenfelder, M.; Brocks, G.; Poelsema, B.; Katsnelson, M. I.; Zandvliet, H. J. W. Germanene: the Germanium Analogue of Graphene. *J. Phys.: Condens. Matter* **2015**, *27*, 443002.

[13] Zhu, F.; Chen, W.; Xu, Y.; Gao, C.; Guan, D.; Liu, C.; Qian, D.; Zhang, S.; Jia, J. Epitaxial Growth of Two-Dimensional Stanene. Nat. Mater. **2015**, *14*, 1020-1025.

[14] Geim, A. K. Graphene: Status and Prospects. *Science* **2009**, *324*, 1530-1534.

[15] Cahangirov, S.; Topsakal, M.; Aktürk, E.; Şahin, H.; Ciraci, S. Two- and One-Dimensional Honeycomb Structures of Silicon and Germanium. *Phys. Rev. Lett.* **2009**, *102*, 236804.

[16] Molle, A.; Goldberger, J.; Houssa, M.; Xu, Y.; Zhang, S.; Akinwande, D. Buckled Two-Dimensional Xene Sheets. Nat. Mater. **2017**, *16*, 163-169.

[17] Fleurence, A.; Friedlein, R.; Ozaki, T.; Kawai, H.; Wang, Y.; Yamada-Takamura, Y. Experimental Evidence for Epitaxial Silicene on Diboride Thin Films. *Phys. Rev. Lett.* **2012**, *108*, 245501.

[18] Liu, C.; Feng, W.; Yao, Y. Quantum Spin Hall Effect in Silicene and Two-Dimensional Germanium. *Phys. Rev. Lett.* **2011**, *107*, 076802.

[19] Sichau, J.; Prada, M.; Anlauf, T.; Lyon, T. J.; Bosnjak, B.; Tiemann, L.; Blick, R.H. Resonance Microwave Measurements of an Intrinsic Spin-Orbit Coupling Gap in Graphene: A Possible Indication of a Topological State. *Phys. Rev. Lett.* **2019**, 122, 046403.

[20] Chhowalla, M.; Shin, H. S.; Eda, G.; Li, L.; Loh, K. P.; Zhang, H. The Chemistry of Two-Dimensional Layered Transition Metal Dichalcogenide Nanosheets. *Nat. Chem*. **2013**, *5*, 263-275.

[21] Johari, P.; Shenoy, V. B. Tuning the Electronic Properties of Semiconducting Transition Metal Dichalcogenides by Applying Mechanical Strains. *ACS Nano* **2012**, *6*, 5449-5456.

[22] Duan, X.; Wang, C.; Pan, A.; Yu, R.; Duan, X. Two-Dimensional Transition Metal Dichalcogenides as Atomically Thin Semiconductors: Opportunities and Challenges. *Chem. Soc. Rev.*, **2015**, *44*, 8859-8876.

[23] Mleczko, M. J.; Zhang, C.; Lee, H. R.; Kuo, H.; Magyari-Köpe, B.; Moore, R. G.; Shen, Z.; Fisher, I. R.; Nishi, Y.; Pop, E. $HfSe_2$ and $ZrSe_2$: Two-dimensional Semiconductors with Native High-κ Oxides. *Sci. Adv*. **2017**, *3*, e1700481.

[24] Ohta, T.; Bostwick, A.; McChesney, J. L.; Seyller, T.; Horn, K.; Rotenberg, E. Interlayer Interaction and Electronic Screening in Multilayer Graphene Investigated with Angle-Resolved Photoemission Spectroscopy. *Phys. Rev. Lett.* **2007**, *98*, 206802.

[25] Mak, K. F.; Lee, C.; Hone, J.; Shan, J.; Heinz, T. F. Atomically Thin MoS_2: A New Direct-Gap Semiconductor. *Phys. Rev. Lett.* **2010**, *105*, 136805.

[26] Splendiani, A.; Sun, L.; Zhang, Y.; Li, T.; Kim, J.; Chim, C.; Galli, G.; Wang, F. Emerging Photoluminescence in Monolayer MoS_2. *Nano Lett.* **2010,** *10*, 1271–1275.

[27] Qiao, J.; Kong, X.; Hu, Z.; Yang, F.; Ji, W. High-Mobility Transport Anisotropy and Linear Dichroism in Few-Layer Black Phosphorus. *Nat. Commun.* **2014**, *5*, 4475.

[28] Li, L.; Yu, Y.; Ye, G. J.; Ge, Q.; Ou, X.; Wu, H.; Feng, D.; Chen, X. H.; Zhang, Y. Black Phosphorus Field-Effect Transistors. *Nat. Nanotechnol.* **2014,** *9*,372–377.

[29] Lui, C. H.; Li, Z.; Mak, K. F.; Cappelluti, E.; Heinz, T. F. Observation of An Electrically Tunable Band Gap in Trilayer Graphene. *Nat. Phys.* **2011**, *7*, 944-947.

[30] Craciun, M. F.; Russo, S.; Yamamoto, M.; Oostinga, J. B.; Morpurgo, A. F.; and Tarucha, S. Trilayer Graphene is A Semimetal with a Gate-Tunable Band Gap. *Nat. Nanotechnol.* **2009,** *4,* 383–388.

[31] Bao, W.; Jing, L.; Jr, J. V.; Lee, Y.; Liu, G.; Tran, D. et al., Stacking-Dependent Band Gap and Quantum Transport in Trilayer Graphene. *Nat. Phys.* **2011,** *7,* 948–952.

[32] Li, G.; Luican, A.; Lopes dos Santos, J. M. B.; Castro Neto, A. H.; Reina, A.; Kong, J.; Andrei, E. Y. Observation of Van Hove Singularities in Twisted Graphene Layers. *Nat. Phys.* **2010**, *6*, 109–113.

[33] Cao, Y.; Fatemi, V.; Fang, S.; Watanabe, K.; Taniguchi, T.; Kaxiras, E.; Jarillo-Herrero, P. Unconventional Superconductivity in Magic-Angle Graphene Superlattices. *Nature* **2018,** *556*, 43–50.

[34] Cao, Y.; Fatemi, V.; Demir, A.; Fang, S. et. al., Correlated Insulator Behaviour at Half-Filling in Magic-Angle Graphene Superlattices *Nature* **2018**, *556*, 80-84.

[35] Wu, S.; Ross, J. S.; Liu, G.; Aivazian, G.; Jones, A.; Fei, Z.; Zhu, W.; Xiao, D.; Yao, W.; Cobden, D.; Xu, X. Electrical Tuning of Valley Magnetic Moment Through Symmetry Control in Bilayer MoS_2. *Nat. Phys***. 2013**, *9*, 149–153.

[36] Liu, K.; Zhang, L.; Cao, T.; Jin, C.; Qiu, D.; Zhou, Q.; Zettl, A.; Yang, P.; Louie, S. G.; Wang, F. Evolution of Interlayer Coupling in Twisted Molybdenum Disulfide Bilayers. *Nat. Commun.* **2014**, *5,* 4966.

[37] Naik, M. H.; Jain, M. Ultraflatbands and Shear Solitons in Moiré Patterns of Twisted Bilayer Transition Metal Dichalcogenides. *Phys. Rev. Lett.* **2018**, *121*, 266401.

[38] Ugeda, M. M.; Ferna´ndez-Torre, D.; Brihuega, I.; Pou, P.; Martı´nez-Galera, A. J.; Pe´rez, R.; Go´mez-Rodrı´guez, J. M. Point Defects on Graphene on Metals. *Phys. Rev. Lett.* **2011**, *107,* 116803.

[39] Chen, J.; Cullen, W. G.; Jang, C.; Fuhrer, M.S.; Williams, E. D. Defect Scattering in Graphene. *Phys. Rev. Lett.* **2009,** *102*, 236805.

[40] Banhart, F.; Kotakoski, J.; Krasheninnikov, A. V. Structural Defects in Graphene. *ACS Nano*, **2011**, *5*, 26-41.

[41] Lin, Z.; Carvalho, B. R.; Kahn, E.; Lv, R.; Rao, R.; Terrones. H.; Pimenta, M. A.; Terrones, M. Defect Engineering of Two-Dimensional Transition Metal Dichalcogenides. *2D Mater*. **2016**, *3*, 022002.

[42] Elias, D. C.; Nair, R. R.; Mohiuddin, T. M. G.; Morozov, S. V.; Blake, P.; Halsall, M. P.; Ferrari, A. C.; Boukhvalov, D. W.; Katsnelson, M. I.; Geim, A. K.; Novoselov, K. S. Control of Graphene’s Properties by Reversible Hydrogenation: Evidence for Graphane. *Science* **2009**, *323*, 610-613.

[43] Balog, R.; Jørgensen, B.; Nilsson, L.; Andersen, M. et al., Bandgap Opening in Graphene Induced by Patterned Hydrogen Adsorption. *Nat. Mater.* **2010**, *9*, 315–319.

[44] Pierucci, D.; Henck, H.; Aziza, Z. B.; Naylor, C. H. et al., Tunable Doping in Hydrogenated Single Layered Molybdenum Disulfide. *ACS Nano* **2017**, *11*, 1755−1761.

[45] Huang, B.; Deng, H.; Lee, H.; Yoon, M.; Sumpter, B. G.; Liu, F.; Smith, S. C.; Wei, S. Exceptional Optoelectronic Properties of Hydrogenated Bilayer Silicene. *Phys. Rev. X* **2014**, *4*, 021029.

Experimental Methods

2.1 Scanning tunneling microscopy

The scanning tunneling microscopy (STM) was invented by G. Binnig and W. Rohrer at the IBM Research Laboratory in 1982,[1, 2]. The inventers of the STM received the Nobel Prize in Physics in 1986. It has been widely used as an instrument for real space analysis in surface science and related research fields. The STM can provide a lateral resolution of 0.1 nm and a vertical resolution of 0.01 nm. Since STM relies on quantum mechanical tunneling the technique only allows to study conducting substrates, such as metals and semiconductors. Not only the structural, but also the electronic properties can be obtained by STM measurements with an unprecedented spatial resolution. It has to be emphasized here that an STM image cannot just be interpreted as a topographic map because the tunneling current is influenced by local density of states at the surface.

2.1.1 The basic principle

The basic idea of an STM is to bring a sharp metallic tip in close proximity (a few Å) to a sample, and apply a small bias between tip and substrate such that a small tunnel current (0.01-50 nA) starts to flow from the tip to the sample or vice versa. Figure 2.1a displays a schematic diagram of an STM. There is no physical contact between the tip and the substrate and electrons simply *tunnel* through a thin vacuum barrier with a width of about 1 nm and a barrier height of a few eVs.

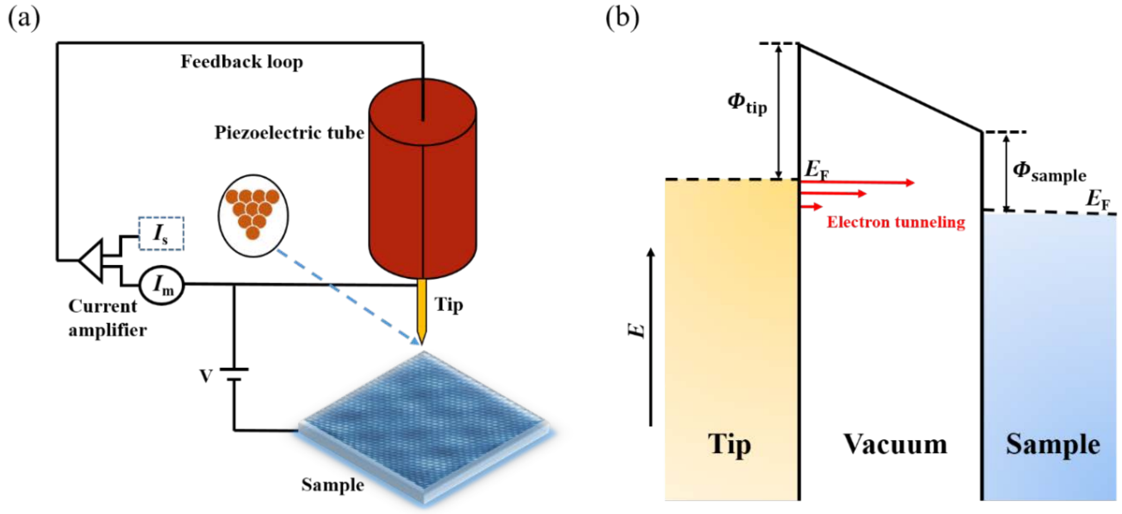

Figure 2.1: (a) Schematic diagram of an STM (b) Energy diagram of an STM tunnel junction.

While the tip is scanned across the substrate the tunnel current is kept constant by continuously adjusting the tip-substrate distance using a piezo (see Figure 2.1a). Let us consider an electron wave with wave function $\Psi_{(\mathrm{x})}$ and energy E that encounters a potential barrier of height Φ. The wave function of the electron satisfies the Schrödinger equation,

$$\frac{-\hbar^2}{2m}\frac{\partial^2\Psi_{(\mathrm{x})}}{\partial x} = (E - \Phi)\Psi_{(\mathrm{x})}, \qquad (1)$$

where $\hbar$ is the reduced Planck's constant, m is the mass of the electron and x the position. If the barrier is higher than the energy of the incoming electron the solution of the wave function is given by

$$\Psi_{(\mathrm{x})} = \Psi_{(0)}e^{-\kappa x}, \qquad (2)$$

here, $\kappa = \frac{\sqrt{2m(\Phi-E)}}{\hbar}$ is the inverse decay length. Then the probability (W) of finding the electron just behind the barrier with a width z is given by

$$W_{(\mathrm{z})} = \left|\Psi_{(\mathrm{z})}\right|^2 = \left|\Psi_{(0)}\right|^2 e^{-2\kappa z}. \qquad (3)$$

For the small bias V, the tunneling current I is proportional to the probability of electrons to tunnel through the barrier, as well as the number of electrons in the energy window between $E_f - eV$and E_f,

$$I \propto \sum_{E_f-eV}^{E_f}\left|\Psi_{(0)}\right|^2 e^{-2\kappa z}. \qquad (4)$$

And by definition, summing the probability over an energy range can give the number of states available in this energy range per unit volume, for the energy $\varepsilon \to 0$, the local density of states $\rho(z, E)$ is given by

$$\rho(z, E) = \frac{1}{\varepsilon}\sum_{E_f-\varepsilon}^{E_f}\left|\Psi_{(\mathrm{z})}\right|^2. \qquad (5)$$

Using equations (4) and (5), the tunneling current can be written in terms of LDOS as,

$$I \propto \mathrm{V}\rho(0, E_f)e^{-2\kappa z}. \qquad (6)$$

2.1.2 Scanning tunneling spectroscopy

There are several spectroscopic modes in STM. Here we discuss only the most important modes.

***I(V)* spectroscopy** In this spectroscopic mode the feedback loop of the STM is disabled and the tunneling current, *I*, is measured as a function of sample bias, *V*. Since the feedback loop is disabled it basically means the tip-substrate distance is kept constant while the *I(V)* trace is recorded. In order to reduce the effect to thermal drift *I(V)* are usually recorded within a second.

***dI/dV* spectroscopy** The differential conductance, *dI/dV*, is proportional to the local electronic density of states (LDOS). By measuring the tunneling current as a function of sample bias, i.e. *I(V)*, the LDOS or differential conductivity can be obtained by simply taking numerically differentiating the *I(V)* curve. At negative sample bias, electrons tunnel from surface to tip, which allows to investigate the LDOS of the filled states, while at positive sample bias the electrons tunnel into the empty states of the sample allowing us to investigate LDOS of the empty states of the surface.

Alternatively the differential conductivity can also be obtained by modulating the sample bias with a small sinusoidal voltage and subsequently use a lock-in amplifier to demodulate the tunnel current with the same frequency. The measured lock-in signal is proportional to the differential conductivity. Since in this method the feedback loop remains enabled at all times the differential conductivity can also be measured simultaneously with the standard topographic signal.

***I(z)* spectroscopy** Current-distance spectroscopy is used to determine the barrier height of the tunnel junction. Here, the tunneling current is recorded as the STM tip is approached to or retracted from the surface. The barrier height between tip and surface is extracted by plotting the logarithm of the tunnel current versus the tip-surface distance. The slope of this curve gives the inverse decay length with is proportional to the square root of the barrier height.

2.1.3 Omicron STM-1

All the STM results are measured by a commercially available Omicron STM-1, which is a room temperature ultra-high vacuum STM. The base pressure in the STM chamber is about 3×10^{-11} mbar. This system is mainly made up of three parts, a load-lock, a preparation chamber and an STM chamber. The load-lock is used to quickly transfer the samples from the air to the vacuum system or vice versa. In the preparation chamber we can clean the sample surface by Ar^+ ion sputtering and annealing. In addition, we can also deposit materials via physical vapor deposition. The setup of our Omicron STM-1 system is shown in Figure 2.2.

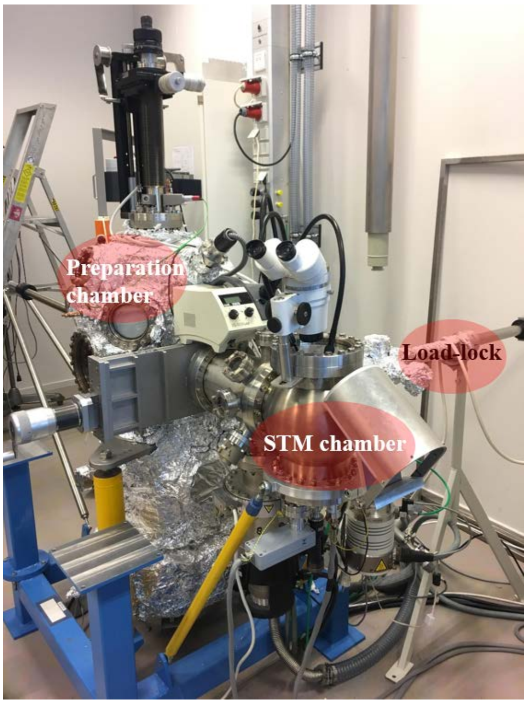

Figure 2.2: The STM-1 system.

2.2 Conductive Atomic Force Microscopy

Conductive atomic force microscopy is developed by Murrel and co-workers at the University of Cambridge in 1993,[3]. Conductive atomic force microscopy (C-AFM) is a very powerful tool to perform nano-scale research of the electrical properties of materials and devices. Unlike in the STM, the topography information in C-AFM is completely separated from the electrical signal. In order to obtain the electrical signal, a voltage is applied between the C-AFM tip and the sample. During the measurement, the cantilever is brought in contact with the sample, referred as the contact mode. The resulting current is recorded by using a highly sensitive amplifier as a current-to-voltage converter. This amplifier should be as close as possible to the tip in order to minimize noise. The two-dimensional currents map can be obtained together with the topographic image. Subsequently, the correlation between the topography and electrical properties of materials can be extracted. In addition, localized single point measurements of the current-voltage curves can also be obtained by the C-AFM. In this case, the cantilever is placed at the desired location on the sample surface and then the current signal is recorded while ramping the bias voltage.

Bibliography

[1] Binnig, G.; Rohrer, H.; Gerber, C.; Weibel, E. Surface Studies by Scanning Tunneling Microscopy. *Phys. Rev. Lett*. **1982**, *49*, 57.

[2] Binnig, G.; Rohrer, H. Scanning Tunneling Microscopy- from Birth to Adolescence. *Rev. Mod. Phys*. **1987**, *59*, 615.

[3] Murrell, M. P.; Welland, M. E.; O’Shea, S. J.; Wong, T. M. H.; Barnes, J. R.; McKinnon, A. W.; Heyns, M.; Verhaverbeke, S. Spatially Resolved Electrical Measurements of SiO_2 Gate Oxides Using Atomic Force Microscopy. *Appl. Phys. Lett.* **1993**, *62*, 786-788.

Moiré band structure in twisted graphene

3.1 Introduction

In 2010 Li *et al.*[1] used scanning tunneling microscopy and spectroscopy to analyze these Van Hove singularities in twisted graphene layers. For small twist angles these authors observed two well-defined Van Hove singularities, one located just above the Fermi level and the other one located just below the Fermi level. The experimentally determined energy separation between these two Van Hove singularities nicely agrees with tight-binding calculations, provided that reasonable assumptions for the hopping integrals are made[1]. In addition, the authors pointed out that the two Van Hove singularities can become asymmetric (in position with respect to the Fermi level and amplitude) due to the presence of an interlayer bias. This interlayer bias is caused by the potential that is applied across the scanning tunneling microscopy junction. In the scanning tunneling microscopy data by Yin et al.[2] a similar asymmetry and shift was found and discussed. Yan et al.[3] studied the angle-dependent Van Hove singularities and found, in contrast to predictions by band structure calculations, that the Fermi velocity is very comparable to the Fermi velocity of monolayer graphene. In a follow-up study Yan et al.[4] showed the breakdown of Van Hove singularities beyond a twist angle of about 3.5°, indicating that the continuum models are no longer applicable at these relatively large twist angles. Yin et al.[5] showed that there is a magic twist angle of 1.11° at which the two Van Hove singularities merge together and form a well-defined peak at the charge neutrality point. In addition to this strong peak at the charge neutrality point, these authors also found a set of regularly spaced peaks. These regularly spaced peaks are confined electronic states in the twisted bilayer graphene. The energy spacing of 70 meV $(= v_F/D)$ agrees well with the periodicity of the moiré pattern. In another study Yin et al.[2] demonstrated that tilt grain boundaries can severely affect the structural and electronic properties of graphene multilayers. They also pointed out that tilt grain boundaries in trilayer graphene can result in the coexistence of massless Dirac fermions and massive chiral fermions. Wong et al.[6] performed local spectroscopy on gate-tunable twisted bilayer graphene. The twisted graphene bilayer was positioned on a hexagonal boron nitride substrate. Wong et al.[6] found, besides the coexistence of moiré patterns and moiré super-superlattices, also a very rich and interesting electronic structure. Despite the fact that the electronic structure of the twisted bilayer graphene has been extensively studied [1–15], the spatial variation of the electronic structure within the unit cell of the moiré pattern did not receive a lot of attention yet.

Here, in this chapter, we have studied the spatial variation of the electronic structure of twisted graphene on highly oriented pyrolytic graphite substrates. In the twisted graphene, we found the development of two Van Hove singularities in the density of states, which is in agreement with the previous studies. Spatial maps of the differential conductivity of the moiré pattern near the Fermi level reveal a honeycomb structure that is comprised of two inequivalent interpenetrating hexagonal sublattices. At large energies, i.e., $|E - E_F| > 0.3$ eV, the difference in the density of states of the two hexagonal sublattices fades away. Here we show that the inequivalence of these two sublattices can be understood if one takes into account a lowering of the symmetry due to the presence of the substrate. We will model this by introducing a third graphene layer. The fact that the spatial variation of the differential conductivity fades away at high energies hints to an electronic instability.

3.2 Experimental and calculation details

The experiments were performed with an ultrahigh vacuum (UHV) scanning tunneling microscope (Omicron). The base pressure of the UHV system is 3×10^{-11} mbar. Before insertion of the ZYA quality highly oriented pyrolytic graphite (HOPG) substrates into the load lock of the UHV system we had removed several graphene layers via mechanical exfoliation using the Scotch-tape method. In order to remove any residual water from the HOPG surfaces, we had baked the load-lock system for 24 h at a temperature of 120 ^{o}C. After cooling down, the samples were transferred to the main chamber and subsequently inserted into the scanning tunneling microscope for imaging.

The scanning tunneling microscopy images were recorded in the constant current mode. Scanning tunneling spectroscopy spectra were recorded in two ways. In the first method we recorded current-voltage (*I(V)*) curves at many locations of the surface with the feedback loop of the scanning tunneling microscope disabled. The *dI/dV* spectra were obtained by numerical differentiation of the I-V traces. In the second method a small sinusoidal voltage with a small amplitude of a few mV and a frequency of 1.9 kHz was added to the bias voltage. A lock-in amplifier was used to record the *dI/dV* signal.

The theoretical calculations for twisted graphene had been performed within the framework of the Slater-Koster tight-binding model, in which we took into account the intralayer and interlayer hoppings between the p_z orbitals. The nearest intralayer hoppings in all layers are fixed as t = 3 eV, and the interlayer hopping between two sites in different layers is given by

$$t_{\perp} = \cos^2\alpha \, V_{\sigma} + \sin^2\alpha \, V_{\pi}, \qquad (1)$$

where the orbital overlap is modeled as function of the angle α between the line connecting the two sites and the normal of the graphene plane, while V_{σ} and V_{π} are Slater-Koster integrals depending on the distance between the two sites. Both V_{σ} and V_{π} decay rapidly when the distance between the two sites is larger than the lattice parameter a_0 = 2.46 Å, and the contribution of V_{π} is negligible in the interlayer hoppings in multilayer graphene[14, 15]. Here we use 0.24 eV as the maximum value of V_{σ} (for two sites with A-A stacking, the same value as used in Ref. [1]), and consider the screening effects following the environment-dependent tight-binding model introduced in Eq. (1) of Ref. [15]. The values of seven parameters fitted for the screening in multilayer graphene are taken from Ref. [15] as α_1 = 6.175, α_2 = 0.762, α_3 = 0.179, α_4 = 1.411, β_1 = 6.811, β_2 = 0.01, and β_3 = 19.176. All the neighboring pairs within a maximum in-plane distance of 2 Å are included in the Hamiltonian. The electronic properties such as the density of states and quasi-eigenstates, which have the real-space profiles comparable to the experimental STM results, are calculated by using the tight-binding propagation method (TBPM)[16, 17]. TBPM has the advantages that the physical properties are extracted directly from the time evolution of the wave function, without any diagonalization of the Hamiltonian matrix.

3.3 Spatial resolved electronic structure of twisted graphene

When two layers of graphene are stacked on top of each other the electronic structure alters substantially. The low energy electronic band structure of bilayer graphene depends on how the two graphene layers are stacked[7]. The most common stacking is the so-called AB or Bernal stacking. The atoms of one of the hexagonal sublattices of the top layer (A1) are located on top of the atoms of one of the sublattices of the bottom layer (B2). The other atoms (B1 and A2) do not lie directly below or above an atom of the other layer. Highly oriented pyrolytic graphite is often stacked in the Bernal configuration. Commensurably twisted bilayer graphene can result in two different moiré lattice types[18]. The first type has a simple two-dimensional hexagonal superlattice, which is similar to the AB-stacked (Bernal) lattice. The other type has a two-dimensional honeycomb superlattice comprising two equivalent hexagonal superlattices, and is similar to the AA-type stacked lattice. The honeycomb cases can be generated by twisting the two layers relative to one another over special angles θ obtained from the relation[18, 19]

$$\cos(\theta) = \frac{2n^2+2nm-m^2}{2(n^2+nm+m^2)}, \qquad (2)$$

in which the integers n and m have no common divisors, and $n - m$ is not an integer multiple of 3[1]. The superlattice vectors are then given by $A_1 = na_1 + ma_2$, respectively, $A_2 = -ma_1 + (n + m)a_2$ with a supercell size factor $N = n^2 + nm + m^2$ larger than in graphene[20, 21]. The simple hexagonal lattice type can be obtained from the same relations by twisting over the special angles $\theta + \pi$. Figure 3.1 shows the scanning tunneling microscopy images of twisted graphene layers on the highly oriented pyrolytic graphite surface recorded at room temperature. Different twisted angles θ are extracted according to the periodicity λ of the moiré pattern,

$$\lambda = a_0/2\sin(\frac{\theta}{2}), \qquad (3)$$

where a_0= 0.246 nm is the lattice constant of graphene.

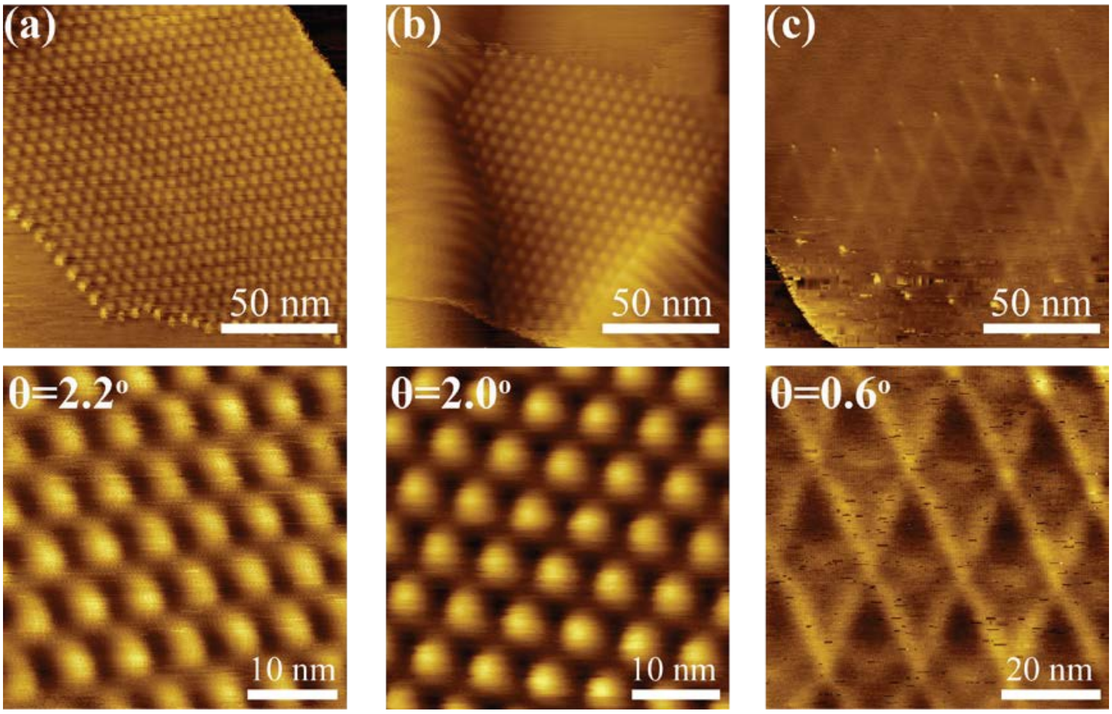

Figure 3.1: Scanning tunneling microscopy images of twisted graphene with different twisted angles, (a) 2.2°; (b) 2.0°; (c) 0.6°.

The electronic structure of this moiré pattern is characterized by a set of two Dirac cones that are located close to each other in reciprocal space. The crossing of these two Dirac cones results into two Van Hove singularities (vHS). As shown in Figure 3.2, as the AA stacking bilayer graphene is twisted by θ, the Brillouin zones of the graphene layers are equally rotated by θ. Thus, the Dirac cones of each layer are now centered in different points of the reciprocal space K_1 and K_2. The cones merge into two saddle points at energies $\pm E_{\mathrm{vHS}}$ from the Dirac point, leading to vHS which generate peaks in the DOS. Here the energy difference ΔE_{vHS} follows[1, 7]:

$$\Delta E_{\text{vHS}} = 2\hbar \upsilon_F \Gamma K \sin\left(\frac{\theta}{2}\right) - 2t_\theta \,, \tag{4}$$

where υ_F is the Fermi velocity for monolayer graphene, ΓK = 1.703 Å^{-1} is the wave vector of the Dirac point in monolayer graphene, and t_θ is the modulus of the amplitude of the main Fourier components of the interlayer potential.

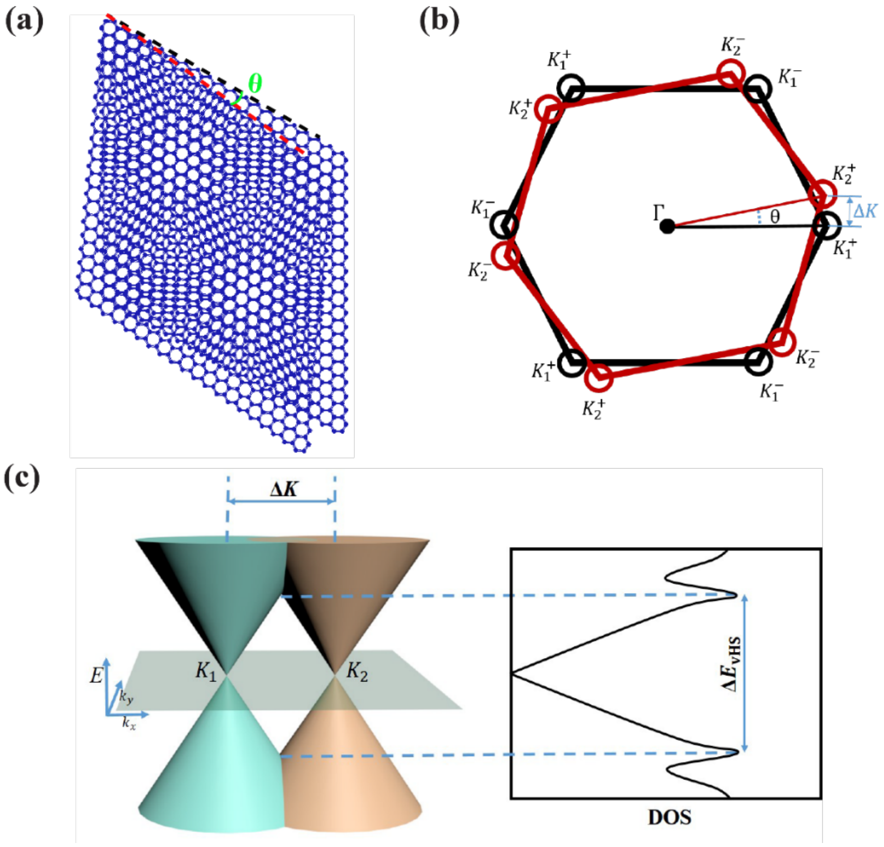

Figure 3.2: Origin of the Van Hove singularities in twisted graphene layer (a) Illustration of a moiré pattern arising from a twisted angle θ. (b) Corresponding rotation in reciprocal space. (c) Emergence of vHS.

In Figure 3.3a, a scanning tunneling microscopy image of a twisted graphene with a twist angle of 2.0° is displayed. The image is recorded at room temperature and the moiré pattern has a periodicity of 7.0 nm. The differential conductivity *dI/dV*, which is proportional to the density of states for small biases, is depicted in Figure 3.3b. The *dI/dV* curves recorded at a 60×60 grid of the surface displayed in the inset of Figure 3.3a. Two well-defined peaks are found at energies of -110 meV and 15 meV with respect to the Fermi level, respectively. These two peaks are Van Hove singularities. At the high regions of the moiré pattern the peaks have a higher intensity as compared to the lower regions of the moiré pattern. The energy separation, relative strength, and asymmetry are in good agreement with Ref. [1]. The *dI/dV* spectra in Figure 3.3b are recorded at room temperature and therefore these peaks are much broader than the peaks that are reported in Ref.[1], which are taken at 4 K.

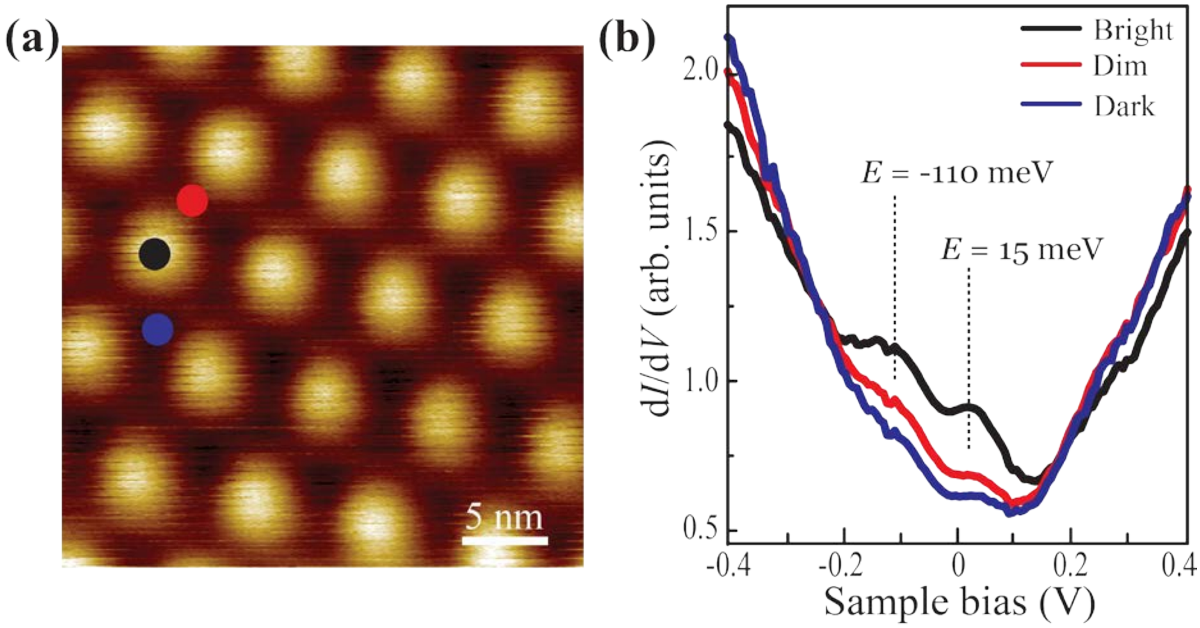

Figure 3.3: (a) Scanning tunneling microscopy image of twisted graphene. (b) Differential conductivity recorded at different locations (bright, dim and dark).

In order to understand the experimental observations shown in Figure 3.3b, we have performed theoretical calculations of the density of states by using the Slater-Koster tight-binding model for rotated bilayer and trilayer graphene, respectively. The numerical results of the integrated density of states are plotted in Figure 3.4.

It is clear that although the two Van Hove singularities are always present when there is a rotated graphene layer, one has to take into account the third layer in order to reproduce the significant electron-hole asymmetry and the finite density of the states in the vicinity of the Fermi level. The electron-hole asymmetry is enhanced if the interlayer hoppings between the top and the third layer are also included. Furthermore, by turning on the direct interactions between the top and the third layer, the whole energy spectrum is shifted to the hole direction, similar to the experimental observations. Here we want to emphasize that for a heterostructure consisting of a rotated graphene layer on top of graphite, it is not sufficient to only consider a rotated bilayer graphene in the theoretical studies. The influence of the third layer, either indirectly via the hoppings to the middle layer, or directly via the interactions to the top layer, is not negligible.

It is therefore necessary to consider at least three layers in the calculations of the electronic structure and physical properties.

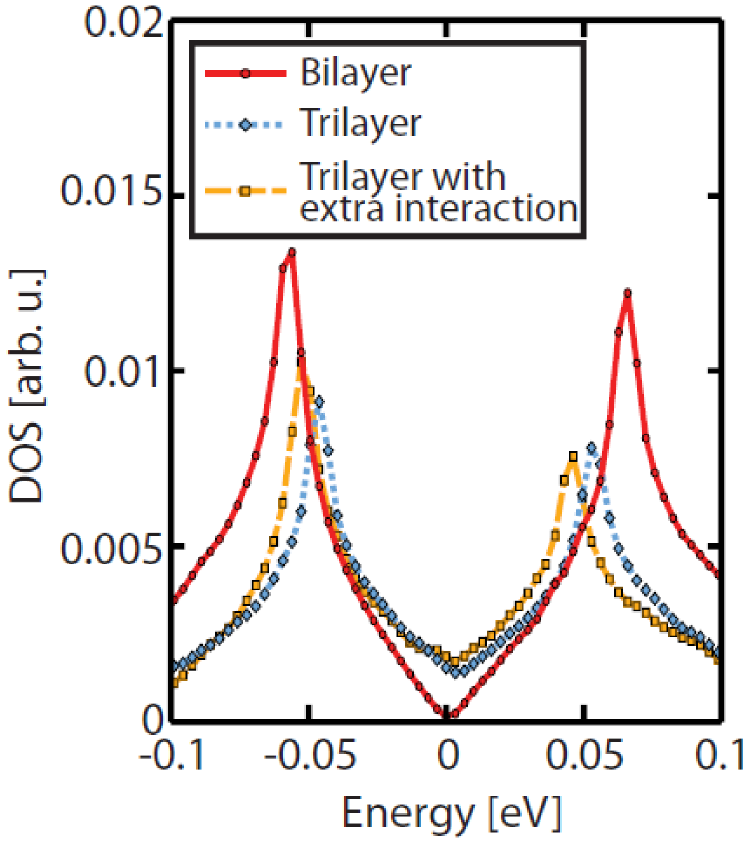

Figure 3.4: (b) Calculated total density of states for rotated bilayer and trilayer graphene (θ = 2.0^o, for trilayer graphene with an extra interaction interlayer hoppings between the top and bottom layers with a maximum value of 0.1 eV are included (for two sites on A-A stacking).

In the two middle panels of Figure 3.5, spatial maps of the differential conductivity are shown at various energies. The moiré pattern is present in the differential conductivity maps that are recorded near the Fermi level, but the structure fades away at larger energies. Also this observation is consistent with Ref. [1], albeit the sample bias range where we observe the moiré pattern in the *dI/dV* signal is substantially larger.

With aim of understanding this strong energy dependence of the differential conductivity maps we have performed tight-binding calculations of a quasi-eigenstate, which is a superposition state of all degenerate eigenstates at a given energy[15]. The real-space distribution of the wave amplitude in a quasi-eigenstate corresponds to the local density of states measured in the scanning tunneling microscopy experiments[16]. In the left and right panels of Figure 3.5 we show contour plots of several quasi-eigenstates for a layer of rotated graphene stacked on top of an AB-stacked bilayer graphene. Our theoretical calculations of this heterostructure consisting of three graphene layers show exactly the same tendency as the experimental data, i.e., the hexagonal structure in the density states is only present near the Fermi level and fades away at higher energies.

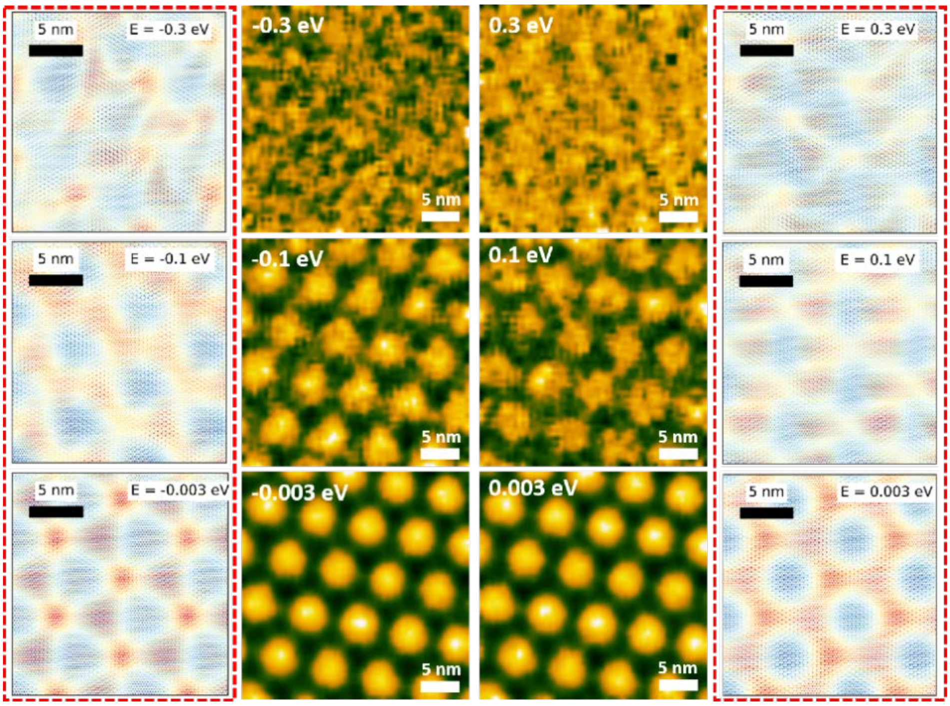

Figure 3.5: Middle panels: Spatial map of the differential conductivity at different bias voltages. The large bright spots in the *dI/dV* maps correspond to the higher parts of the moiré pattern [see Figure 3.3a]. Left and right panels (in red dashed box): The real-space amplitude (logarithmic scale) of the calculated quasieigenstates for trilayer graphene with twisted top layer ($\theta = 2.0^{o}$). The results are obtained by averaging over 24 initial states to mimic the randomness introduced by the initial state. In each figure, blue and red correspond to the maximal and minimal intensity, respectively. For higher absolute energy this amplitude is lower.

The fact that the differential conductivity only exhibits a density modulation near the Van Hove singularities is reminiscent of a charge density wave. One of the hallmarks of a charge density wave is that the electron density and the lattice positions are coupled. Charge density waves may be generated by an exchange-driven instability of a metallic Fermi surface (Fermi nesting), or by a lattice-dynamical instability leading to a static periodic lattice distortion. It is important to point out here that a periodic potential in a Dirac system will not result in the opening of a band gap, but rather in the creation of new Dirac points and Van Hove singularities[22, 23]. The concept of charge density of waves needs therefore to be revisited for Dirac systems. The energy dependent electron density modulation that we measured for twisted graphene can be fully explained by tight-binding calculations. Since electron-phonon coupling is not included in these tight-binding calculations it remains to be seen whether we are dealing here with a charge density wave.

In Figure 3.6a, a high resolution spatial map of the differential conductivity of the strongest Van Hove singularity, which is located at -110 meV, is shown. This spatial map is recorded with a lock-in amplifier (modulation voltage 20 mV and frequency 1.9 kHz). The spatial *dI/dV* map exhibits atomic resolution. Even the periodicity of the top graphene layer with a lattice constant of 0.246 nm is visible. For the sake of clarify we have inverted the color scale in Figure 3.6a, so dark regions refer to a high *dI/dV* signal, whereas bright spots refer to a low *dI/dV* signal. The honeycomb structure consists of two interpenetrating hexagonal sublattices. One hexagonal sublattice displays a substantially higher *dI/dV* signal than the other hexagonal sublattice. The occurrence of these two hexagonal sublattices can be understood if one takes into account a third graphene layer that breaks the symmetry of a twisted bilayer graphene. The dominant stacking arrangement of HOPG is the Bernal (AB) stacking. Consequently, half of

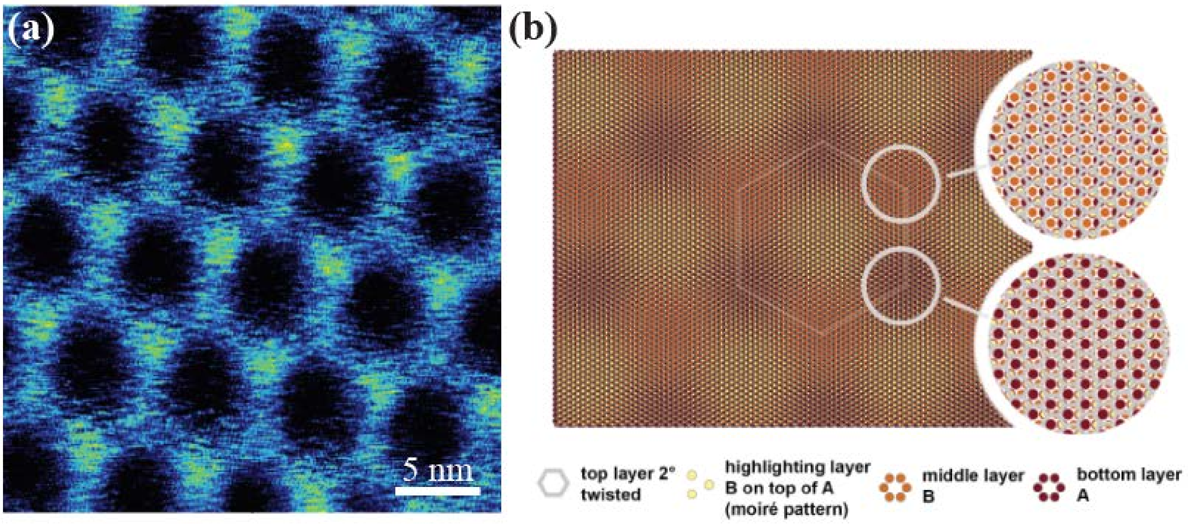

Figure 3.6: (a) Spatial map of the differential conductivity. (b) Structural model of trilayer graphene.

the carbon atoms of the second graphene layer are located on top of a carbon atom of the bottom layer, whereas the other half of the second layer carbon atoms do not have a carbon atom underneath them. In Figure 3.6b the schematic diagram of the trilayer graphene is depicted: the two bottom graphene layers are AB stacked, whereas the top graphene layer is twisted by 2.0^{o} with respect to the second graphene layer. The honeycomb lattice of the moiré pattern in Figure 3.6b is composed of two interpenetrating hexagonal sublattices. The highest *dI/dV* signal is observed if the atoms in the second layer have atoms directly underneath them.

3.4 Conclusions

Spatially resolved scanning tunneling spectroscopy measurements of twisted graphene reveal a hitherto unnoticed variation of the density of states within the unit cell of the moiré pattern. A honeycomb pattern is found that is comprised of two *inequivalent* hexagonal sublattices. The symmetry of the honeycomb lattice of the moiré pattern is broken by a third graphene layer that is stacked in a Bernal configuration with respect to the second graphene layer. Our experimental findings are in excellent agreement with tight-binding calculations.

Bibliography

[1] Li, G.; Luican, A.; Lopes dos Santos, J. M. B.; Castro Neto, A. H.; Reina, A.; Kong, J.; Andrei, E. Y. Observation of Van Hove Singularities in Twisted Graphene Layers. *Nat. Phys.* **2010**, *6* (2), 109–113.

[2] Yin, L.-J.; Qiao, J.-B.; Wang, W.-X.; Chu, Z.-D.; Zhang, K. F.; Dou, R.-F.; Gao, C. L.; Jia, J.-F.; Nie, J.-C.; He, L. Tuning Structures and Electronic Spectra of Graphene Layers with Tilt Grain Boundaries. *Phys. Rev. B* **2014**, *89* (20), 205410.

[3] Yan, W.; Liu, M.; Dou, R.-F.; Meng, L.; Feng, L.; Chu, Z.-D.; Zhang, Y.; Liu, Z.; Nie, J.-C.; He, L. Angle-Dependent van Hove Singularities in a Slightly Twisted Graphene Bilayer. *Phys. Rev. Lett.* **2012**, *109* (12), 126801.

[4] Yan, W.; Meng, L.; Liu, M.; Qiao, J.-B.; Chu, Z.-D.; Dou, R.-F.; Liu, Z.; Nie, J.-C.; Naugle, D. G.; He, L. Angle-Dependent van Hove Singularities and Their Breakdown in Twisted Graphene Bilayers. *Phys. Rev. B* **2014**, *90* (11), 115402.

[5] Yin, L.-J.; Qiao, J.-B.; Zuo, W.-J.; Li, W.-T.; He, L. Experimental Evidence for Non-Abelian Gauge Potentials in Twisted Graphene Bilayers. *Phys. Rev. B* **2015**, *92* (8), 081406.

[6] Wong, D.; Wang, Y.; Jung, J.; Pezzini, S.; DaSilva, A. M.; Tsai, H.-Z.; Jung, H. S.; Khajeh, R.; Kim, Y.; Lee, J.; et al. Local Spectroscopy of Moir\’e-Induced Electronic Structure in Gate-Tunable Twisted Bilayer Graphene. *Phys. Rev. B* **2015**, *92* (15), 155409.

[7] Lopes dos Santos, J. M. B.; Peres, N. M. R.; Castro Neto, A. H. Graphene Bilayer with a Twist: Electronic Structure. *Phys. Rev. Lett.* **2007**, *99* (25), 256802.

[8] Ohta, T.; Bostwick, A.; Seyller, T.; Horn, K.; Rotenberg, E. Controlling the Electronic Structure of Bilayer Graphene. *Science* **2006**, *313* (5789), 951–954.

[9] Castro, E. V.; Novoselov, K. S.; Morozov, S. V.; Peres, N. M. R.; dos Santos, J. M. B. L.; Nilsson, J.; Guinea, F.; Geim, A. K.; Neto, A. H. C. Biased Bilayer Graphene:

Semiconductor with a Gap Tunable by the Electric Field Effect. *Phys. Rev. Lett.* **2007**, *99* (21), 216802.

[10] Li, G.; Luican, A.; Andrei, E. Y. Scanning Tunneling Spectroscopy of Graphene on Graphite. *Phys. Rev. Lett.* **2009**, *102* (17), 176804.

[11] Trambly de Laissardière, G.; Mayou, D.; Magaud, L. Localization of Dirac Electrons in Rotated Graphene Bilayers. *Nano Lett.* **2010**, *10* (3), 804–808.

[12] Luican, A.; Li, G.; Reina, A.; Kong, J.; Nair, R. R.; Novoselov, K. S.; Geim, A. K.; Andrei, E. Y. Single-Layer Behavior and Its Breakdown in Twisted Graphene Layers. *Phys. Rev. Lett.* **2011**, *106* (12), 126802.

[13] Brihuega, I.; Mallet, P.; González-Herrero, H.; Trambly de Laissardière, G.; Ugeda, M. M.; Magaud, L.; Gómez-Rodríguez, J. M.; Ynduráin, F.; Veuillen, J.-Y. Unraveling the Intrinsic and Robust Nature of van Hove Singularities in Twisted Bilayer Graphene by Scanning Tunneling Microscopy and Theoretical Analysis. *Phys. Rev. Lett.* **2012**, *109* (19), 196802.

[14] Sboychakov, A. O.; Rakhmanov, A. L.; Rozhkov, A. V.; Nori, F. Electronic Spectrum of Twisted Bilayer Graphene. *Phys. Rev. B* **2015**, *92* (7), 075402.

[15] Tang, M. S.; Wang, C. Z.; Chan, C. T.; Ho, K. M. Environment-Dependent Tight-Binding Potential Model. *Phys. Rev. B* **1996**, *53* (3), 979–982.

[16] Yuan, S.; De Raedt, H.; Katsnelson, M. I. Modeling Electronic Structure and Transport Properties of Graphene with Resonant Scattering Centers. *Phys. Rev. B* **2010**, *82* (11), 115448.

[17] Yuan, S.; Wehling, T. O.; Lichtenstein, A. I.; Katsnelson, M. I. Enhanced Screening in Chemically Functionalized Graphene. *Phys. Rev. Lett.* **2012**, *109* (15), 156601.

[18] Yıldız, D.; Şen, H. Ş.; Gülseren, O.; Gürlü, O. Apparent Corrugation Variations in Moir\’e Patterns of Dislocated Graphene on Highly Oriented Pyrolytic Graphite and the

Origin of the van Hove Singularities of the Moir\'e System. *ArXiv150200869 Cond-Mat* **2015**.

[19] Wijk, M. M. van; Schuring, A.; Katsnelson, M. I.; Fasolino, A. Relaxation of Moiré Patterns for Slightly Misaligned Identical Lattices: Graphene on Graphite. *2D Mater.* **2015**, *2* (3), 034010.

[20] Albrecht, T. R.; Mizes, H. A.; Nogami, J.; Park, S.; Quate, C. F. Observation of Tilt Boundaries in Graphite by Scanning Tunneling Microscopy and Associated Multiple Tip Effects. *Appl. Phys. Lett.* **1988**, *52* (5), 362–364.

[21] Kuwabara, M.; Clarke, D. R.; Smith, D. A. Anomalous Superperiodicity in Scanning Tunneling Microscope Images of Graphite. *Appl. Phys. Lett.* **1990**, *56* (24), 2396–2398.

[22] Park, C.-H.; Yang, L.; Son, Y.-W.; Cohen, M. L.; Louie, S. G. Anisotropic Behaviours of Massless Dirac Fermions in Graphene under Periodic Potentials. *Nat. Phys.* **2008**, *4* (3), 213–217.

[23] Park, C.-H.; Yang, L.; Son, Y.-W.; Cohen, M. L.; Louie, S. G. New Generation of Massless Dirac Fermions in Graphene under External Periodic Potentials. *Phys. Rev. Lett.* **2008**, *101* (12), 126804.

Intercalation of silicon in transition metal dichalcogenides

4.1 Introduction

Since the isolation of graphene by Novoselov and Geim,[1] two-dimensional (2D) materials have received a lot of attention. The method of delaminating graphite down to a single layer is facilitated by the crystal structure of graphite, which consists of 2D layers that are weakly bonded to each other via van der Waals forces.[2] Besides graphite, other 2D materials such as the transition metal dichalcogenides (TMDs) also consist of these weakly van der Waals bonded layers. The chemical composition of each of these TMDs is MX_2, where M refers to a transition metal, e.g., molybdenum or tungsten, and X stands for a chalcogen such as sulfur or selenium. Each TMD layer consists of three sheets with hexagonal symmetry that are covalently bonded to each other. In each of these triple layers, one layer of transition metal atoms is sandwiched in between two layers of chalcogen atoms. Since the TMDs have a similar layered structure as graphite, it is not surprising that a renewed interest in the TMDs aroused when it was found possible to also exfoliate these materials to a single layer.[3] As such, it was found that the physical properties of TMDs such as the band gap[4] and electron-phonon coupling[5] depend on the number of TMD triple layers.

Pristine and free-standing graphene is gapless, and therefore this material cannot be used as the key material for the field-effect based devices. Many scientists have, however, tried to open a band gap in pristine graphene by breaking the sub-lattice symmetry.[6,7] So far, these attempts have failed or resulted in a strong degradation of the charge carrier mobilities. A more suitable 2D material for realizing a field effect transistor is silicene, the silicon analogue of graphene, which naturally already displays a broken sub-lattice symmetry. The charge carriers in silicene have been predicted to behave similar to the massless Dirac fermions of graphene.[8] Unlike graphite and the TMDs, silicene does not occur in nature and therefore it has to be synthesized. Several research groups have shown that silicene can be grown on Ag(111).[9–12] Silicene synthesized on Ag(111) even displays a linear dispersion relation;[11] however, the exact origin of this linear energy band is still under debate.[13] Unfortunately, silicene has a strong electronic coupling with the Ag(111) substrate and as a result loses its Dirac fermion characteristics.[14] To protect the unique electronic properties of silicene, the electronic coupling with the substrate should be reduced as much as possible. TMDs like WSe_2 and MoS_2, which have no dangling bonds, are atomically flat over large areas, and have a band gap, seem to fit all the requirements to support the growth of silicene as the interaction with the 2D adlayer is only via very weak van der Waals forces.[15] This weak interaction will help to preserve the important electronic properties near the Fermi level. The growth of silicon on MoS_2 has already been studied.[16,17] Another appealing two-dimensional material is germanene.[18–21] Recently, the synthesis of germanene on MoS_2 has been reported.[22] The density of states of germanene on MoS_2 exhibits a well-defined V-shape, which is one of the hallmarks of a two-dimensional Dirac material.[23] In this chapter, we report on the growth of submonolayers of silicon on tungsten diselenide (WSe_2). Upon deposition of silicon, the atomically flat WSe_2 surface converts into a surface with a hill-and-valley structure. Guided by our high-resolution scanning tunneling microscopy (STM) and spectroscopy (STS) measurements, we provide compelling evidence that silicon does not grow on top of WSe_2 but intercalates between the WSe_2 layers.

4.2 Experimental details

The experiments were carried out in a system equipped with a room temperature Omicron STM (STM-1). The base pressure in the system is below 3×10^{-11} mbar. All the STM and STS measurements were conducted at room temperature. The synthetic WSe_2 samples purchased from HQ Graphene were cleaned by mechanical exfoliation in ambient conditions after which they were immediately mounted on a sample holder and inserted into the ultra-high vacuum system. Limited contamination is expected because the samples are non-reactive. Silicon was deposited on the WSe_2 samples via the resistive heating of a small piece of a silicon wafer. In order to calibrate the silicon source, we deposited a fraction of a monolayer of silicon on a Ge(001) substrate at room temperature. Subsequently, the Ge(001) substrate was mildly annealed at a temperature 450–500 K. After that, we determined the coverage of the epitaxial silicon islands.

4.3 Growth of silicon on tungsten diselenide

Before the deposition of silicon, the samples of freshly cleaved WSe_2 are characterized by the constant current topography STM images. In this STM mode, the tip-sample distance is adjusted as to keep a constant tunneling current while the extension of the z-piezo is recorded. The lattice constant of the hexagonal lattice of WSe_2 is 3.28 Å.[24] Even at larger length scales, the mechanically cleaved samples of WSe_2 are atomically flat, as can be seen in the inset of Figure 4.1. Only a few electronic defects can be observed in an area of 80×80 nm^2. The average terrace size of WSe_2 is very large, and step edges are only rarely encountered in STM scans.

After the deposition of about a quarter of a monolayer of silicon on clean WSe_2, the WSe_2 surface displays more roughness in the STM topography scans than the bare surface, as can be seen in Figure 4.2a. A hill-and-valley structure can be observed in the topography scans, similar to the observations by Chiappe et al.[16] and Molle et al.[17] for the silicon on MoS_2 system. Upon the deposition of more silicon, the surface becomes even rougher and after a few monolayers eventually 3D clusters are observed on the surface. It is not obvious at all that the growth does resemble typical island growth, as was suggested by Chiappe et al.[16] for the Si/MoS_2 system. A firm argument against island growth is the fact that the lattice constant of the hill-and valley is exactly the same as the lattice constant of the bare WSe_2 or MoS_2 substrates. This is not compatible with the silicon island growth on top of WSe_2 since the lattice constants of silicon or low-buckled silicene are substantially larger.[25] Chiappe et al.[16] interpreted the observed small lattice constant as the growth of strained high-buckled silicene. They argued that high-buckled silicene grows epitaxially on MoS_2, i.e., the lattice constant of silicene adapts itself to the lattice constant of the MoS_2 substrate. However, it should be pointed out that freestanding high buckled silicene is unstable because it has imaginary phonon modes in a large portion of the Brillouin zone.[26,27] In addition, the interaction between the silicon adlayer and the substrate

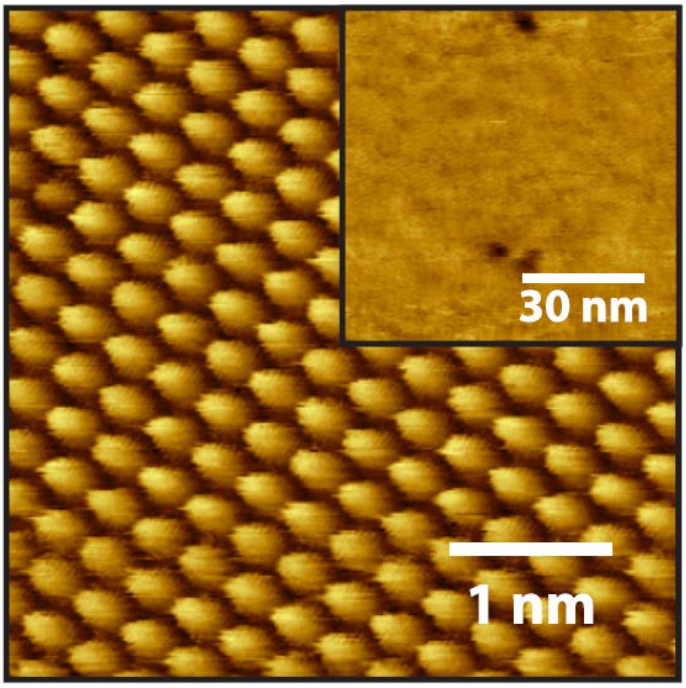

Figure 4.1: The clean atomically resolved surface of WSe_2 (V= -0.6V, I= 1.1 nA). Inset: Large area scan of WSe2 showing a few electronic defects.

is governed by weak van der Waals forces and therefore the formation of a strained epitaxial silicon layer is highly unlikely. Actually, van der Waals heteroepitaxy has been demonstrated even for materials with a large lattice mismatch.[28] Another strong argument against island growth is that the transition from a hill to a valley is very gradual, as can be seen in the line profile in Figure 4.2c. In the case of island growth on top of a substrate, one expects to encounter well-defined island edges, which show up as abrupt height variations in the constant current STM scans. The gradual transition from a hill to a valley does, however, support the idea of a buckled WSe_2 top layer.

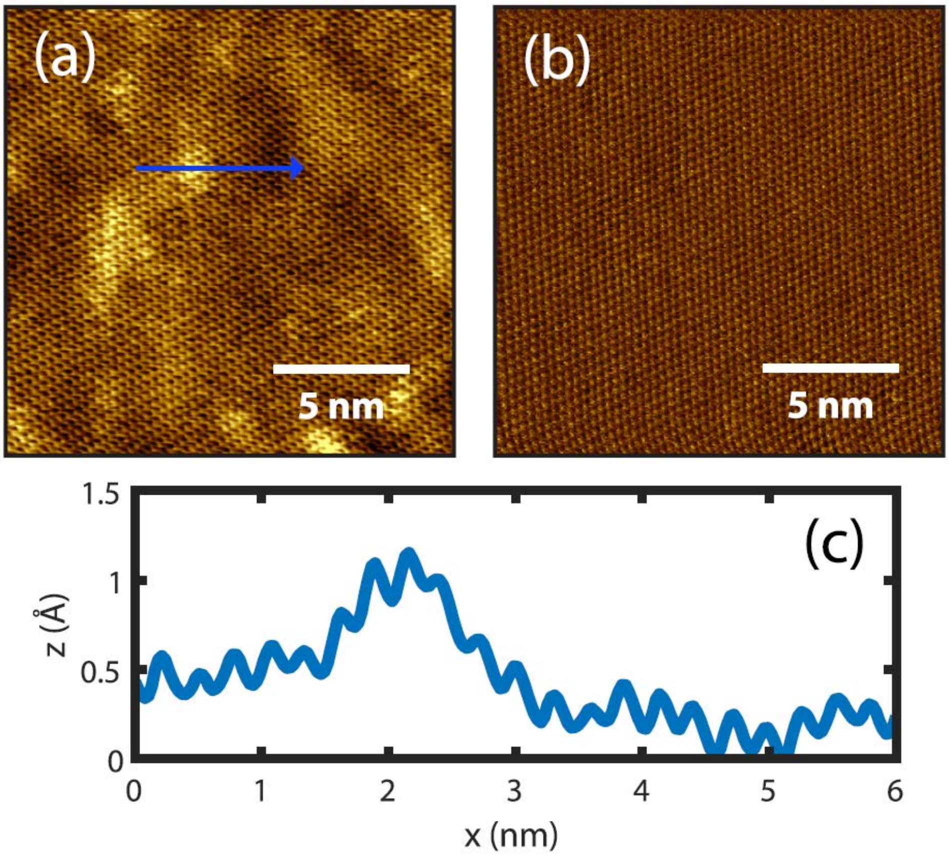

Figure 4.2: Constant current topography (a) and *dI/dz* (b) maps of WSe_2 after deposition of 0.25 ML of silicon (V= -0.8 V, I= 1.5 nA). The *dI/dz* map is proportional to the local apparent barrier height. The maps are recorded simultaneously. The line profile indicated in (a) is displayed in panel (c).

At this point, it is still not clear what the hills and valleys in the topography scans exactly represent. This is because a constant current topography scan in the STM contains both topographic and electronic information. In order to determine the exact nature of the hill-and-valley structure, one needs to separate the topographic and electronic signals and obtain chemical sensitivity on the surface. In STM, this can be accomplished by operating the STM in the *dI/dz* spectroscopy mode. The *dI/dz* signal can be recorded simultaneously with the constant current topography. In the constant current mode, the z-piezo voltage is measured (the z-piezo voltage can be converted into a height z_0, which should be discriminated from, z, the tip-sample distance), whereas in the *dI/dz* mode only the derivative of the current to z is measured. The fact that the *dI/dz* signal is not dependent on the local surface height variations can easily be understood within the framework of the Tersoff and Hamann approximation.[29] The tunnel current I is given by

$$I = C \int_0^{eV} \rho_t(E - eV)\rho_s(E)T(V, E, z)dE \,, \qquad (1)$$

where C is a proportionality constant, e the elementary charge, V the applied voltage between tip and sample and ρ_t and ρ_s the density of states of the tip and sample, respectively. $T(V, E, z)$ is the tunneling probability and E and z are the electron energy and the tip-sample distance, respectively. The tunneling probability depends on the tip-sample distance z, but not z_0

$$T(V, E, z) = \exp\left(-2\frac{\sqrt{2m}}{\hbar}\, z\sqrt{\varphi_A + \frac{eV}{2} - E}\right), \qquad (2)$$

with m the electron mass and φ_A the local apparent barrier height[30] that is equal to $(\varphi_s + \varphi_t)/2$, where φ_s and φ_t are the work functions of the sample and the tip, respectively. The derivative of this tunneling probability is given by

$$\frac{dT}{dz} = T(V, E, z)\left(-2\frac{\sqrt{2m}}{\hbar}\, z\sqrt{\varphi_A + \frac{eV}{2} - E}\right) = A(V, E)T(V, E, z). \quad (3)$$

We emphasize that $A(V, E)$ does not depend on z. When we insert Equation (2) of $T(V, E, z)$ in the expression of the current I in Equation (1), *dI/dz* is given by

$$\frac{dI}{dz} = C \int_0^{eV} \rho_t\,(E - eV)\rho_s(E)\,\frac{T(V,E,z)}{dz}\,dE = A(V, E)I. \qquad (4)$$

Here, *dI/dz* does not depend on z_0, i.e., the extension of the z-piezo, or z, the tip-sample distance. For small sample biases, i.e., $eV/2 \ll \varphi_A$, one finds

$$\frac{1}{I}\frac{dI}{dz} = \frac{dln(I)}{dz} \approx \frac{2\sqrt{2m}}{\hbar} I\sqrt{\varphi_A}\,. \qquad (5)$$

The apparent barrier height is related to the local sample work function as stated earlier and is sensitive to the chemical composition of the surface. The measured apparent barrier height has experimentally been found to be independent of the tip-sample distance for reasonable tunnel gaps up until the point of contact.[31] During constant current scanning, the height of the tip is constantly adjusted as to keep a constant tunneling current. To record these *dI/dz* maps, a small sinusoidal signal (with a frequency that exceeds the bandwidth of the feedback loop) is applied to the *z*-piezo during scanning at constant current. The resulting oscillations in the current can be accurately detected by a lock-in technique.

Simultaneously with the topography in Figure 4.2a, the *dI/dz* map as shown in Figure 4.2b was obtained. As can be seen, the *dI/dz* map does not show any contrast besides the atomic corrugation. This atomic corrugation is a result of lateral variations of the decay length of the surface wave functions, as discussed in more detail by Wiesendanger.[30] With the topographic information removed, it is even more clear that there is one continuous lattice. Also, since the topographic information is removed from this scan, we conclude that the electronic properties of the hills and valleys are identical. This would not be the case if the hills were silicon islands because this would result in a contrast variation of the measured apparent barrier height. Therefore, we have to conclude that there is actually no silicon at all on the surface of WSe_2. The outer-most layer of the hill and valley structure is pure WSe_2, and therefore silicon must have been intercalated in between the top layers of WSe_2. These results are supported by *I(V)* spectra recorded on the bare WSe_2 surface before and after the deposition of silicon in Figure 4.3. In order to compare the *I(V)* traces of the bare WSe_2 surface and hills and valleys that are found after deposition, we have taken all *I(V)* traces with the same set points (V= -0.8 V and I= 1.5 nA). As can be seen in Figure 4.3, all three *I(V)* curves share the same semiconductor

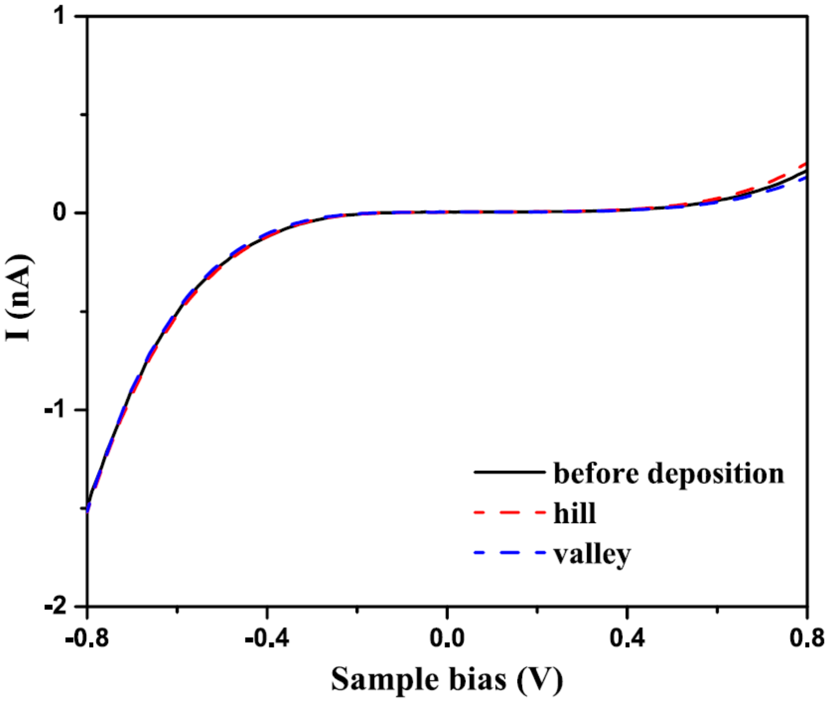

Figure 4.3: *I(V)* curves recorded on WSe_2 (V= -0.8V and I= 1.5 nA) before deposition (black curve), after the deposition of 0.25 monolayers of Si on a hill (red curve) and a valley (blue curve).

characteristics with similar bandgap. Finally, it should be noted that intercalation is ubiquitous in TMDs because intercalated atoms can exchange charge more easily than atoms located on top of the TMD.[32] Intercalation has been found to occur through defects or steps in the surface.[33] The diffusion barrier on van der Waals materials is very low, and therefore the adatoms can easily reach step edges or defects, even though the defect density is rather low.[34] Intercalation in TMDs is the rule rather than the exception for small atoms such as sodium and lithium,[33, 35] but even large atoms, such as cesium and gold, can intercalate.[36–38]

4.4 Conclusions

In summary, the deposition of silicon on WSe_2 has been studied with scanning tunneling microscopy and spectroscopy. Upon the deposition of silicon, a hill-and-valley structure develops that has a lattice constant that has the exact same value as the TMD substrate. Spatial maps of the *dI/dz* provide compelling evidence that silicon does not grow on top of WSe_2 but rather intercalates between the top layers of WSe_2.

Bibliography

[1] Novoselov, K. S.; Geim, A. K.; Morozov, S. V.; Jiang, D.; Zhang, Y.; Dubonos, S. V.; Grigorieva, I. V.; Firsov, A. A. Electric Field Effect in Atomically Thin Carbon Films. *Science* **2004**, *306* (5696), 666–669.

[2] Rydberg, H.; Dion, M.; Jacobson, N.; Schröder, E.; Hyldgaard, P.; Simak, S. I.; Langreth, D. C.; Lundqvist, B. I. Van Der Waals Density Functional for Layered Structures. *Phys. Rev. Lett.* **2003**, *91* (12), 126402.

[3] Xu, M.; Liang, T.; Shi, M.; Chen, H. Graphene-Like Two-Dimensional Materials. *Chem. Rev.* **2013**, *113* (5), 3766–3798.

[4] Mak, K. F.; Lee, C.; Hone, J.; Shan, J.; Heinz, T. F. Atomically Thin MoS_2: A New Direct-Gap Semiconductor. *Phys. Rev. Lett.* **2010**, *105* (13), 136805.

[5] Li, H.; Zhang, Q.; Yap, C. C. R.; Tay, B. K.; Edwin, T. H. T.; Olivier, A.; Baillargeat, D. From Bulk to Monolayer MoS_2: Evolution of Raman Scattering. *Adv. Funct. Mater.* **2012**, *22* (7), 1385–1390.

[6] Balog, R.; Jørgensen, B.; Nilsson, L.; Andersen, M.; Rienks, E.; Bianchi, M.; Fanetti, M.; Lægsgaard, E.; Baraldi, A.; Lizzit, S.; et al. Bandgap Opening in Graphene Induced by Patterned Hydrogen Adsorption. *Nat. Mater.* **2010**, *9* (4), 315–319.

[7] Park, J.-S.; Choi, H. J. Band-Gap Opening in Graphene: A Reverse-Engineering Approach. *Phys. Rev. B* **2015**, *92* (4), 045402.

[8] Guzmán-Verri, G. G.; Lew Yan Voon, L. C. Electronic Structure of Silicon-Based Nanostructures. *Phys. Rev. B* **2007**, *76* (7), 075131.

[9] Lalmi, B.; Oughaddou, H.; Enriquez, H.; Kara, A.; Vizzini, S.; Ealet, B.; Aufray, B. Epitaxial Growth of a Silicene Sheet. *Appl. Phys. Lett.* **2010**, *97* (22), 223109.

[10] Jamgotchian, H.; Colignon, Y.; Hamzaoui, N.; Ealet, B.; Hoarau, J. Y.; Aufray, B.; Bibérian, J. P. Growth of Silicene Layers on Ag(111): Unexpected Effect of the Substrate Temperature. *J. Phys. Condens. Matter* **2012**, *24* (17), 172001.

[11] Vogt, P.; De Padova, P.; Quaresima, C.; Avila, J.; Frantzeskakis, E.; Asensio, M. C.; Resta, A.; Ealet, B.; Le Lay, G. Silicene: Compelling Experimental Evidence for Graphenelike Two-Dimensional Silicon. *Phys. Rev. Lett.* **2012**, *108* (15), 155501.

[12] Enriquez, H.; Vizzini, S.; Kara, A.; Lalmi, B.; Oughaddou, H. Silicene Structures on Silver Surfaces. *J. Phys. Condens. Matter* **2012**, *24* (31), 314211.

[13] Chen, M. X.; Weinert, M. Revealing the Substrate Origin of the Linear Dispersion of Silicene/Ag(111). *Nano Lett.* **2014**, *14* (9), 5189–5193.

[14] Lin, C.-L.; Arafune, R.; Kawahara, K.; Kanno, M.; Tsukahara, N.; Minamitani, E.; Kim, Y.; Kawai, M.; Takagi, N. Substrate-Induced Symmetry Breaking in Silicene. *Phys. Rev. Lett.* **2013**, *110* (7), 076801.

[15] Gao, N.; Li, J. C.; Jiang, Q. Tunable Band Gaps in Silicene–MoS_2 Heterobilayers. *Phys. Chem. Chem. Phys.* **2014**, *16* (23), 11673–11678.

[16] Chiappe, D.; Scalise, E.; Cinquanta, E.; Grazianetti, C.; Broek, B. van den; Fanciulli, M.; Houssa, M.; Molle, A. Two-Dimensional Si Nanosheets with Local Hexagonal Structure on a MoS_2 Surface. *Adv. Mater.* **2014**, *26* (13), 2096–2101.

[17] Molle, A.; Lamperti, A.; Rotta, D.; Fanciulli, M.; Cinquanta, E.; Grazianetti, C. Electron Confinement at the Si/MoS_2 Heterosheet Interface. *Adv. Mater. Interfaces* **2016**, *3* (10), 1500619.

[18] Li, L.; Lu, S.; Pan, J.; Qin, Z.; Wang, Y.; Wang, Y.; Cao, G.; Du, S.; Gao, H.-J. Buckled Germanene Formation on Pt(111). *Adv. Mater.* **2014**, *26* (28), 4820–4824.

[19] Dávila, M. E.; Xian, L.; Cahangirov, S.; Rubio, A.; Lay, G. L. Germanene: A Novel Two-Dimensional Germanium Allotrope Akin to Graphene and Silicene. *New J. Phys.* **2014**, *16* (9), 095002.

[20] Bampoulis, P.; Zhang, L.; Safaei, A.; Gastel, R. van; Poelsema, B.; Zandvliet, H. J. W. Germanene Termination of Ge_2Pt Crystals on Ge(110). *J. Phys. Condens. Matter* **2014**, *26* (44), 442001.

[21] Acun, A.; Zhang, L.; Bampoulis, P.; Farmanbar, M.; van Houselt, A.; Rudenko, A. N.; Lingenfelder, M.; Brocks, G.; Poelsema, B.; Katsnelson, M. I.; et al. Germanene: The Germanium Analogue of Graphene. *J. Phys. Condens. Matter* **2015**, *27* (44), 443002.

[22] Zhang, L.; Bampoulis, P.; Rudenko, A. N.; Yao, Q.; van Houselt, A.; Poelsema, B.; Katsnelson, M. I.; Zandvliet, H. J. W. Structural and Electronic Properties of Germanene on MoS_2. *Phys. Rev. Lett.* **2016**, *116* (25), 256804.

[23] Zhang, L.; Bampoulis, P.; van Houselt, A.; Zandvliet, H. J. W. Two-Dimensional Dirac Signature of Germanene. *Appl. Phys. Lett.* **2015**, *107* (11), 111605.

[24] Schutte, W. J.; De Boer, J. L.; Jellinek, F. Crystal Structures of Tungsten Disulfide and Diselenide. *J. Solid State Chem.* **1987**, *70* (2), 207–209.

[25] Lebègue, S.; Eriksson, O. Electronic Structure of Two-Dimensional Crystals from Ab Initio Theory. *Phys. Rev. B* **2009**, *79* (11), 115409.

[26] Cahangirov, S.; Topsakal, M.; Aktürk, E.; Şahin, H.; Ciraci, S. Two- and One-Dimensional Honeycomb Structures of Silicon and Germanium. *Phys. Rev. Lett.* **2009**, *102* (23), 236804.

[27] Roome, N. J.; Carey, J. D. Beyond Graphene: Stable Elemental Monolayers of Silicene and Germanene. *ACS Appl. Mater. Interfaces* **2014**, *6* (10), 7743–7750.

[28] Koma, A.; Sunouchi, K.; Miyajima, T. Fabrication and Characterization of Heterostructures with Subnanometer Thickness. *Microelectron. Eng.* **1984**, *2* (1), 129–136.

[29] Tersoff, J.; Hamann, D. R. Theory of the Scanning Tunneling Microscope. *Phys. Rev. B* **1985**, *31* (2), 805–813.

[30] Wiesendanger, R.; Roland, W. *Scanning Probe Microscopy and Spectroscopy: Methods and Applications*; Cambridge University Press, 1994.

[31] Olesen, L.; Brandbyge, M.; Sørensen, M. R.; Jacobsen, K. W.; Lægsgaard, E.; Stensgaard, I.; Besenbacher, F. Apparent Barrier Height in Scanning Tunneling Microscopy Revisited. *Phys. Rev. Lett.* **1996**, *76* (9), 1485–1488.

[32] Whittingham, M. S.; Chianelli, R. R. Layered Compounds and Intercalation Chemistry: An Example of Chemistry and Diffusion in Solids. *J. Chem. Educ.* **1980**, *57* (8), 569.

[33] Xiong, F.; Wang, H.; Liu, X.; Sun, J.; Brongersma, M.; Pop, E.; Cui, Y. Li Intercalation in MoS_2: In Situ Observation of Its Dynamics and Tuning Optical and Electrical Properties. *Nano Lett.* **2015**, *15* (10), 6777–6784.

[34] Petrović, M.; Šrut Rakić, I.; Runte, S.; Busse, C.; Sadowski, J. T.; Lazić, P.; Pletikosić, I.; Pan, Z.-H.; Milun, M.; Pervan, P.; et al. The Mechanism of Caesium Intercalation of Graphene. *Nat. Commun.* **2013**, *4*, 2772.

[35] Brauer, H. E.; Starnberg, H. I.; Holleboom, L. J.; Strocov, V. N.; Hughes, H. P. Electronic Structure of Pure and Alkali-Metal-Intercalated VSe_2. *Phys. Rev. B* **1998**, *58* (15), 10031–10045.

[36] Pettenkofer, C.; Jaegermann, W.; Schellenberger, A.; Holub-Krappe, E.; Papageorgopoulos, C. A.; Kamaratos, M.; Papageorgopoulos, A. Cs Deposition on Layered 2*H* $TaSe_2$ (0 0 0 1) Surfaces: Adsorption or Intercalation? *Solid State Commun.* **1992**, *84* (9), 921–926.

[37] Starnberg, H. I.; Brauer, H. E.; Holleboom, L. J.; Hughes, H. P. 3D-to-2D Transition by Cs Intercalation of VSe_2. *Phys. Rev. Lett.* **1993**, *70* (20), 3111–3114.

[38] Iyikanat, F.; Sahin, H.; Senger, R. T.; Peeters, F. M. Ag and Au Atoms Intercalated in Bilayer Heterostructures of Transition Metal Dichalcogenides and Graphene. *APL Mater.* **2014**, *2* (9), 092801.

Effect of substrate and hydrogenation on germanene

5.1 Introduction

The rise of graphene[1,2] has triggered many scientists to synthesize and study other two-dimensional elemental materials. Silicene, germanene, and stanene, i.e., the silicon, germanium, and tin analogues of graphene, are among these two-dimensional materials that have received quite some attention owing to their similarity with graphene.[3–7] Theoretical calculations have revealed that silicene, germanene, and stanene exhibit linear dispersing energy bands in the vicinity of K and K' points of the Brillouin zone.[8–10] These materials are, just as graphene, semimetals that host massless Dirac fermions. In contrast to graphene, these elemental two-dimensional materials do not occur in nature, and therefore, they have to be synthesized. Another disadvantage of silicene, germanene, and stanene is that they oxidize, i.e., they are not stable at ambient conditions. Despite these disadvantages, there are also several advantages: (1) the honeycomb lattices of silicene, germanene, and stanene are not planar, as in graphene, but buckled, paving the way for the opening of a bandgap by, for instance, applying an external electric field and (2) the spin-orbit coupling in these materials is much larger than that in graphene, making these two-dimensional materials appealing candidates for spintronic based applications.

5.1.1 Charge inhomogeneities in 2D material

An ideal graphene sheet, i.e., a sheet that is undoped, perfectly flat, and completely free from defects and charged impurities, has its charge neutrality point, also referred to as the Dirac point, located at the Fermi level. The density of states of this ideal graphene sheet vanishes at the Dirac point. Recent experiments have revealed that graphene placed on a substrate often exhibits a spatially varying Dirac point, resulting in electron-hole puddles. The exact origin of these charge puddles is still under debate. Possible candidates for the occurrence of these charge puddles are (1) charged impurities in the substrate on which the graphene is placed,[11,12] (2) charged species which are intercalated between the graphene sheet and the substrate,[13] and (3) the local curvature of the graphene sheet.[14–16] The first experimental evidence for the occurrence of charge puddles in two-dimensional materials dates back to 2008. Martin et al.[11] used a scanning single-electron transistor to spatially map out the charge inhomogeneities in graphene on SiO_2. One year later, Zhang et al.[12] used a scanning tunneling microscope to map out the charge density inhomogeneities in graphene on SiO_2 by a technique, referred to as Dirac-point mapping, with a charge density spatial resolution that is substantially higher than what can be achieved by the scanning single-electron transistor. These authors arrived at the conclusion that the electron-hole puddles originate from charge donating defects and/or impurities in the SiO_2 substrate. As demonstrated by Martin et al., .[13] also atoms or molecules intercalated between graphene and its support can result in the formation of charge puddles. Gibertini et al.[15, 16] used density functional theory calculations to show that structural corrugations are in principle sufficient to explain the formation of charge puddles in graphene. They also pointed out that the locations of these electron-hole puddles, which have a typical dimension of a few nanometers, do not exhibit a clear correlation with the topography of the graphene sheet. It is worth mentioning that electron-hole puddles are also found in bilayer graphene.[17] So far, charge puddles have only been found in graphene and not in any other elemental two-dimensional material.

In this chapter, we have investigated the electronic disorder of germanene sheets grown on bulk MoS_2 by using scanning tunneling microscopy. Inspired by the observation of charge puddles in graphene sheets, we have scrutinized if such charge inhomogeneities are also present in germanene. In order to map out the charge density of the germanene sheet, we have used the aforementioned Dirac point mapping technique.

5.1.2 From germanene to germanane

Graphene exhibits many interesting and appealing properties, but unfortunately the material cannot be used for field-effect based electronic devices because it is gapless. In principle, a bandgap can be opened in graphene; however, this usually goes at the expense of the high charge carrier mobilities in graphene. Silicene and germanene are, provided that the rather small spin-orbit gap is ignored, also semimetals. Hydrogenated silicene and germanene, usually referred to as silicane and germanane, respectively, exhibit a sizeable bandgap and still have appreciable charge carrier mobilities.[18–20] In 2013, the first successful synthesis of germanane was reported by Bianco et al.[18] These authors synthesized germanane via the topochemical deintercalation of $CaGe_2$. Germanane sheets can be obtained by exfoliation since germanane belongs to the family of layered van der Waals materials. At ambient conditions, germanane turns out to be very stable and the material only oxidizes in a time span of several months. This stability is an important prerequisite for the usage of germanane in any technological application. The strong potential of germanane for technological applications is fueled by theoretical calculations, which predict a direct bandgap of 1.5 eV and an electron mobility that is about five times larger than that of bulk germanium.[19, 20] The existence of a bandgap in germanane was confirmed experimentally by Bianco et al.[18] Inspired by the results of Bianco et al., Madhushankar et al.[21] realized a germanane based field-effect transistor. These authors showed that their germanane field effect transistor, which involved a 60 nm thick stack of germanane layers, exhibited ambipolar transport, but the charge carrier mobilities were much lower (~70 cm^2/V s at room temperature and ~150 cm^2/V s at 77 K) than the theoretical predicted value (20 000 cm^2/V s).

Here, we aim to realize a single germanane layer by hydrogenating germanene synthesized in an ultra-high vacuum environment. The germanene sheets are grown on a substrate, and therefore, only one side of the germanene sheet will be exposed to atomic hydrogen. Since only the Ge atoms of the upward buckled hexagonal sub-lattice will be hydrogenated, the maximum coverage of one monolayer refers to this situation. In this chapter, our scanning tunneling spectroscopy measurements reveal that full hydrogenation results in the opening of a bandgap of about 0.5 eV. Further exposure to atomic hydrogen leads to roughening of the germanane layer, which we ascribe to intercalation of the atomic hydrogen.

5.2 Experimental details

5.2.1 Growth of germanene on MoS_2

The scanning tunneling microscopy (STM) and spectroscopy (STS) experiments have been performed at room temperature with an ultra-high vacuum STM (Omicron STM-1). The base pressure of the ultra-high vacuum system is 3×10^{-11} mbar. MoS_2 samples were freshly cleaved from synthesized 2H-MoS_2 (purchased from 2D Semiconductors) before inserting into the vacuum system. The MoS_2 samples are mounted on a Mo sample holder. Germanium was deposited onto the MoS_2 substrate, which was held at room temperature, by resistively heating a small piece of a Ge(001) wafer at a temperature of ~1150 K. Prior to the deposition process, the Ge(001) wafer was cleaned by outgassing at a temperature of 700 K for about 24 h followed by several cycles of argon ion bombardment at 800 eV and annealing at 1100 K.[22] The Ge source was located at a distance of ~10 mm from the MoS_2 substrate. After the deposition of germanium, the MoS_2 sample was inserted into the STM.

5.2.2 Hydrogenation of germanene terminated on Ge_2Pt nanocrystal

The experiments are performed in an ultra-high vacuum system that is equipped with a room temperature scanning tunneling microscope (Omicron STM1). The base pressure of the ultra-high vacuum system is 3×10^{-11} mbar. The Ge(110) substrates are nearly intrinsic and nominally flat and have dimensions of 10×4×0.5 mm. The substrates are mounted on a sample holder that only contains molybdenum, tantalum, and aluminum oxide components. After introducing the Ge(110) samples, via a load lock system, into the ultra-high vacuum system, they are carefully degassed at a temperature of 800 K for at least 24 h. Subsequently, the samples are cleaned by several cycles of argon ion bombardment at 500 eV and annealing at 1100 K.[22] Pt is deposited on the Ge(110) substrate by resistively heating a W wire wrapped with high purity Pt(99.995%). After Pt-deposition, the sample is flash annealed at 1100 (±25) K and subsequently cooled down to room temperature before inserting it into the scanning tunneling microscope for imaging. The aforementioned procedure results in a Ge(110) surface that contains Ge_2Pt clusters with typical dimensions of a few hundreds of nanometers.[23] There are two types of Ge_2Pt clusters: pyramids and flat-topped clusters. The flat-topped clusters exhibit a buckled honeycomb lattice with a lattice constant of 4.2 Å.[23] Scanning tunneling spectroscopy measurements show that the germanene sheet possesses a V-shaped density of states, which is one of the hallmarks of a two-dimensional Dirac material.[24] The steps of the germanene sheets on the Ge_2Pt clusters are quantized in units of 5.6 ± 0.1 Å, i.e., twice the germanene interlayer spacing.[23] The latter suggest that we are dealing with germanene bilayers or multiples thereof, rather than a single germanene layer. This would also explain why the top germanene layer is electronically decoupled from the Ge_2Pt cluster.

The hydrogen adsorption experiments were performed by exposing the sample at room temperature to high-purity molecular hydrogen at a pressure in the range of 1×10^{-7}–3×10^{-5} mbar. The molecular hydrogen was decomposed into atomic hydrogen using a hot tungsten filament, which was heated to a temperature of about 2000 K. The sample was located in the field of view of the hot tungsten filament at a distance of a few centimeters, which is substantially smaller than the mean free path of the atomic hydrogen.

5.3 Charge puddles in germanene

In Figure 5.1a and 5.1b, a large-scale scanning tunneling microscopy image and a scanning tunneling spectroscopy spectrum of the pristine MoS_2 surface are shown. By examining several large-scale scanning tunneling microscopy images, similar to the one shown in Figure. 5.1a, we have found a defect density of about 3×10^{-3} nm^{-2}. This defect density, which includes the dark and the dimmer defects shown in Figure 5.1a, compares well with a previous study of the defects of MoS_2 using conductive atom force microscopy by Bampoulis et al.[25] The dark features in Figure 5.1a are defects in the first MoS_2 trilayer, whereas the dimmer features are defects located in the second MoS_2 trilayer.[25] As shown by Bampoulis et al.,[25] both the dark and dim defects are electronic in nature since they only show up in conductive atomic force microscopy images and not in topographic atomic force microscopy images. The differential conductivity spectrum displayed in Figure 5.1b demonstrates that the MoS_2 substrate has a sizeable bandgap. The defects in MoS_2 have been extensively studied (see, e.g., Ref. 26 and references therein). MoS_2 exhibits n-type and p-type defects, which are explained by sulfur-deficient and sulfur-rich regions, respectively.[26]

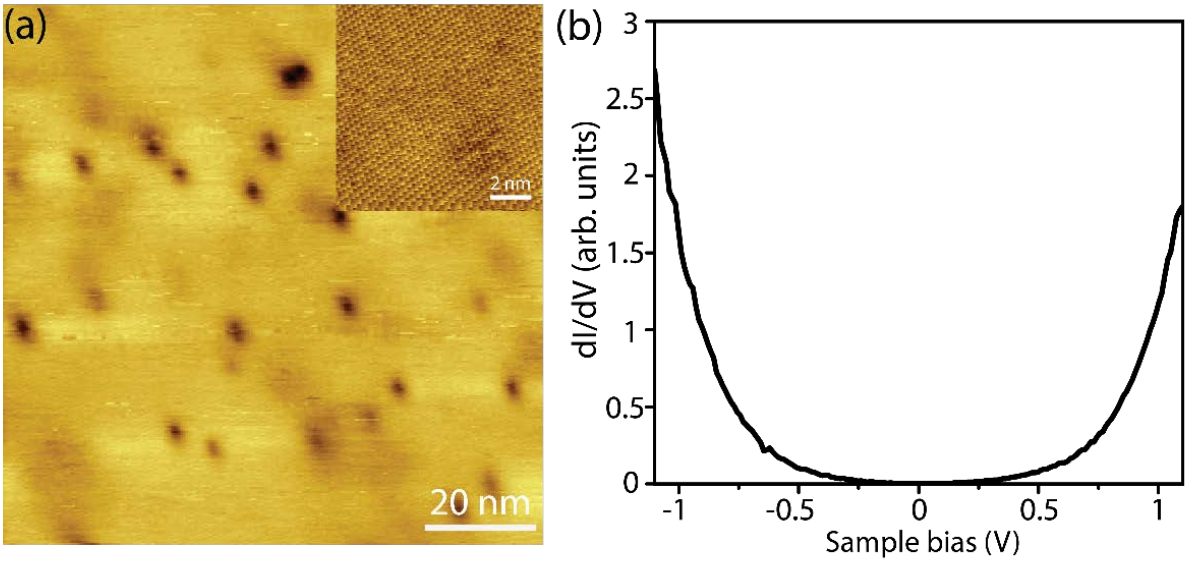

Figure 5.1: (a) Scanning tunneling microscopy image of the pristine MoS_2 surface. Inset: small scale scanning tunneling microscopy image. The sample bias is -0.3 V, and the tunnel current is 500 pA. (b) *dI/dV* spectrum of the pristine MoS_2 surface. The set point values are -1.1 V and 500 pA.

In Figure 5.2a, a scanning tunneling microscopy image of a germanene layer grown on MoS_2 is shown. As we have already shown in a recent study,[5] Ge atoms deposited on the MoS_2 substrate nucleate at pre-existing defects of the MoS_2 surface. The germanene islands have a height of 3.2 Å and exhibit a hexagonal symmetry with a lattice constant of 3.8–3.9 Å, which is about 20% larger than the lattice constant of pristine MoS_2. This relatively large interlayer spacing of 3.2 Å between the germanene sheet and the MoS_2 substrate hints to a relatively weak interaction between the layers as one expects for materials that are held together by Van der Waals interactions. The deposition of more Ge eventually leads to a complete and very flat germanene layer [see Figure 5.2a].[5] Owing to the large buckling of germanene on MoS_2, only one of the two triangular sub-lattices is visible in the scanning tunneling microscopy images [see the inset of Figure 5.2a]. The electronic properties of the germanene layer have been studied by recording grid *I(V)* curves with the feedback loop disabled. The typical grid size is 60×60 for a 100 nm by 100 nm scan. The differential conductivity (*dI/dV*), which is proportional to the density of states, is obtained by numerically differentiating the *I(V)* curves. The averaged *dI/dV* curve is shown in Figure 5.2b. The differential conductivity displays a V-shape, which is one of the signatures of a two-dimensional Dirac material. The density of states does not completely vanish as the Dirac point. The *dI/dV* curve is asymmetric, a feature that we have observed before.[5] The asymmetry of the dI/dV curve could be caused by the electronic structure of the STM tip. In addition, it should be noted that the rounded shape near the Dirac point cannot be fully explained by thermal broadening. A much improved fit is, however,

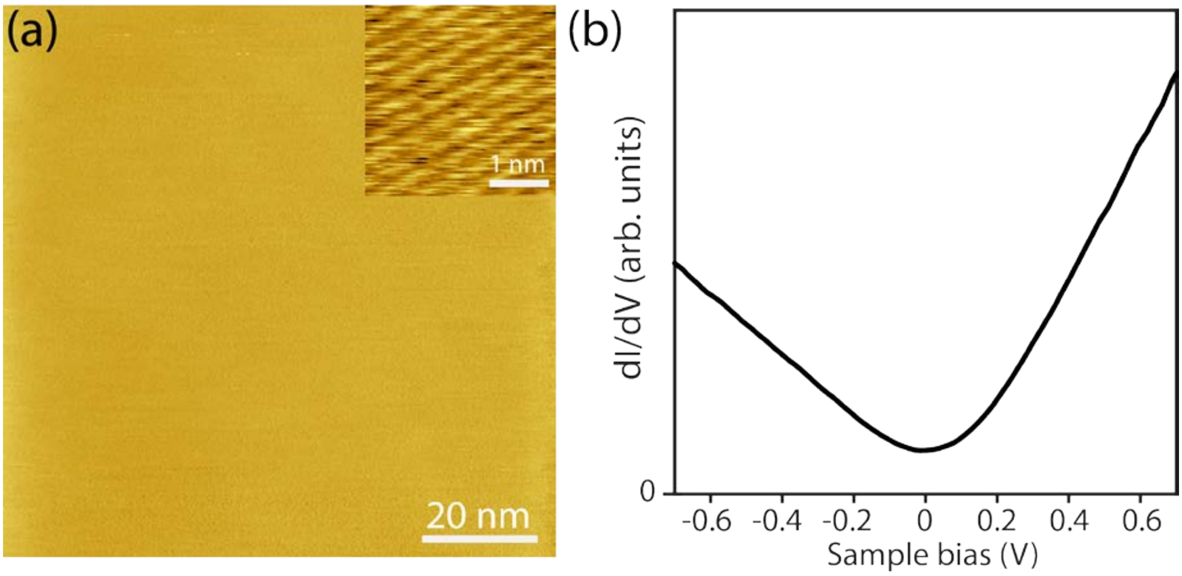

Figure 5.2: (a) Large scale scanning tunneling microscopy image (100 nm by 100 nm) of a complete germanene layer grown on MoS_2. Inset: small scale scanning tunneling microscopy image of the germanene layer. The sample bias is -1 V, and the tunnel current is 300 pA. (b) Differential conductivity of germanene. The set point values are -1.4 V and 600 pA.

obtained by introducing a bandgap of about 25 meV. This bandgap could be due to the presence of a spin-orbit gap in germanene.[27] Density functional theory calculations shown in Ref. 5 reveal that besides the linear bands at the K and K' points of the Brillouin zone, there are also two parabolic bands in the vicinity of the Fermi level at the Γ point. It is very well possible that these two parabolic bands near the Γ point are responsible for the non-zero density of states at the Dirac point; however, the non-zero density of states could also be caused by the electronic structure of the scanning tunneling microscopy tip.

Since the *dI/dV* curve shown in Figure 5.2b is averaged over 3600 different positions on the surface, it is worthwhile to have a detailed look at the spatial variation of the *dI/dV* curves. In order to do this, we have determined the exact position of the minimum of all individual *dI/dV* curves. The minimum of the V-shaped *dI/dV* curve is located at the charge neutrality point, i.e., the Dirac point. As we will show below, the Dirac point provides information on the local charge density. The dispersion relation of a two-dimensional Dirac material is $E = \hbar v_F |k|$, where $\hbar$ is the reduced Planck constant, v_F the Fermi velocity, *E* the energy of the electron, and *k* the momentum of the electron. The density of states of a two-dimensional Dirac material is given by

$$D(E) = \frac{2|E-E_D|}{\pi\hbar^2 v_F^2}, \qquad (1)$$

where E_D is the Dirac point energy. The map of the Dirac point energy can be converted into a map of the charge density by using

$$\rho(x,y) = \int_0^{E_D} \frac{2|E-E_D|}{\pi\hbar^2 v_F^2} dE = -\frac{{E_D}^2}{\pi\hbar^2 v_F^2} sign(E_D). \qquad (2)$$

In Figure 5.3a and 5.3b, spatial maps of the Dirac and charge character of a 100 nm by 100 nm germanene/MoS$_2$ are shown, respectively. The images consist of 60×60 pixels, and each pixel corresponds to a single *I(V)* curve. It should be emphasized here that we are dealing with raw data, and we have not applied any smoothening of the *I(V)* curves in order to determine the minimum of each *I(V)* curve. The spatial maps of the variation of the Dirac point and charge character reveal that the germanene sheet consists of electron and hole puddles with a typical radius of 10–20 nm embedded in an intrinsic, i.e., undoped, background. The electrostatic screening in two-dimensional Dirac materials is significantly different from electrostatic screening in conventional two-dimensional electron systems. The Dirac point varies from -30

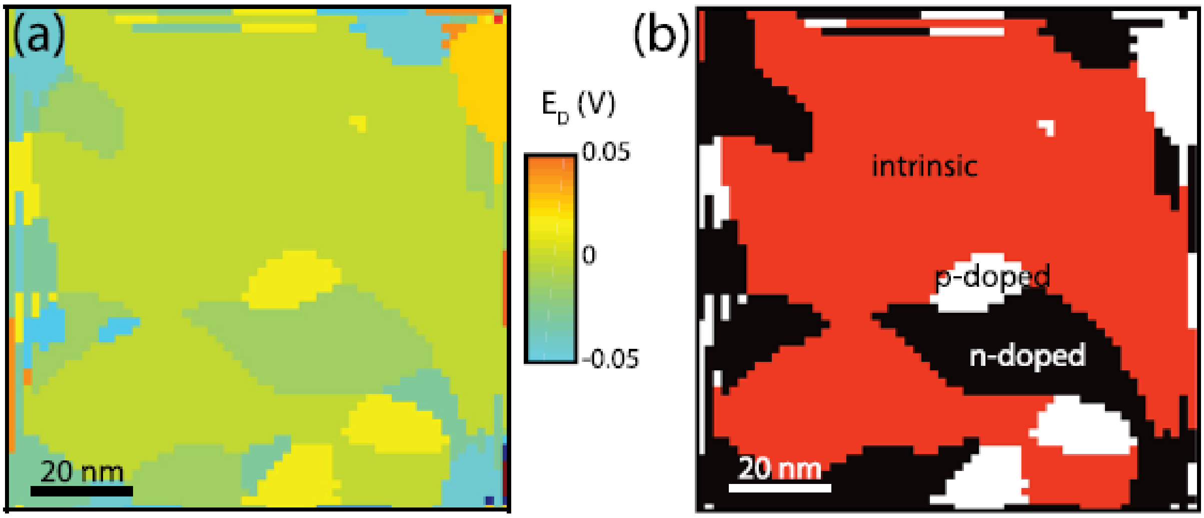

Figure 5.3: (a) Spatial map (60×60 pixels) of the Dirac point of germanene/MoS_2. The image size is 100 nm by 100 nm. The color code refers to the position of the Dirac point. (b) Spatial map (60×60 pixels) of the charge character of germanene/MoS_2 (red: intrinsic, black: n-type, and white: p-type). The image size is 100 nm by 100 nm.

meV to 15 meV corresponding to a charge fluctuation of 2.6×10^{-3} electrons/nm^2 to 6.6×10^{-4} holes/nm^2, assuming a Fermi velocity of 5×10^5 m/s.[28] Since the germanene sheet is atomically flat on a length scale exceeding the typical size of the charge puddles, we have to rule out the possibility that charge puddles are caused by structural corrugations or bending of the germanene sheet. The germanene sheet is grown and subsequently studied at ultra-high vacuum conditions, and therefore, we can also rule out the intercalation of atoms or molecules as being the cause of the charge puddles. The only remaining sources are charge donating impurities in the MoS_2 substrate. By analyzing several large-scale scanning tunneling microscopy images of our pristine and freshly cleaved MoS_2 substrate, we find a defect density of 3×10^{-3} nm^{-2}. This value compares favorably well with the charge puddle density we have determined for the germanene sheet. Based on these findings, we suggest that the charge puddles are caused by charge donating defects of the MoS_2 substrate. The typical radius of the charge puddles in germanene is about 10–20 nm. A crude estimate for the size of the charge puddle is the Thomas-Fermi screened length. In conventional two-dimensional electron systems, the density of states in energy space is constant, and therefore, the Thomas-Fermi screening length, which is inversely proportional to the density of states at the Fermi level, is constant.[29–32] In two-dimensional Dirac systems, however, the density of states is proportional to the energy. This results in a Thomas-Fermi screening length of $2\pi\kappa\hbar\upsilon_F/4e^2\sqrt{\pi n}$, where n is the charge density.[29] Assuming a Fermi velocity of 5×10^5 m/s (Refs. 26 and 33) and a charge density of ~3×10^{-3} nm^{-2} (one charge carrier per defect), we find for germanene on molybdenum disulfide a Thomas-Fermi length of ~10 nm, which is somewhat smaller than our experimental observations.

In addition, the size of the charge puddles in germanene is very comparable to the size of the charge puddles found in graphene at a comparable charge density (see Ref. 12). Please note that the charge density in Ref. 13 is substantially larger than in our case and Ref. 12, resulting in, as expected, smaller charge puddles. In a previous study,[5] we found a qualitative good agreement between the *dI/dV* spectrum and the density functional theory calculations. There is, however, an overall energy shift of about 0.3 eV between the experimental and theoretical spectra. In Ref. 5, we tentatively ascribed this energy shift to the presence of defects and/or impurities with an acceptor character. In this work, we have not found any evidence for the presence of these acceptor types of defects and/or impurities in the germanene layer, and therefore, we have to discard this interpretation.

5.4 Bandgap opening in hydrogenated germanene

In Figure 5.4a, a scanning tunneling microscopy image of a flat-topped Ge_2Pt cluster coated with a germanene layer is shown. In the inset, a small scale image of the flat-topped part of the Ge_2Pt cluster is shown. The lattice constant of the hexagonal structure is 4.2 ± 0.1 Å, which agrees well with the findings of Bampoulis et al.[23] [see Figure 5.4b]. Unfortunately, the resolution of this image is insufficient to resolve the downward buckled Ge atoms. The differential conductivity is shown in Figure 5.4c. The observed V-shaped differential conductivity is in good agreement with the results obtained by Zhang et al.[24]

Upon the exposure of the germanene sheet to 100 L of atomic hydrogen at room temperature, the (1×1) hexagonal structure of germanene changes into a (2×2) hexagonal structure [see Figure. 5.5a]. The (2×2) hexagonal structure still exhibits some defects and adsorbates. The line scan displayed in Figure. 5.5b shows a lattice constant of 0.84 nm, i.e., two times the lattice constant of germanene. The differential conductivity is shown in Figure 5.5c. The hydrogenation results in the opening of a small bandgap of about 0.2 eV. Based on the observed (2×2) structure and the small bandgap opening, we suggest that only half of the upward buckled Ge atoms are hydrogenated, resulting in a hydrogen coverage of 1/2 monolayer (at 1 monolayer coverage, all the Ge atoms of the upward buckled hexagonal sub-lattice of the germanene sheet are hydrogenated). Upon further exposure to atomic hydrogen, the (2×2) structure vanishes and the bandgap opens further.

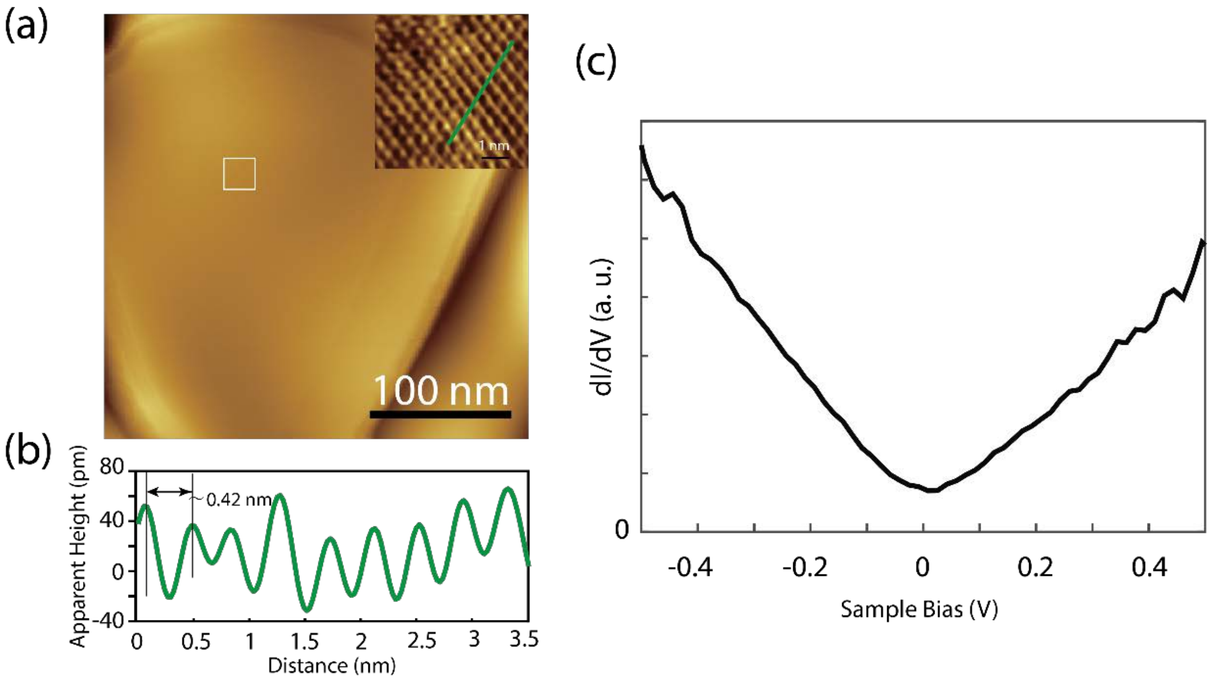

Figure 5.4: (a) Scanning tunneling microscopy image of a germanene coated flat-topped Ge_2Pt cluster. Sample bias: -1.5 V and tunneling current: 0.6 nA. Inset: small scale image of the flat-topped part of the germanene coated flat-topped Ge_2Pt cluster. Sample bias: 0.4 V and tunneling current: 0.4 nA. (b) Line profile of the line shown in the inset of graph (a). (c) Differential conductivity (*dI/dV*) of the germanene coated flat-topped Ge_2Pt cluster. Set points: sample bias -1.5 V and tunneling current 1.0 nA.

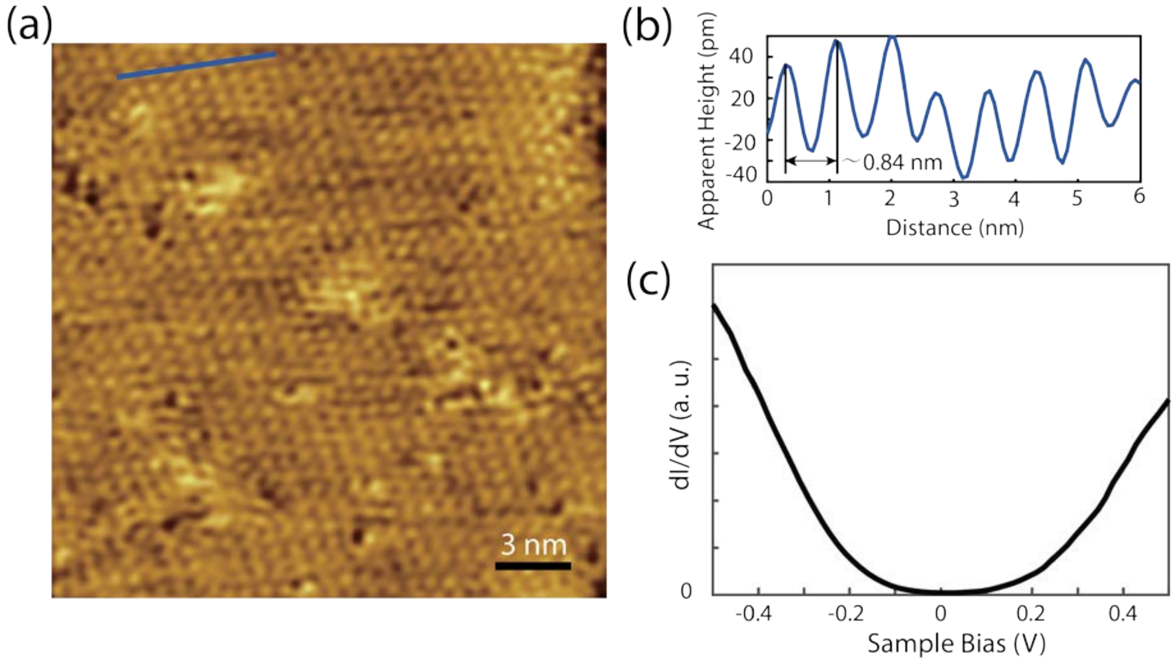

Figure 5.5: (a) Scanning tunneling microscopy image of a partly hydrogenated germanene sheet. The lattice constant of the hexagonal structure is 0.84 nm, i.e., twice the value of the pristine germanene sheet. Sample bias: -1.5 V and tunneling current: 1.0 nA. Hydrogen exposure of 100 L. (b) Line profile of the line shown in graph (a). (c) Differential conductivity of the partly hydrogenated germanene. Set points: sample bias -1.0 V and tunneling current 0.9 nA.

In Figure 5.6b the differential conductivity of the hydrogenated germanene after an exposure of 9000 L is shown. The bandgap opening amounts about 0.5 eV, and the hydrogenated germanene has become slightly n-type. The surface structure exhibits an increase in roughness and disorder, which we ascribe to the intercalation of hydrogen atoms. An scanning tunneling microscopy image is shown in Figure 5.6a. The height variation in this image is about 1 nm. Despite numerous attempts, we were unable to achieve atomically resolved scanning tunneling microscopy images, which is probably caused by the increase in roughness and disorder. The exposure to more atomic hydrogen leads to a further increase in the roughness and size of the bandgap. As a final remark, we would like to emphasize that we have not observed any significant spatial variation of the bandgap, indicating that the bandgap cannot be explained by a spatially varying Dirac point.[34] The hydrogenation of germanene and silicene has been studied quite extensively, see Refs. 20 and 34–36 and Refs. 37 and 38 for several theoretical and experimental articles, respectively. Houssa et al.[20] calculated the electronic band structure

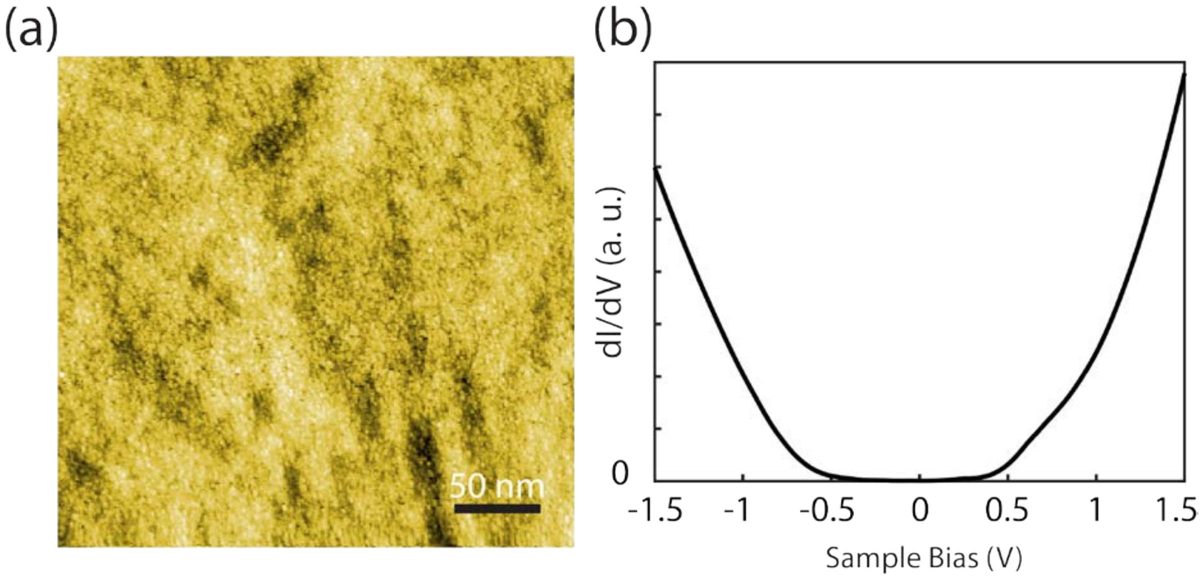

Figure 5.6: (a) Scanning tunneling microscopy image of the fully hydrogenated germanene sheet. Image size 300 nm×300 nm, sample bias -0.8 V, and tunnel current 0.9 nA. (b) Differential conductivity of a fully hydrogenated germanene (1 monolayer of hydrogen). Set points: sample bias -1.5 V and tunneling current 0.9 nA. The hydrogen exposure is 9000 L.

of germanane using first-principles total energy calculations based on the density functional theory. They found that the bandgap in germanane is direct, independent of the exact atomic configuration, making this material an appealing candidate for optoelectronic applications. Wang et al.[35] theoretically studied the properties of half-hydrogenated germanene. These authors found that half-hydrogenated germanene is stable and has a direct bandgap. They also pointed out that the buckling as well as the lattice constant of germanene increases upon hydrogenation. Nijamudheen et al.[36] demonstrated that the buckling of germanene results in an enhanced chemical reactivity of germanene for hydrogen. To date, there are, unfortunately, no experimental reports on the hydrogenation of a single sheet of germanene. Luckily, a few experimental studies on the hydrogenation of silicene have been performed recently. The first experimental report on the hydrogenation is by Qiu et al.[37] These authors studied the hydrogenation of a silicene layer synthesized on a Ag(111) substrate using scanning tunneling microscopy and density functional theory calculations. They focused on the (3×3) silicene structure [a (3×3) silicene supercell is commensurable with a (4×4) cell of the Ag(111) surface]. Six out of the 18 Si atoms of a (3×3) silicene unit cell are located on-top, or almost on-top, of a Ag atom and are therefore found in the upward buckled position. The other 12 atoms are found in a downward buckled position. Upon hydrogenation, the regular (3×3) cell, also referred to as the α-(3×3) structure, converts to a γ-(3×3) structure. This γ-(3×3) structure is composed of two distinctly different half unit cells, where one half unit cell has 6 and the other half unit cell has only one upward buckled Si atom.[37] The hydrogen atoms only adsorb on these upward buckled Si atoms, resulting in a saturation coverage of 7/18 monolayer. The hydrogen adsorption favors the sp^3 hybridization, leading to an enhancement of the upward buckling and lattice constant. In a second study, Qiu et al.[38] studied the hydrogenation of the $(2\sqrt{3}\times2\sqrt{3})R30^{o}$ silicene phase, which is also commonly found on the Ag(111) surface. In this case, the hydrogen atoms only adsorb on one of the two sublattices of silicene, yielding a perfect half-hydrogenated (1×1) structure. Based on our experimental results and the available theoretical and experimental data, we arrive at the description of the hydrogenation process of germanene coated Ge_2Pt crystals. At small hydrogen exposures, the hydrogen atoms only occupy the upward buckled Ge atoms. The adsorption of the hydrogen atom on an upward buckled Ge atom leads to an increase in the buckling as well as a small expansion of the surface lattice constant of germanene. The adsorption of hydrogen leads to the development of a compressive surface stress in the germanene sheet. In order to relieve this surface stress, it is energetically favorable to maximize the next-nearest distance of the hydrogenated Ge atoms. At a coverage of 1/2 monolayer, this results in a (2×2) structure. The next phase of the hydrogenation (1/2 to 1 monolayer) process proceeds substantially slower since now also the energetically unfavorable upward buckled Ge atoms need to be hydrogenated. This results in a further increase in the compressive surface stress. Eventually, the germanene sheet becomes fully hydrogenated and exhibits a sizeable bandgap of 0.5 eV. Upon further exposure to hydrogen, we anticipate that hydrogen atoms start to intercalate underneath the half-hydrogenated germanene sheet, leading to an increase in the roughness and a further opening of the bandgap.

5.5 Conclusions

we have studied the charge inhomogeneities of germanene grown on MoS_2. The charge fluctuations in germanene have been mapped out by using a Dirac point map. Spatial maps of the Dirac point and the charge character reveal that the germanene sheet consists of electrons and hole puddles with a typical radius of 10–20 nm embedded in an intrinsic, i.e., undoped, background. The typical charge per puddle is of the order of one electron or hole. The defect density of MoS_2 is determined by the analysis of several large-scale scanning tunneling microscopy images and compares very well with the charge density of the germanene sheet.

We found strong indications that the charge puddles in germanene are caused by charge-donating defects and impurities in the MoS_2 substrate. Our results demonstrate that even in van der Waals heteroepitaxy, the quality of the substrate plays a key role. Charge donating defects or impurities result in electronic inhomogeneities in the two-dimensional material. In addition, hydrogenation of germanene, synthesized on Ge_2Pt, results in the opening of a bandgap of about 0.5 eV. At a fractional hydrogen coverage, the (1×1) germanene structure converts to a (2×2) structure with a bandgap opening of about 0.2 eV. A further increase in the hydrogen exposure leads to vanishing of the (2×2) structure and an increase in the bandgap opening to about 0.5 eV. Eventually, the roughness and disorder of the germanane sheet increase, which we ascribe to the intercalation of atomic hydrogen.

Bibliography

[1] Novoselov, K. S.; Geim, A. K.; Morozov, S. V.; Jiang, D.; Zhang, Y.; Dubonos, S. V.; Grigorieva, I. V.; Firsov, A. A. Electric Field Effect in Atomically Thin Carbon Films. *Science* **2004**, *306* (5696), 666–669.

[2] Geim, A. K.; Novoselov, K. S. The Rise of Graphene. *Nat. Mater.* **2007**, *6* (3), 183–191.

[3] Vogt, P.; De Padova, P.; Quaresima, C.; Avila, J.; Frantzeskakis, E.; Asensio, M. C.; Resta, A.; Ealet, B.; Le Lay, G. Silicene: Compelling Experimental Evidence for Graphenelike Two-Dimensional Silicon. *Phys. Rev. Lett.* **2012**, *108* (15), 155501.

[4] Fleurence, A.; Friedlein, R.; Ozaki, T.; Kawai, H.; Wang, Y.; Yamada-Takamura, Y. Experimental Evidence for Epitaxial Silicene on Diboride Thin Films. *Phys. Rev. Lett.* **2012**, *108* (24), 245501.

[5] Zhang, L.; Bampoulis, P.; Rudenko, A. N.; Yao, Q.; van Houselt, A.; Poelsema, B.; Katsnelson, M. I.; Zandvliet, H. J. W. Structural and Electronic Properties of Germanene on MoS_2. *Phys. Rev. Lett.* **2016**, *116* (25), 256804.

[6] Acun, A.; Zhang, L.; Bampoulis, P.; Farmanbar, M.; van Houselt, A.; Rudenko, A. N.; Lingenfelder, M.; Brocks, G.; Poelsema, B.; Katsnelson, M. I.; et al. Germanene: The Germanium Analogue of Graphene. *J. Phys. Condens. Matter* **2015**, *27* (44), 443002.

[7] Zhu, F.; Chen, W.; Xu, Y.; Gao, C.; Guan, D.; Liu, C.; Qian, D.; Zhang, S.-C.; Jia, J. Epitaxial Growth of Two-Dimensional Stanene. *Nat. Mater.* **2015**, *14* (10), 1020–1025.

[8] Takeda, K.; Shiraishi, K. Theoretical Possibility of Stage Corrugation in Si and Ge Analogs of Graphite. *Phys. Rev. B* **1994**, *50* (20), 14916–14922.

[9] Guzmán-Verri, G. G.; Lew Yan Voon, L. C. Electronic Structure of Silicon-Based Nanostructures. *Phys. Rev. B* **2007**, *76* (7), 075131.

[10] Cahangirov, S.; Topsakal, M.; Aktürk, E.; Şahin, H.; Ciraci, S. Two- and One-Dimensional Honeycomb Structures of Silicon and Germanium. *Phys. Rev. Lett.* **2009**, *102* (23), 236804.

[11] Martin, J.; Akerman, N.; Ulbricht, G.; Lohmann, T.; Smet, J. H.; von Klitzing, K.; Yacoby, A. Observation of Electron–Hole Puddles in Graphene Using a Scanning Single-Electron Transistor. *Nat. Phys.* **2008**, *4* (2), 144–148.

[12] Zhang, Y.; Brar, V. W.; Girit, C.; Zettl, A.; Crommie, M. F. Origin of Spatial Charge Inhomogeneity in Graphene. *Nat. Phys.* **2009**, *5* (10), 722–726.

[13] Martin, S. C.; Samaddar, S.; Sacépé, B.; Kimouche, A.; Coraux, J.; Fuchs, F.; Grévin, B.; Courtois, H.; Winkelmann, C. B. Disorder and Screening in Decoupled Graphene on a Metallic Substrate. *Phys. Rev. B* **2015**, *91* (4), 041406.

[14] Deshpande, A.; Bao, W.; Miao, F.; Lau, C. N.; LeRoy, B. J. Spatially Resolved Spectroscopy of Monolayer Graphene on ${\text{SiO}}_{2}$. *Phys. Rev. B* **2009**, *79* (20), 205411.

[15] Gibertini, M.; Tomadin, A.; Polini, M.; Fasolino, A.; Katsnelson, M. I. Electron Density Distribution and Screening in Rippled Graphene Sheets. *Phys. Rev. B* **2010**, *81* (12), 125437.

[16] Gibertini, M.; Tomadin, A.; Guinea, F.; Katsnelson, M. I.; Polini, M. Electron-Hole Puddles in the Absence of Charged Impurities. *Phys. Rev. B* **2012**, *85* (20), 201405.

[17] Rutter, G. M.; Jung, S.; Klimov, N. N.; Newell, D. B.; Zhitenev, N. B.; Stroscio, J. A. Microscopic Polarization in Bilayer Graphene. *Nat. Phys.* **2011**, *7* (8), 649–655.

[18] Bianco, E.; Butler, S.; Jiang, S.; Restrepo, O. D.; Windl, W.; Goldberger, J. E. Stability and Exfoliation of Germanane: A Germanium Graphane Analogue. *ACS Nano* **2013**, *7* (5), 4414–4421.

[19] Lew Yan Voon, L. C.; Sandberg, E.; Aga, R. S.; Farajian, A. A. Hydrogen Compounds of Group-IV Nanosheets. *Appl. Phys. Lett.* **2010**, *97* (16), 163114.

[20] Houssa, M.; Scalise, E.; Sankaran, K.; Pourtois, G.; Afanas’ev, V. V.; Stesmans, A. Electronic Properties of Hydrogenated Silicene and Germanene. *Appl. Phys. Lett.* **2011**, *98* (22), 223107.

[21] Madhushankar, B. N.; Kaverzin, A.; Giousis, T.; Potsi, G.; Gournis, D.; Rudolf, P.; Blake, G. R.; van der Wal, C. H.; van Wees, B. J. Electronic Properties of Germanane Field-Effect Transistors. *2D Mater.* **2017**, *4* (2), 021009.

[22] Zandvliet, H. J. W. The Ge(001) Surface. *Phys. Rep.* **2003**, *388* (1), 1–40.

[23] Bampoulis, P.; Zhang, L.; Safaei, A.; Gastel, R. van; Poelsema, B.; Zandvliet, H. J. W. Germanene Termination of Ge_2Pt Crystals on Ge(110). *J. Phys. Condens. Matter* **2014**, *26* (44), 442001.

[24] Zhang, L.; Bampoulis, P.; van Houselt, A.; Zandvliet, H. J. W. Two-Dimensional Dirac Signature of Germanene. *Appl. Phys. Lett.* **2015**, *107* (11), 111605.

[25] Bampoulis, P.; van Bremen, R.; Yao, Q.; Poelsema, B.; Zandvliet, H. J. W.; Sotthewes, K. Defect Dominated Charge Transport and Fermi Level Pinning in MoS_2 /Metal Contacts. *ACS Appl. Mater. Interfaces* **2017**, *9* (22), 19278–19286.

[26] Addou, R.; Colombo, L.; Wallace, R. M. Surface Defects on Natural MoS_2. *ACS Appl. Mater. Interfaces* **2015**, *7* (22), 11921–11929.

[27] Liu, C.-C.; Feng, W.; Yao, Y. Quantum Spin Hall Effect in Silicene and Two-Dimensional Germanium. *Phys. Rev. Lett.* **2011**, *107* (7), 076802.

[28] Liu, C.-C.; Jiang, H.; Yao, Y. Low-Energy Effective Hamiltonian Involving Spin-Orbit Coupling in Silicene and Two-Dimensional Germanium and Tin. *Phys. Rev. B* **2011**, *84* (19), 195430.

[29] Das Sarma, S.; Adam, S.; Hwang, E. H.; Rossi, E. Electronic Transport in Two-Dimensional Graphene. *Rev. Mod. Phys.* **2011**, *83* (2), 407–470.

[30] Samaddar, S.; Yudhistira, I.; Adam, S.; Courtois, H.; Winkelmann, C. B. Charge Puddles in Graphene near the Dirac Point. *Phys. Rev. Lett.* **2016**, *116* (12), 126804.

[31] Katsnelson, M. I. Nonlinear Screening of Charge Impurities in Graphene. *Phys. Rev. B* **2006**, *74* (20), 201401.

[32] John, R.; Merlin, B. Optical Properties of Graphene, Silicene, Germanene, and Stanene from IR to Far UV – A First Principles Study. *J. Phys. Chem. Solids* **2017**, *110*, 307–315.

[33] Ezawa, M. Monolayer Topological Insulators: Silicene, Germanene, and Stanene. *J. Phys. Soc. Jpn.* **2015**, *84* (12), 121003.

[34] Zhang, Y.; Brar, V. W.; Wang, F.; Girit, C.; Yayon, Y.; Panlasigui, M.; Zettl, A.; Crommie, M. F. Giant Phonon-Induced Conductance in Scanning Tunnelling Spectroscopy of Gate-Tunable Graphene. *Nat. Phys.* **2008**, *4* (8), 627–630.

[35] Wang, X.-Q.; Li, H.-D.; Wang, J.-T. Induced Ferromagnetism in One-Side Semihydrogenated Silicene and Germanene. *Phys. Chem. Chem. Phys.* **2012**, *14* (9), 3031–3036.

[36] Nijamudheen, A.; Bhattacharjee, R.; Choudhury, S.; Datta, A. Electronic and Chemical Properties of Germanene: The Crucial Role of Buckling. *J. Phys. Chem. C* **2015**, *119* (7), 3802–3809.

[37] Qiu, J.; Fu, H.; Xu, Y.; Oreshkin, A. I.; Shao, T.; Li, H.; Meng, S.; Chen, L.; Wu, K. Ordered and Reversible Hydrogenation of Silicene. *Phys. Rev. Lett.* **2015**, *114* (12), 126101.

[38] Qiu, J.; Fu, H.; Xu, Y.; Zhou, Q.; Meng, S.; Li, H.; Chen, L.; Wu, K. From Silicene to Half-Silicane by Hydrogenation. *ACS Nano* **2015**, *9* (11), 11192–11199.

Impact of defects and air-stability on $HfSe_2$

6.1 Introduction

Since the first single-layer MoS_2 transistor was fabricated and characterized in 2011,[1] it has triggered many scientists to search for transition metal dichalcogenides (TMDs)-based applications. Two-dimensional TMDs have been widely studied because of their appealing physical (1T or 2H phase) and electrical properties (ranging from metallic to half-metallic to semiconducting and even superconducting).[2-4] For instance, MoS_2 has a thickness dependent bandgap, with a transition of an indirect to direct bandgap in case that the thickness is reduced to a single layer.[5] In addition, superconductivity has been observed in both bulk 1T-MoS_2[6] and pristine $2H_a$-MoS_2[7]. However, compared to Mo or W chalcogenides, $HfSe_2$, has not been received that much of attention. Single-layer $HfSe_2$ is a material with an octahedral structure with an indirect band gap of ~1 eV,[8-10] which makes it an appealing candidate for semiconductor device applications.

$HfSe_2$-based prototype transistors have been realized and investigated by several groups.[9, 11-13] A high on/off current ratio, exceeding 10^6, was found, satisfying the requirement for effective switching in digital logic transistors.[11] The current density of a trilayer $HfSe_2$ was up to ~30 µA/µm.[9] Moreover, a phototransistor based on $HfSe_2$ has superior optoelectronic properties with an ultrafast response time and high photocurrent, which is comparable with other TMDs phototransistors.[12] However, its carrier mobility is rather low, ranging from ~0.3 to ~6.5 $cm^2 \cdot V^{-1} \cdot S^{-1}$, i.e., three orders of magnitude lower than the predicted value of ~3500 $cm^2 \cdot V^{-1} \cdot S^{-1}$ at room temperature.[14]

Besides device optimization, such as the inclusion of dielectric layers and the selection of proper metal contacts, the quality of the material should be also improved, in order to obtain properly operating devices. It is known that TMD materials suffer from a large number of intrinsic defects, located either in the transition metal layer or the chalcogenide layer.[15-17] Moreover, the air stability of $HfSe_2$ needs to be investigated too. These key issues, i.e. intrinsic defects and air stability, have to be considered in order to properly evaluate the application prospects of $HfSe_2$.

Defects often play a significant role in determining the electronic behavior in TMDs.[18-23] Intrinsic defects dominate the contact resistance between metal contacts and TMDs[19] and can act as scattering centers[20], degrading the charge carrier mobility. Defects are also expected to dominate the surface conductivity of $HfSe_2$ leading to the very low carrier mobilities. It is therefore essential to scrutinize the structural and electronic characteristics of $HfSe_2$ and explore the reasons of the poor device performance. We have used scanning tunneling microscopy and spectroscopy (STM/STS) to study variations in the structure and electronic local density of states (LDOS) of the $HfSe_2$ surface. We have found several types of defects located either in the uppermost Se layer or Hf layer. Furthermore, we have used conductive atomic force microscopy (C-AFM) to measure the influence of these defects on the Schottky barrier height formed with different metal contacts and possible partial Fermi level pinning effects, following the same approach as in ref [21] for MoS_2.

In addition, $HfSe_2$ crystals are not stable against oxidation at ambient conditions, implying this air-sensitive $HfSe_2$ surface is detrimental for many applications. Gioele et al.[24] found a preferential reaction of oxygen with the Hf atoms rather than with the Se atoms, leading to the formation of a HfO_2 layer. In principle the poor air stability of $HfSe_2$ should limit its application in electronic devices. However, HfO_2 is a high-κ dielectric oxide, which has been frequently used as a top gate layer for field-effect transistors.[1, 25] In particular, native HfO_2 layer can effectively suppress the interfacial charge trap states at the $HfSe_2/HfO_2$ interface , which is very beneficial for device performance.[9] Therefore, it is important to properly understand the oxidation of $HfSe_2$. Unlike earlier Raman and XPS studies[8,13,24], the combination of STM and C-AFM allow us to study the oxidation dynamics and evolution of the electrical properties of $HfSe_2$ with a high spatial resolution.

6.2 Experimental Details

The $HfSe_2$ crystal was purchased from HQ Graphene (Groningen, The Netherlands). The samples were cleaned by mechanical exfoliation and subsequently transferred to vacuum system as soon as possible for STM and C-AFM measurements. All the STM/STS data were obtained by room temperature scanning tunneling microscopy (Omicron STM1). The base pressure of the ultra-high vacuum system is 3×10^{-11} mbar. In order to obtain *I(V)* signals by AFM, we applied the bias voltages between the conductive tip (grounded) and $HfSe_2$ surface to read out the current values. Different conductive tips, including the Pt tips, the PtSi tips and the n-type Si tips, were used for the measurements. The resonance frequency is 4.5, 15, and 160 kHz for the Pt, PtSi, and n-type Si tips, respectively.

6.3 Surface topography and local electronic properties

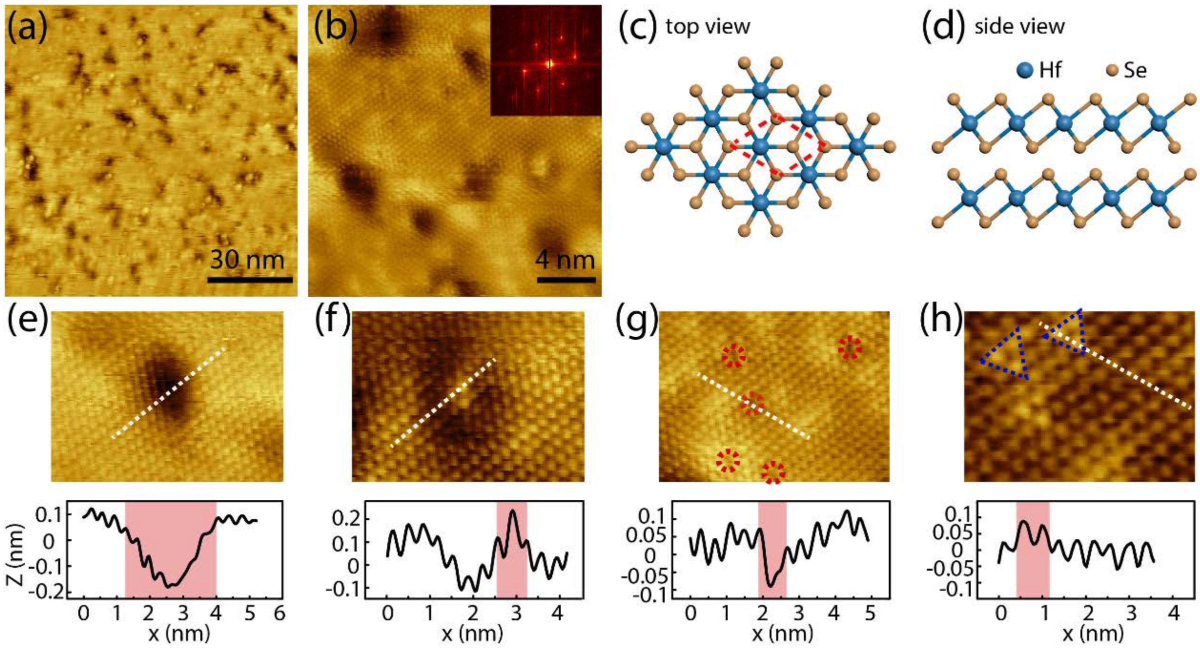

Figure 6.1: (a) Large-scale STM topography image on the $HfSe_2$ crystal (100 nm×100 nm; I_t= 0.6 nA , V_s= -0.3 V). (b) An atomically resolved image of the $HfSe_2$ surface (20 nm×20 nm; I_t= 0.6 nA , V_s= -0.4 V). The inset is the corresponding FFT image. (c) Top view, and (d) side view sketches of a bilayer $HfSe_2$. (e-h) Atomic scale STM images and line scans of defects on $HfSe_2$ (I_t= 0.6 nA , V_s= -0.4 V).

Because of the poor air instability of $HfSe_2$, the mechanical exfoliation was done *in-situ* in the load lock of the STM system at a base pressure of 1×10^{-8} mbar. The freshly cleaved sample was then transferred to the main chamber of the STM for imaging. Figures 6.1a shows a large-scale STM topography image of the freshly cleaved $HfSe_2$ surface. It is clear that the surface of $HfSe_2$ is inhomogeneous, displaying a large number of defects. The density of these defects across the whole sample is about 9×10^{-11} cm^{-2}, which is substantially higher than the defect densities of MoS_2 or WSe_2,[26,27] see Figure 6.2.

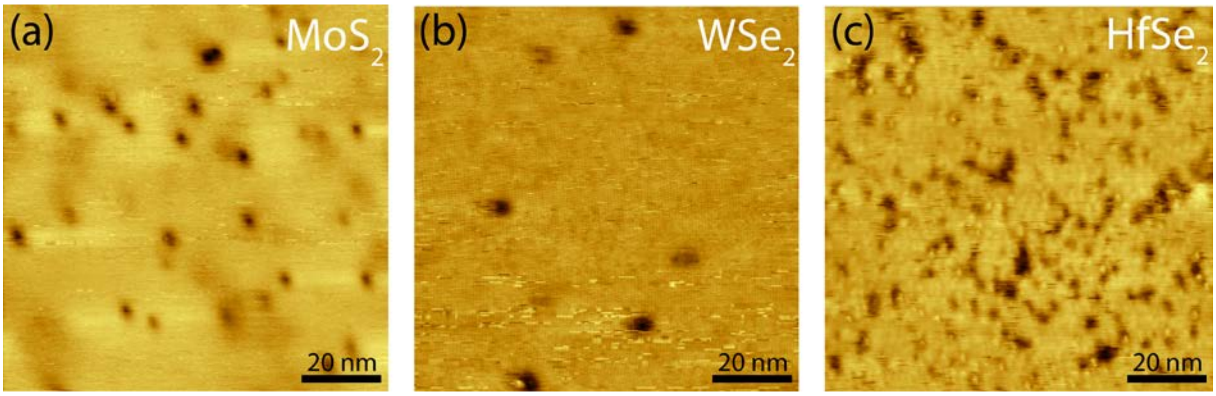

Figure 6.2: STM topography images of three different TMD surfaces, obtained by the same scanning tunneling microscopy settings. The image size is 100 nm×100 nm, sample bias voltage is -0.3 V and tunnel current is 0.6 nA.

Such a high density of defects makes it very difficult to find nanometer sized defect-free regions. By zooming in at parts where the surface structure is still intact, we have acquired the atomic lattice of the surface, as shown in Figure 6.1b. The lattice constant, as extracted from the images is 0.378 nm (see the inset in Figure 6.1b for a fast Fourier transform). This value is in good agreement with the previously reported lattice constant.[28] Figure 6.1c and 6.1d shows the structural model of bilayer $HfSe_2$. The interlayer distance of the $HfSe_2$ crystal is ~0.614 nm.[29] The single-layer $HfSe_2$ is constituted of a top-Se, center-Hf, and bottom-Se atom layer, respectively. These three atom layers acquire an octahedral configuration. In our atomically resolved STM images only the top-Se atom layer is observed. The unit cell formed by the nearest four neighbor Se atoms corresponds to the red dashed contour marked in the top view of the structural model.

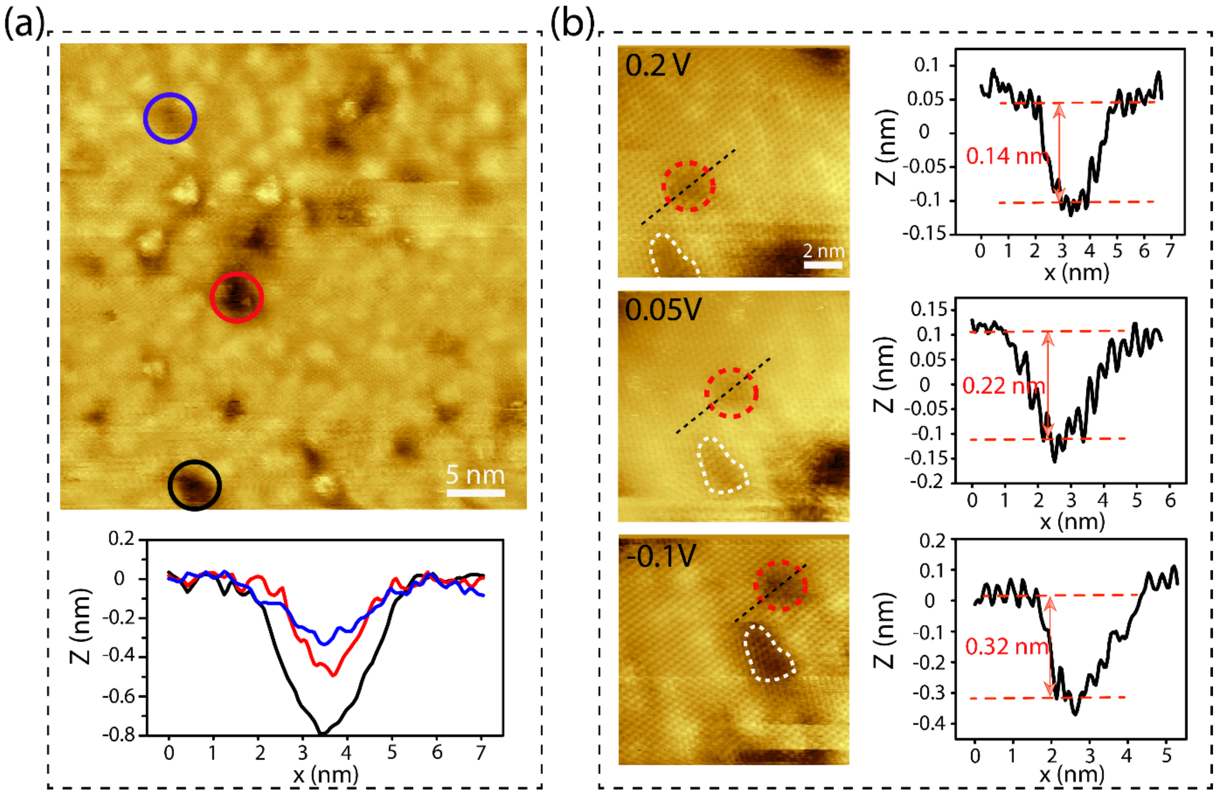

Figure 6.3: Height of the depression for dark defects. Panel (a): three different positions, marked by the blue, red, and black rings. The heights are 0.3, 0.5, and 0.8nm, respectively. Panel (b): The exact height of the same dim dark defect marked by the dashed red contour, depends on the sample bias voltage.

The most abundant defects are shown in Figure 6.1e-f, which are dark defects, bright defects, and atom vacancies, respectively. The dark defect in Figure 6.1e has a depth measured by the line profile of around 0.3 nm. Depending on the defect position and sample bias voltage, the height of this depression varies from around 0.1 nm to 0.8 nm, as described in detail in the Figure 6.3. It is worth noting that three types of dark defects have been identified based on their topographical features: 1) a very dark hole-like defect with the depression depth of ≥ 0.7 nm, 2) a less dark defect with the depression depth ranging from 0.5 nm to 0.7 nm and 3) a dim dark defect with a visible continuous lattice periodicity and the depression depth of ≤ 0.5 nm, see Figure 6.4). The third type of defects (dim dark) have a density of 5×10^{11} cm^{-2}. Defects with a similar appearance are also reported to exist on other TMD crystals, either on pristine surfaces or after ion bombardment.[26, 27, 30-32] Since our $HfSe_2$ sample was only treated with scotch-tape cleavage before scanning, the ion bombardment induced defects can be ignored here. The dark defects have been interpreted to be caused by poor growth conditions. Its appearance is the result of electron depletion caused by the Coulomb repulsive potential around the Se atom complex or the acceptor impurity near the surface.[27, 33] The continuation of the lattice periodicity suggests that this type of feature is due to the absence of a Se atom.

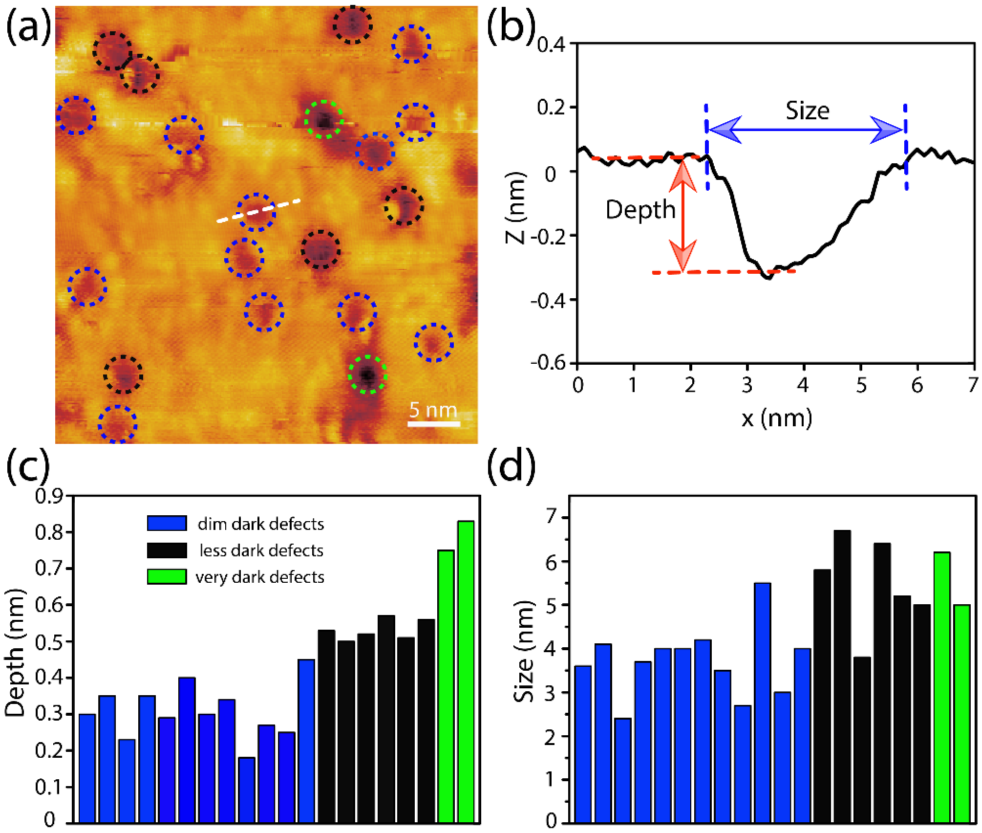

Figure 6.4: The three types of dark defects. (a) STM topography image of HfSe$_2$ surface, the image size is 40 nm × 40 nm, sample bias voltage is -0.4 V and tunnel current is 0.6 nA. The three types of defects, marked by the blue, black, and green contours, are corresponding to the dim dark defect, less dark defects and very dark defects, respectively; (b) The depth and size of the defect marked by the dashed white line; (c) Depth of the dark defects from (a); (d) Size of the dark defects from (a).

In addition to these abundant dark defects, we have found several other types of defects on the surface. Figure 6.1f presents a hillock-like defect with a density of ~2.5×10^{11} cm^{-2}, probably caused by an adatom. The adatom could be for instance a Se atom, or another impurity atom such as Li, Na, K and Re.[32,34] Moreover, several single-atom vacancies are also found, as shown in Figure 1g. The corresponding cross section reveals the absence of an atom in the lattice. Such single atom vacancy has a density of ~0.5×10^{11} cm^{-2}. We also report a new type of defect with a triangular shape, shown in Figure 1h. It has a similar appearance as the 3×3 charge density wave superlattice observed in NbSe$_2$.[35] Since the charge density wave transition temperature of HfSe$_2$ is rather low we can exclude this interpretation here. It has been shown that HfSe$_2$ is a suitable host material for extrinsic dopant atoms,[36] suggesting that the bright defects might be a result of the intercalation of impurities.

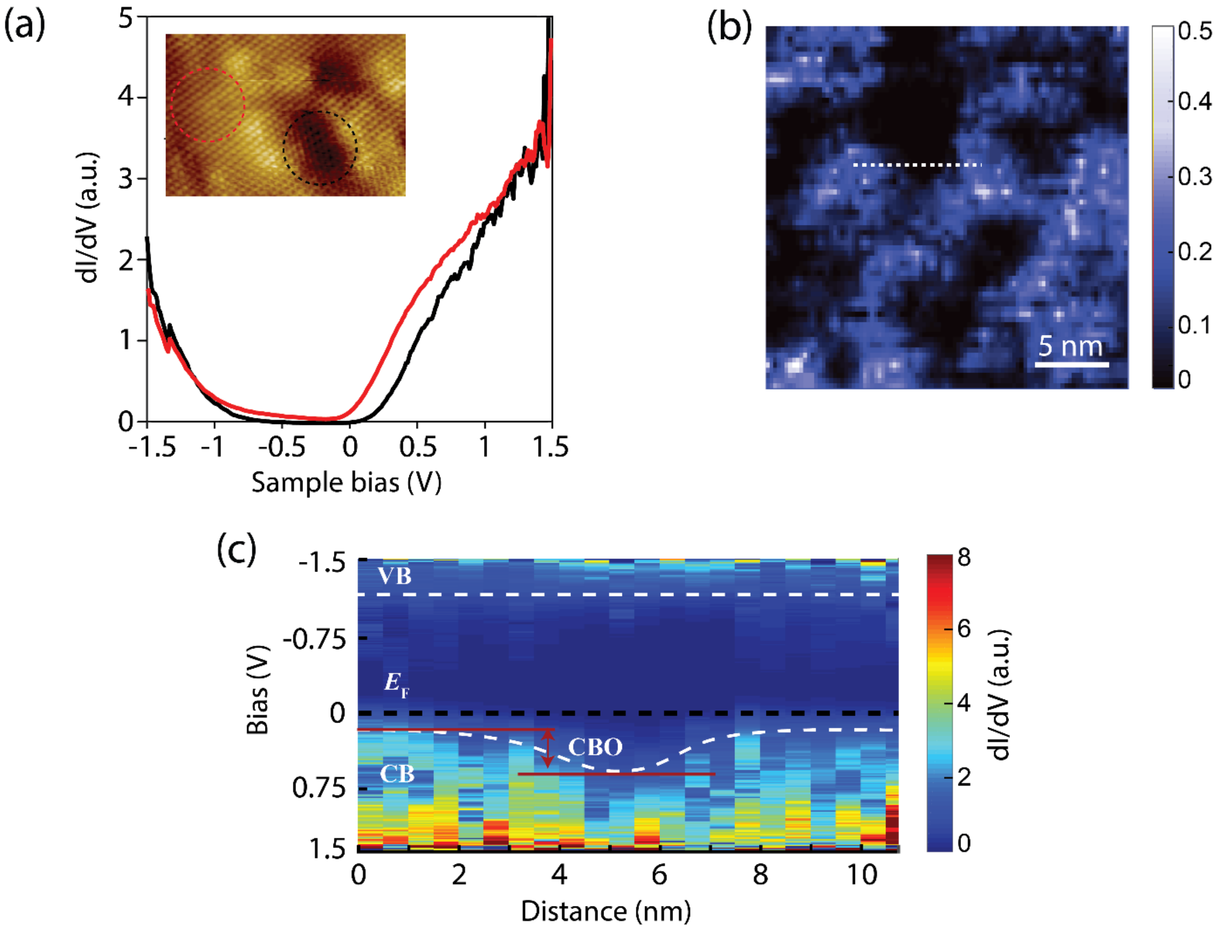

Figure 6.5: Scanning tunneling spectroscopy results of the HfSe$_2$ surface (a) *dI/dV* spectra at different regions, Inset: STM image showing the locations where the spectroscopy data were taken from. (b) *dI/dV* map of HfSe$_2$ (100 nm×100 nm; I_t= 0.6 nA , V_s= -0.3 V). (c) Colour-coded rendering of the real space imaging of the band profile plotted in terms of *dI/dV* taken along the dashed white line in Figure 2b.

In the following section, we investigate the influence of the aforementioned defects on the local density of states of the HfSe$_2$ surface using scanning tunneling spectroscopy (STS). Figure 6.5a shows the local tunneling conductance (*dI/dV*) spectra taken at the red and black dashed circles, which correspond to the dim dark defect and the pristine region, respectively. The *dI/dV* spectra, which are proportional to the electronic local density of states (LDOS) near the Fermi level for small sample biases, are obtained by numerical differentiating 3600 current-voltage curves recorded in a 60 × 60 grid. Both recorded curves exhibit an n-type semiconducting behavior, in good agreement with previous STM and electrical transport measurements.[8, 11-12] The Fermi level is much closer to the conduction band (CB) than to the valence band (VB) because of the strong doping from the Se atom vacancies in the crystal. The sharp increases in the *dI/dV* spectra correspond to the CB and VB band edges. The bandgap as extracted from these curves is about 1 eV for the pristine $HfSe_2$ surface and 1.25 eV for the dim dark defects, respectively. In addition, the *dI/dV* map in Figure 6.5b illustrates the large fluctuation of the LDOS of $HfSe_2$, induced by the presence of the high density of intrinsic defects on $HfSe_2$ surface. The *dI/dV* spectra along the dashed white line in Figure 6.5b are taken to determine the real space band profiles. As shown in Figure 6.5c, there is a conduction band offset (CBO) between the conduction band minima of the defect and the pristine surface that amounts to ~0.2 eV. In principle, S or Se atom vacancies in TMDs can lead to enhancement of the LDOS in the conduction band because of the broken covalent bonds, leading to a reduction of the CBM.[37, 38] In contrast, we observe an upward shift of the CBM. The atomically resolved STM topography images of the dim dark defects (shown in Figure 6.1e) show an intact lattice periodicity, indicating that these defects are buried under the surface. Therefore, the possible mechanism for the shift of the CBM might involve substitutional dopants, like Mo, W or Sn atoms. The presence of these substitutional atoms could be caused by the crystal growth process.. The brighter LDOS signal in Figure 6.5b is most probably related to the presence of triangular defects, however their considerable smaller size does not allow for accurately capturing their influence on the surface.

Spatial maps of the LDOS recorded at various energies on the same $HfSe_2$ surface location as discussed in Figure 6.5b, are shown in Figure 6.6. These *dI/dV* maps are recorded simultaneously with the topographic image. The dark (red arrows) and bright (green arrows) regions correspond to the dark defects and the pristine areas, respectively. In the vicinity of the Fermi level ($-0.15\ \text{eV} \leq E \leq 0.15\ \text{eV}$), large inhomogeneities of the LDOS are clearly observed. The pristine $HfSe_2$ has a higher conductance, which is in accordance with the *dI/dV* curves shown in Figure 6.5a. For energies is far away from Fermi level, the distribution of the LDOS becomes more and more uniform.

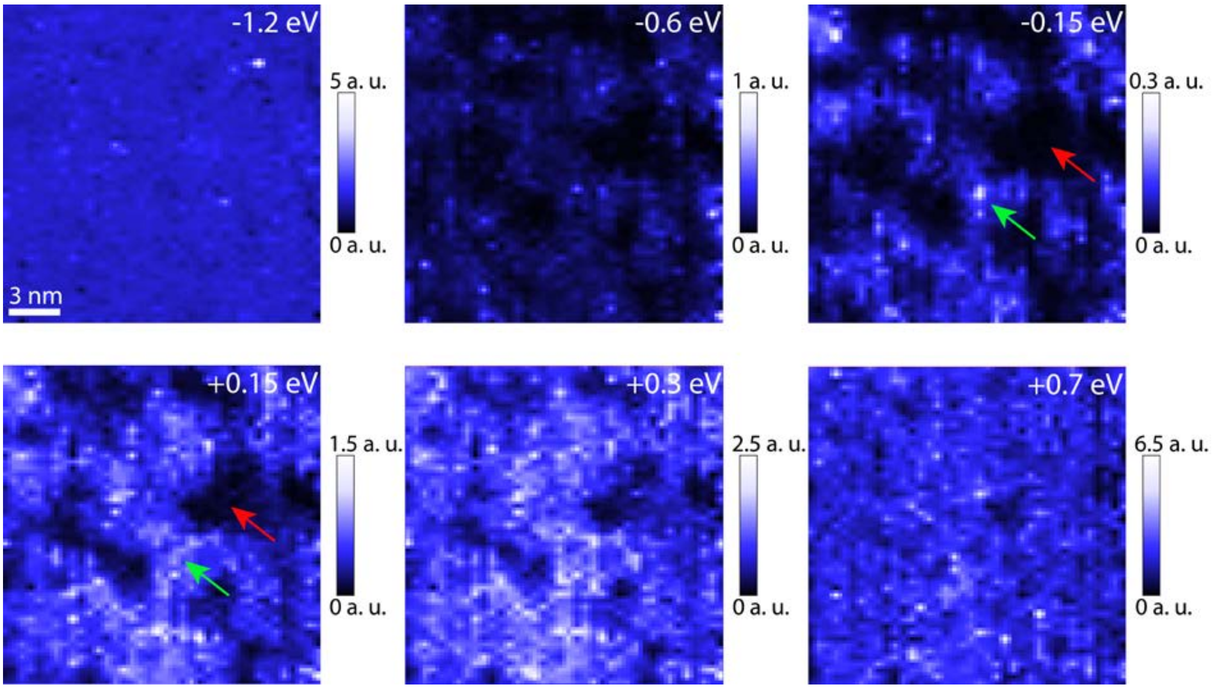

Figure 6.6: Spatially resolved density-of-state maps obtained on $HfSe_2$ surface at different energies (20 nm×20 nm, I_t= 0.5 nA), taken at -1.2 V, -0.6 V, -0.15 V, +0.15 V, +0.3 V and +0.7 V, respectively.

6.4 Schottky barrier height and Fermi level pinning of the $HfSe_2$ crystal

Owing to the moderate bandgap of around 1 eV, which is comparable to silicon, $HfSe_2$-based field effect transistors have been investigated. However, the mobility obtained in transport measurements is much lower than the theoretically predicted one.[9, 11, 13] The following reasons for the low charge carrier mobility have been put forward. Firstly, the high anisotropic electrical resistivity of $HfSe_2$ can suppress the vertical charge transport in the Ohmic regime . Secondly, the barrier at non-ideal Ohmic contacts induces large contact resistances and further limits the mobility. Thirdly, the environmental instability of $HfSe_2$ can cause degradation of the device. In addition, the existence of possible interfacial scattering and interlayer resistance could be also responsible for the low charge carrier mobility. Although a slow decay time of photocurrent in Au-contacted $HfSe_2$ phototransistor was shown to be correlated to defects and charge impurity states ,[12] the effect of defects on the charge transport of $HfSe_2$ has not yet been studied. In our STM images we have confirmed the high-density of these defects and impurities. The strong influence of the dark defects in the LDOS indicates local variations in electrical contacts.

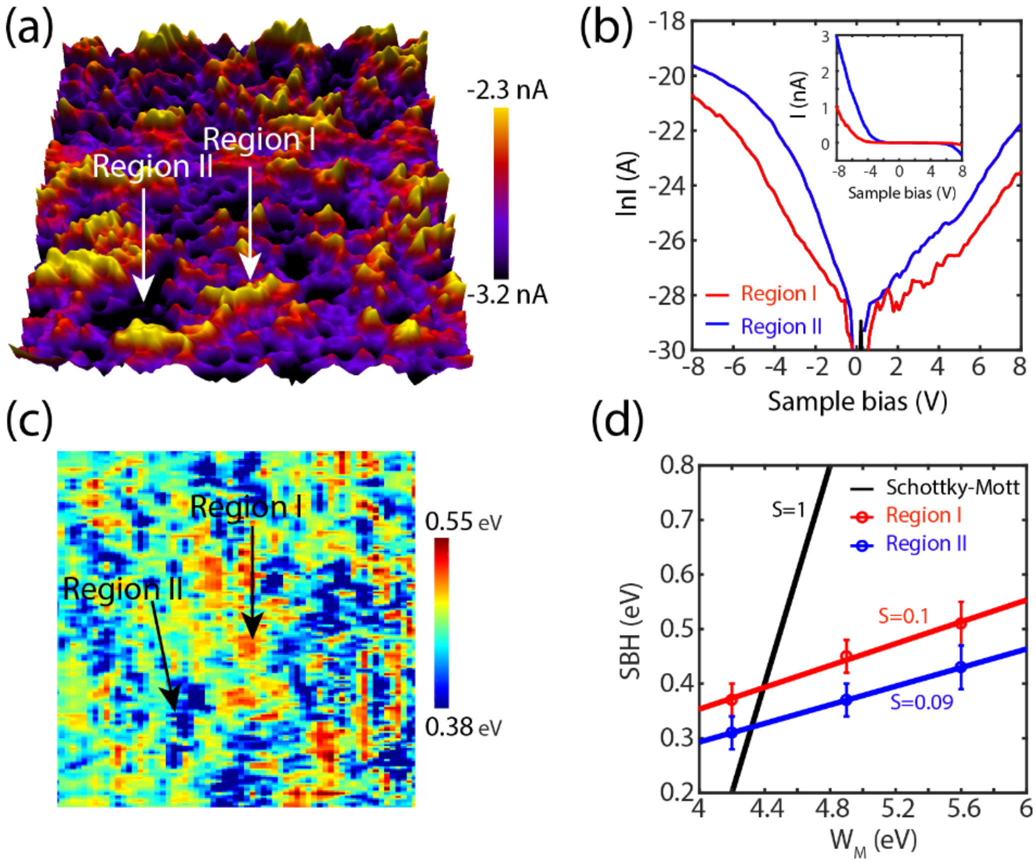

Figure 6.7: (a) A current image (600 nm × 600 nm) of the $HfSe_2$ recorded with C-AFM at a sample bias of 4.7 V. A highly doped Si tip (work function 4.2 eV) has been used. (b) The semi-logarithmic contact *I(V)* curves for region I and region II, as indicated in panel (a). Inset: the corresponding contact *I(V)* curves. (c) The extracted Schottky barrier height (SBH) map (200 nm×200 nm) of the surface extracted from *I(V)* curves, as shown in panel (b). The apparent SBH variations are attributed to the presence of defects on the sample. (d) The Schottky barrier heights of region I (red) and region II (blue) *as a function of the tip's* work functions(W_M). The pinning factor S is extracted using eq 6. The black line refers to the standard Schottky-Mott rule (see eq 5).

Since a C-AFM tip can be used as a metal nanocontact to measure simultaneously the topography image and *I*(*V*) curves, it is possible to make a metal-semiconductor (tip-$HfSe_2$) junction and obtain information on the variation in electrical resistance and contact properties induced by defects on the $HfSe_2$. Figure 6.7a shows the current map recorded with C-AFM using a highly n-doped Si tip with a work function of about 4.2 eV and a radius of curvature of 2 nm. The inhomogeneous current distribution is consistent with STM topography images.

Moreover, voltage-dependent current spectra are recorded in 128×128 grid fashion, the average curves recorded in region I and region II are shown in Figure 6.7b. We find different charge transport characteristics in region I (red line) and region II (blue line), with region II being much more conductive than region I, especially in the negative sample bias regime (see inset in Figure 6.7b). Furthermore, the *I(V)* traces reveal a rectifying behavior with an n-type Schottky barrier. The observation of an n-type Schottky barrier is reminiscent of the n-type doping of $HfSe_2$ surface. In order to understand the difference between region I and region II, we have considered thermionic emission as the main transport process. The thermionic emission current *I* is given by,

$$I = I_0 \left[\exp\left(\frac{qV}{\eta \kappa_B T}\right) - 1\right] \quad (1)$$

with

$$I_0 = AA^* T^2 \exp\left(-\frac{q\phi_B}{\kappa_B T}\right) \quad (2)$$

where I_0 is the saturation current, V is the applied bias voltage, q is the electron charge, and T is the sample temperature. A is the AFM tip contact area, calculated using the Hertz model.[39] κ_B and A^* are the Boltzmann constant and the Richardson constant, respectively. Then, the ideality factor (η) and the Schottky barrier height (Φ_B) are obtained by

$$\eta = \frac{q}{\kappa_B} \frac{dV}{d(lnI)} \quad (3)$$

and

$$\Phi_B = \frac{k_B T}{q} \ln\left(\frac{AA^* T^2}{I_0}\right). \quad (4)$$

The calculated Schottky barrier height map is shown in Figure 6.7c, two distinct regions matching region I and region II of the current image are observed, with region I having a larger Φ_B than region II. In the map, the highest barrier height is about 0.55 eV, while the lowest one is around 0.38 eV. Combined with the STS results of Figure 6.5, we assign region I to be a defect-dominated area. In principle, the Schottky barrier height expected from the Schottky-Mott rule should be ~0.2 eV according to the following equation:

$$\Phi_B = W_m - \chi \quad (5)$$

The work function W_m of the tip is around 4.2 eV, and the electron affinity χ of the $HfSe_2$ is 4.0 eV.[8] The measured barrier height is larger than the expected value by about 0.18-0.35 eV. We attribute this discrepancy to partial Fermi level pinning. The difference in the Φ_B between region I and region II can be understood by the observed difference in the location of the CBM at the two regions (see the STM/STS measurements). The lower CBM (by about 0.2 eV) in region II leads to a smaller barrier height as compared to region I. Moreover, the ideality factors obtained in both regions are between 2-4, indicating that thermionic emission is not the sole contributor to the current, but tunnelling across the barrier also plays a role.

In order to investigate the partial Fermi level effect, we have investigated the charge transport characteristics for tips of different work function (PtSi of 4.8 eV and Pt of 5.6 eV). The Φ_B determined at the two regions for each tip are then plotted as a function of the work function, Figure 6.7d. The pinning factor is then quantified by the slope S of the curve, and given by

$$S = d\Phi_{\mathrm{B}}/dW_m \quad (6)$$

Here, S takes values between 0 and 1. S =1 indicates an unpinned interface and the Schottky-Mott rule is fully applicable. For S =0, the Φ_B is independent of the metal work function and the Fermi level is fully pinned. For S between 0 and 1 partial Fermi level pinning occurs. Here we found that in region I S is equal to 0.1, while in region II S is equal to 0.09, both of these values signify a strong Fermi level pinning. A similar behavior has been also observed in metal/MoS_2.[40, 41] Two mechanisms are suggested for the pinning effect in $HfSe_2$. Firstly, distortion of the crystal surface to a large extent results in a notable charge redistribution at the interface between $HfSe_2$ and the contact metal. This can reduce the width of Schottky barrier and enhance the orbital overlap, which could then cause the weak dependence of W_m on Φ_{B}. Secondly, the Se atom vacancies on $HfSe_2$ surface (see Figure 6.1g) that act as metallic defects can induce the formation of additional gap states, and subsequently strengthen the Fermi level pinning.

6.5 Effect of oxidation on $HfSe_2$ Surface

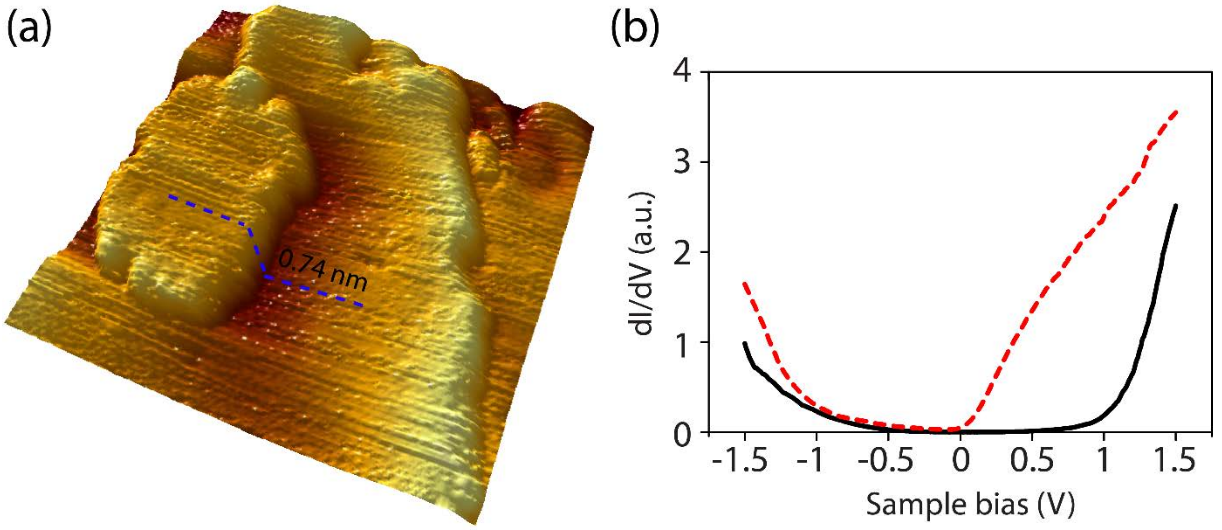

Figure 6.8. (a) Three dimensional (3D) image of $HfSe_2$ surface after air exposure for 2 days. The blue dashed line profiles the flake height, I_t= 0.6 nA, V_s= -2.5 V; (b) dI/dV spectra of the oxidized surface (black curve) and pristine $HfSe_2$ (red dashed curve) measured with the same STM tip, I_t= 0.4 nA , V_s= -1.5 V.

The oxidation of the $HfSe_2$ crystal was first investigated by STM. The 3D STM topography with a size of 25 nm×25 nm in Figure 6.8a presents the $HfSe_2$ surface after 2 days of air exposure. Small flakes with thickness of ~0.74 nm are readily found on the surface, i.e., a value about 0.13 nm larger than the interlayer distance of $HfSe_2$. The surface of the material appears to be much rougher than the freshly cleaved surface. Because of this roughness, atomic resolution imaging of the crystal's lattice was not possible. The *dI*/*dV* spectra recorded on the pristine and air-exposed $HfSe_2$ surfaces are shown in Figure 6.8b. The bandgap of the air exposed surface as measured by STS is about 2 eV, which is almost two times larger than that of $HfSe_2$. However, the expected bandgap of fully oxidized HfO_2 is about 5.8 eV.[42] This difference suggests that the outermost $HfSe_2$ layer is only partly oxidized and some of the Hf-Se bonds are still preserved.

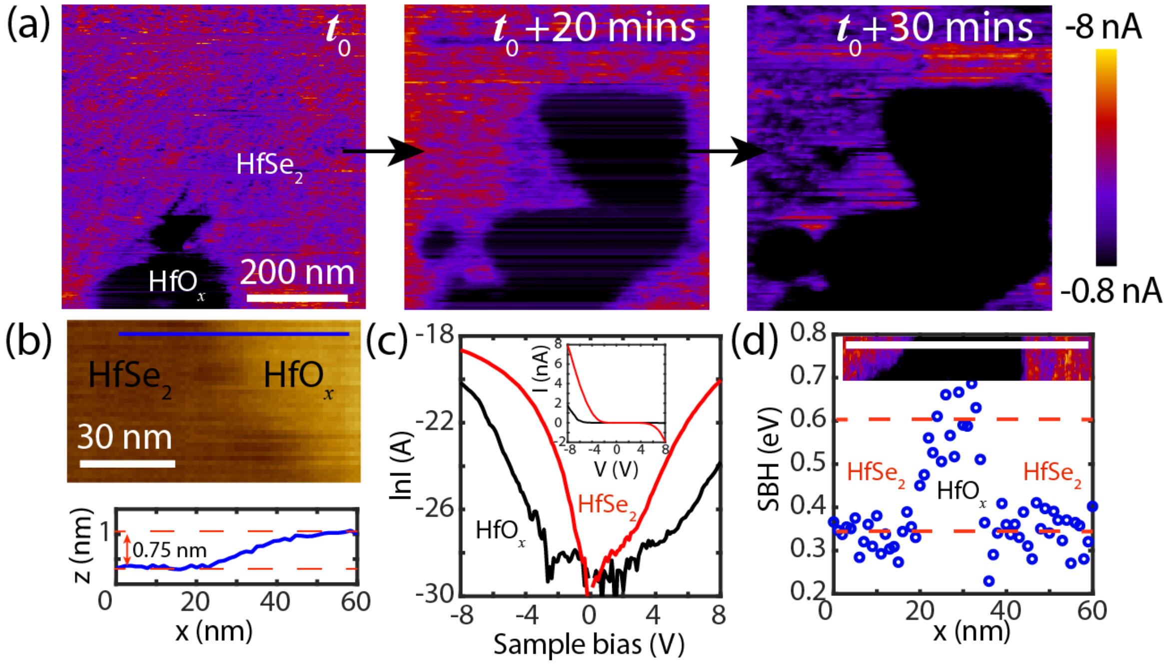

Figure 6.9. (a) The oxidation evolution of the HfSe$_2$ as measured with C-AFM, which are taken at t_o, t_o+20 mins and t_o+30 mins, respectively. The sample bias is 4.7 V (b) AFM topography of the transition between an unoxidized to an oxidized region. The blue line shows the apparent height of HfO$_x$ layer. (c) The semi-logarithmic contact I(V) curves for HfSe$_2$ and HfO$_x$. Inset: the corresponding contact I(V) curves. (d) Schottky barrier height cross section showing a HfSe$_2$-HfO$_x$-HfSe$_2$ transition.

The air stability of HfSe$_2$ was also investigated with C-AFM. In contrast to the UHV measurements in the STM experiments, the C-AFM measurements were done in a very low humidity-N$_2$ environment to exclude the influence from water.[43] The sample, however, is still exposed to a certain amount of oxygen allowing us to study in-situ the oxidation dynamics of the uppermost HfSe$_2$ layers. Figure 6.9a shows the time-dependent oxidation process of HfSe$_2$ during a C-AFM measurement. At t_0, a small oxidized area was detected at the bottom side of the image by the distinct current intensity, which was one order of magnitude lower than that of the pristine surface. After 20 minutes of scanning of the same region, the oxidized part has spread along all directions, as shown in the second panel of Figure 6.9a. At t_0+30 minutes, the oxidized region occupies more than half of the image. The height of the HfO$_x$ flake was measured to be around 0.75 nm, as shown in Figure 6.9b, in line with the STM result. The current-voltage characteristics averaged from several curves at the pristine and oxidized regions are shown in Figure 6.9c. As compared to the pristine HfSe$_2$, the oxidized regions are significantly less conductive most probably due to the larger bandgap of these regions. The

Schottky barrier height of this HfO_x layer is determined to be ~0.61 eV, i.e., about 44% larger than that of the unoxidized $HfSe_2$ surface. More importantly, the ideality factor across these two regions has increased from approximately 4 at the unoxidized region to about 20 at the oxidized region. This huge increase in the ideality factor suggests that the current is not solely due to thermionic emission, but that also tunneling plays an important role. To this regard, the oxidized upper flake may act as a tunneling barrier. The measured structural and electrical variations confirm the air-sensitivity of $HfSe_2$. $HfSe_2$-based devices operated at ambient conditions will require the use of a protective coating layer in order to avoid oxidation. Another approach is to use the uppermost layer as a dielectric layer, complete oxidation of the uppermost layer is expected to slow down the oxidation of the underlying layers. To that extent new device architectures need to be considered to account for the effects observed here.

6.6 Conclusions

In summary, $HfSe_2$ crystal surface has been investigated in detail by STM and C-AFM. Atomically resolved STM images of the surface lattice structure demonstrates a high density of intrinsic defects, located both in the Se layer and Hf layer. The surface distortion and high density of defects indicate a very poor quality of the $HfSe_2$ crystal, detrimental for many device applications. This poor quality most probably explains the low carrier mobilities found in $HfSe_2$-based field effect transistors. A prominent defect with a dim dark appearance, localized at the Hf-layer with a density of 5×10^{11} cm^{-2} locally increases the bandgap by about 25%, changing it from 1 eV to 1.25 eV. Moreover, the presence of defects reduces the local barrier height with metal contacts. Furthermore, the small dependence of the measured barrier height on the metal's work function indicates partial Fermi level pinning. We have also investigated the oxidation dynamics of $HfSe_2$. After exposure of the crystal to ambient conditions, we find that oxidized layers grow fast and have a bandgap of ~2 eV. The large increase of the Schottky barrier height and ideality factor of the oxidized parts when contacting with a metal tip, confirms our interpretation. Therefore, in order to obtain the predicted performance for $HfSe_2$-based electronic devices, the influence of defects and oxidation has to be well-controlled or eliminated.

Bibliography

[1] Radisavljevic, B.; Radenovic, A.; Brivio, J.; Giacometti, V.; Kis, A. Single-Layer MoS_2 Transistors. *Nat. Nanotechnol.* **2011**, *6*, 147-150.

[2] Butler, S. Z.; Hollen, S. M.; Cao, L.; Cui, Y.; Gupta, J. A.; Gutierrez, H. R.; Heinz, T. F.; Hong, S. S.; Huang, J.; Ismach, A. F., et al. Progress, Challenges, and Opportunities in Two-Dimensional Materials Beyond Graphene. *ACS Nano* **2013**, *7*, 2898-2926.

[3] Jariwala, D.; Sangwan, V. K.; Lauhon, L. J.; Marks, T. J.; Hersam, M. C. Emerging Device Applications for Semiconducting Two-Dimensional Transition Metal Dichalcogenides. *ACS Nano* **2014**, *8*, 1102-1120.

[4] Duong, D. L.; Yun, S. J.; Lee, Y. H. van der Waals Layered Materials: Opportunities and Challenges. *ACS Nano* **2017**, *11*, 11803-11830.

[5] Splendiani, A.; Sun, L.; Zhang, Y.; Li, T.; Kim, J.; Chim, C.; Galli, G.; Wang, F. Emerging Photoluminescence in Monolayer MoS_2. *Nano Lett.* **2010**, *10*, 1271-1275.

[6] Fang, Y.; Pan, J.; He, J.; Luo, R.; Wang, D.; Che, X.; Bu, K.; Zhao, W.; Liu, P.; Mu, G.; Zhang, H.; Lin, T.; Huang, F. Structure Re-Determination and Superconductivity Observation of Bulk 1T MoS_2. *Angew. Chem.* **2018**, *130*, 1246-1249.

[7] Chi, Z.; Chen, X.; Yen, F.; Peng, F.; Zhou, Y.; Zhu, J.; Zhang, Y.; Liu, X.; Lin, C.; Chu, S.; Li, Y.; Zhao, J.; Kagayama, T.; Ma, Y.; Yang, Z. Superconductivity in Pristine $2H_a$-MoS_2 at Ultrahigh Pressure. *Phys. Rev. Lett.* **2018**, *120*, 037002.

[8] Yue, R.; Barton, A. T.; Zhu, H.; Azcatl, A.; Pena, L. F.; Wang, J.; Peng, X.; Lu, N.; Cheng, L.; Addou, R., et al. $HfSe_2$ Thin Films: 2D Transition Metal Dichalcogenides Grown by Molecular Beam Epitaxy. *ACS Nano* **2015**, *9*, 474-480.

[9] Mleczko, M. J.; Zhang, C.; Lee, H. R.; Kuo, H.; Magyari-Kope, B.; Moore, R. G.; Shen, Z.; Fisher, I. R.; Nishi, Y.; Pop. $HfSe_2$ and $ZrSe_2$: Two-Dimensional Semiconductors with Native High-κ Oxides. *Sci. Adv.* **2017**, *3*, e1700481.

[10] Rasmussen, F. A.; Thygesen, K. S. Computational 2D Materials Database: Electronic Structure of Transition-Metal Dichalcogenides and Oxides. *J. Phys. Chem. C* **2015**, *119*, 13169-13183.

[11] Kang, M.; Rathi, S.; Lee, I.; Lim, D.; Wang, J.; Li, L.; Khan M. A.; Kim, G. Electrical Characterization of Multilayer $HfSe_2$ Field-Effect Transistors on SiO_2 Substrate. *Appl. Phys. Lett.* **2015**, *106*, 143108.

[12] Yin, L.; Xu, K.; Wen, Y.; Wang, Z.; Huang, Y.; Wang, F.; Shifa, T. A.; Cheng, R.; Ma, H.; He, J. Ultrafast and Ultrasensitive Phototransistors Based on Few-Layered $HfSe_2$. *Appl. Phys. Lett*. **2016**, *109*, 213105.

[13] Kang, M.; Rathi, S.; Lee, I.; Li, L.; Khan, M. A.; Lim, D.; Lee, Y.; Park, J.; Yun, S. J.; Youn, D.; Jun, C.; Kim, G. Tunable Electrical Properties of Multilayer $HfSe_2$ Field Effect Transistors by Oxygen Plasma Treatment. *Nanoscale* **2017**, *9*, 1645-1652.

[14] Zhang, W.; Huang, Z.; Zhang, W.; Li, Y. Two-Dimensional Semiconductors with Possible High Room Temperature Mobility. *Nano Res.* **2014**, *7*, 1731-1737.

[15] Zhou, W.; Zou, X.; Najmaei, S.; Liu, Z.; Shi, Y.; Kong, J.; Lou, J.; Ajayan, P. M.; Yakobson, B. I.; Idrobo, J. Intrinsic Structural Defects in Monolayer Molybdenum Disulfide. *Nano Lett*., **2013**, *13*, 2615-2622.

[16] Liu, H.; Zheng, H.; Yang, F.; Jiao, L.; Chen, J.; Ho, W.; Gao, C.; Jia, J.; Xie, M. Line and Point Defects in $MoSe_2$ Bilayer Studied by Scanning Tunneling Microscopy and Spectroscopy. *ACS Nano* **2015**, *9*, 6619-6625.

[17] Zhang, S.; Wang, C.; Li, M.; Huang, D.; Li, L.; Ji, W.; Wu, S. Defect Structure of Localized Excitons in a WSe_2 Monolayer. *Phys. Rev. Lett.* **2017**, *119*, 046101.

[18] Wu, Z.; Luo, Z.; Shen, Y.; Zhao, W.; Wang, W.; Nan, H.; Guo, X.; Sun, L.; Wang, X.; You, Y.; Ni, Z. Defects as a Factor Limiting Carrier Mobility in WSe_2: A Spectroscopic Investigation. *Nano Res.* **2016**, *9*, 3622-3631.

[19] McDonnell, S.; Addou, R.; Buie, C.; Wallace, R. M.; Hinkle, C. L. Defect-Dominated Doping and Contact Resistance in MoS_2. *ACS Nano* **2014**, *8*, 2880-2888.

[20] Liu, X.; Balla, I.; Bergeron, H.; Hersam, M. C. Point Defects and Grain Boundaries in Rotationally Commensurate MoS_2 on Epitaxial Graphene. *J. Phys. Chem. C* **2016**, *120*, 20798-20805.

[21] Bampoulis, P.; Bremen, R. V.; Yao, Q.; Poelsema, B.; Zandvliet, H. J. W.; Sotthewes, K. Defect Dominated Charge Transport and Fermi Level Pinning in MoS_2/Metal Contacts. *ACS Appl. Mater. Interfaces* **2017**, *9*, 19278-19286.

[22] Ghorbani-Asl, M.; Enyashin, A. N.; Kuc, A.; Seifert, G.; Heine, T. Defect-Induced Conductivity Anisotropy in MoS_2 Monolayers. *Phys. Rev. B* **2013**, *88*, 245440.

[23] Lin, Z.; Carvalho, B. R.; Kahn, E.; Lv, R.; Rao, R.; Terrones, H.; Pimenta, M. A.; Terrones, M. *2D Mater*. **2016**, *3*, 022002.

[24] Mirabelli, G.; McGeough, C.; Schmidt, M.; McCarthy, E. K.; Monaghan, S.; Povey, I. M.; McCarthy, M.; Gity, F.; Nagle, R.; Hughes, G.; Cafolla, A.; Hurley, P. K.; Duffy, R. Air Sensitivity of MoS_2, $MoSe_2$, $MoTe_2$, HfS_2, and $HfSe_2$. *J. Appl. Phys.* **2016**, *120*, 125102.

[25] Zou, K.; Hong, X.; Keefer, D.; Zhu, J. Deposition of High-Quality HfO_2 on Graphene and the Effect of Remote Oxide Phonon Scattering. *Phys. Rev. Lett.* **2010**, *105*, 126601.

[26] Addou, R.; Colombo, L.; Wallace, R. M. Surface Defects on Natural MoS_2. *ACS Appl. Mater. Interfaces* **2015**, *7*, 11921-11929.

[27] Addou, R.; Wallace, R. M. Surface Analysis of WSe_2 Crystals: Spatial and Electronic Variability. *ACS Appl. Mater. Interfaces* **2016**, *8*, 26400-26406.

[28] Lucovsky, G.; White, R. M. Infrared-Reflectance Spectra of Layered Group-IV and Group-VI Transition-Metal Dichalcogenides. *Phys. Rev. B* **1973**, *7*, 3859-3870.

[29] Schimmel, Th.; Fuchs, H.; Sander, R.; Lux-Steiner, M. Atomically Resolved STM Imaging of Ion-Bombarded WSe_2. *Ultramicroscopy* **1992**, *44*, 683-688.

[30] Matthes, Th. W.; Sommerhalter, Ch.; Rettenberger, A.; Bruker, P.; Boneberg, J.; Lux-Steiner, M. Ch.; Leiderer, P. *Appl. Phys. A* **1998**, *66*, S1007-S1011.

[31] Murata, H.; Kataoka, K.; Koma, A. Scanning Tunneling Microscope Images of Locally Modulated Structures in Layered Materials, MoS_2(0001) and $MoSe_2$(0001), Induced by Impurity Atoms. *Surf. Sci.* **2001**, *478*, 131-144.

[32] Inoue, A.; Komori, T.; Shudo, K. Atomic-Scale Structures and Electronic States of Defects on Ar^+-Ion Irradiated MoS_2. *J. Electron Spectrosc. Relat. Phenom.* **2013**, *189*, 11-18.

[33] Kobayashi, K. Scattering Theory of Subsurface Impurities Observed in Scanning Tunneling Microscopy. *Phys. Rev. B* **1996**, *54*, 17029.

[34] Whangbo, M. H.; Ren, J.; Magonov, S. N.; Bengel, H.;Parkinson, B. A.; Suna, A. On the Correlation Between the Scanning Tunneling Microscopy Image Imperfections and Point Defects ofLayered Chalcogenides 2H-MX_2 (M=Mo, W; X= S, Se). *Surf. Sci.* **1995**, *326*, 311−326.

[35] Ugeda, M. M.; Bradley, A. J.; Zhang, Y.; Onishi, S.; Chen, Y.; Ruan, W.; Ojeda-Aristizabal, C.; Ryu, H.; Edmonds, M. T.; Tsai, H., et al. Characterization of Collective Ground States in Single-Layer $NbSe_2$. *Nat. Phys.* **2016**, *12*, 92-97.

[36] Eknapakul, T.; Fongkaew, I.; Siriroj, S.; Jindata, W.; Chaiyachad, S.; Mo, S.-K.; Thakur, S.; Petaccia, L.; Takagi, H.; Limpijumnong, S.; Meevasana, W. Direct Observation of Strain-Induced Orbital Valance Band Splitting in $HfSe_2$ by Sodium Intercalation. *Phys. Rev. B* **2018**, *97*, 201104(R).

[37] Park, J. H.; Sanne, A.; Guo, Y.; Amani, M.; Zhang, K.; Movva, H. C. P.; Robinson, J. A.; Javey, A.; Robertson, J.; Banerjee, S. K.; Kummel, A. C. Defect Passivation of Transition Metal Dichalcogenides via a Charge Transfer van Der Waals Interface. *Sci. Adv.* **2017**, *3,* e1701661.

[38] Rak, Z.; Mahanti, S. D.; Mandal, K. C.; Fernelius, N. C. Electronic Structure of Substitutional Defects and Vacancies in GaSe. *J. Phys. Chem. Solids* **2009**, *70,* 344-355.

[39] Hertz, H. Über die berührung fester elastischer körper. *J. Reine Angew. Math.* ***1882***, *92*, 156–171.

[40] Das, S.; Prakash, A.; Salazar, R.; Appenzeller, J. Toward Low-Power Electronics: Tunneling Phenomena in Transition Metal Dichalcogenides. *ACS Nano* **2014**, *8*, 1681-1689.

[41] Kim, C.; Moon, I.; Lee, D.; Choi, M. S.; Ahmed, F.; Nam, S.; Cho, Y.; Shin, H.; Park, S.; Yoo, W. J. Fermi Level Pinning at Electrical Metal Contacts of Monolayer Molybdenum Dichalcogenides. *ACS Nano* **2017**, *11*, 1588-1596.

[42] Peacock, P. W.; Robertson, J. Band Offsets and Schottky Barrier Heights of High Dielectric Constant Oxides. *J. Appl. Phys.* **2002**, *92*, 4712-4721.

[43] Bampoulis, P.; Teernstra, V. J.; Lohse, D.; Zandvliet, H. J. W.; Poelsema, B. Hydrophobic Ice Confined between Graphene and MoS_2. *J. Phys. Chem. C* **2016**, *120,* 27079-27084.

Conclusions and Outlook

7.1 General conclusions

In this thesis, we have studied the structural and electronic properties of various 2D materials using scanning tunneling microscopy and scanning tunneling spectroscopy. Their intrinsic electronic properties are modified in various ways, such as stacking, hydrogenation, defects and coupling to substrate. The main conclusions of our work are:

In twisted bilayer graphene with a twist angle of 2.3^{o}, we have found two van Hove singularities that are located near the Fermi level. We have made spatial maps of the electronic structure. The spatial maps of the electronic structure reveal a honeycomb structure, rather than a triangular structure. The origin of this honeycomb structure is due to the fact that twisted bilayer is positioned on a Bernal stacked highly-oriented pyrolytic graphite substrate.

The deposition of Si on transition metal dichalcogenides, such as MoS_2 and WSe_2, does not result in the growth of silicene on the transition metal dichalcogenides surfaces, but rather to the intercalation of silicon between the transition metal dichalcogenide layers.

For the first time, we have successfully synthesized germanene on a band gap material (MoS_2), which paves the way towards the determination of the intrinsic properties of this novel 2D buckled Dirac material. We found compelling evidence for the existence of charge puddles in germanene grown on a MoS_2 substrate. These charge puddles are caused by charge-donating impurities in the MoS_2 substrate.

Hydrogenation of germanene, synthesized on Ge_2Pt nanocrystals, results in the opening of a bandgap of about 0.5 eV. This finding is an important step forward since a bandgap is a prerequisite for the realization of a germanene based field-effect transistor.

Finally, we have studied the structural and electronic properties of $HfSe_2$. This material possesses a high density of surface defects. This high density of defects in $HfSe_2$ degrade its electrical performance, and therefore the quality of $HfSe_2$ crystals should be carefully checked before using this material in device applications.

7.2 Outlook and recommendations

7.2.1 Twisted graphene

Twisted graphene layers can be found on highly-oriented pyrolytic graphite samples after cleavage. [1-3] In our work, we also use this method to produce twisted graphene layers. Another way to prepare twisted graphene layers is by growing graphene on 4H- or 6H- SiC substrates.[4] Also in this case there is no control over the exact twist angle of the graphene. In order to produce twisted bilayer graphene with a well-defined twist angle we have built a dry transfer set up. The twisted graphene bilayers are synthesized on a h-BN/SiO_2 substrate.[5] The setup we have built is shown in Figure 7.1a, and is referred to as 2D-transfer system. In Figure 7.1b two examples of a twisted bilayer graphene (with electrical contacts) are shown.

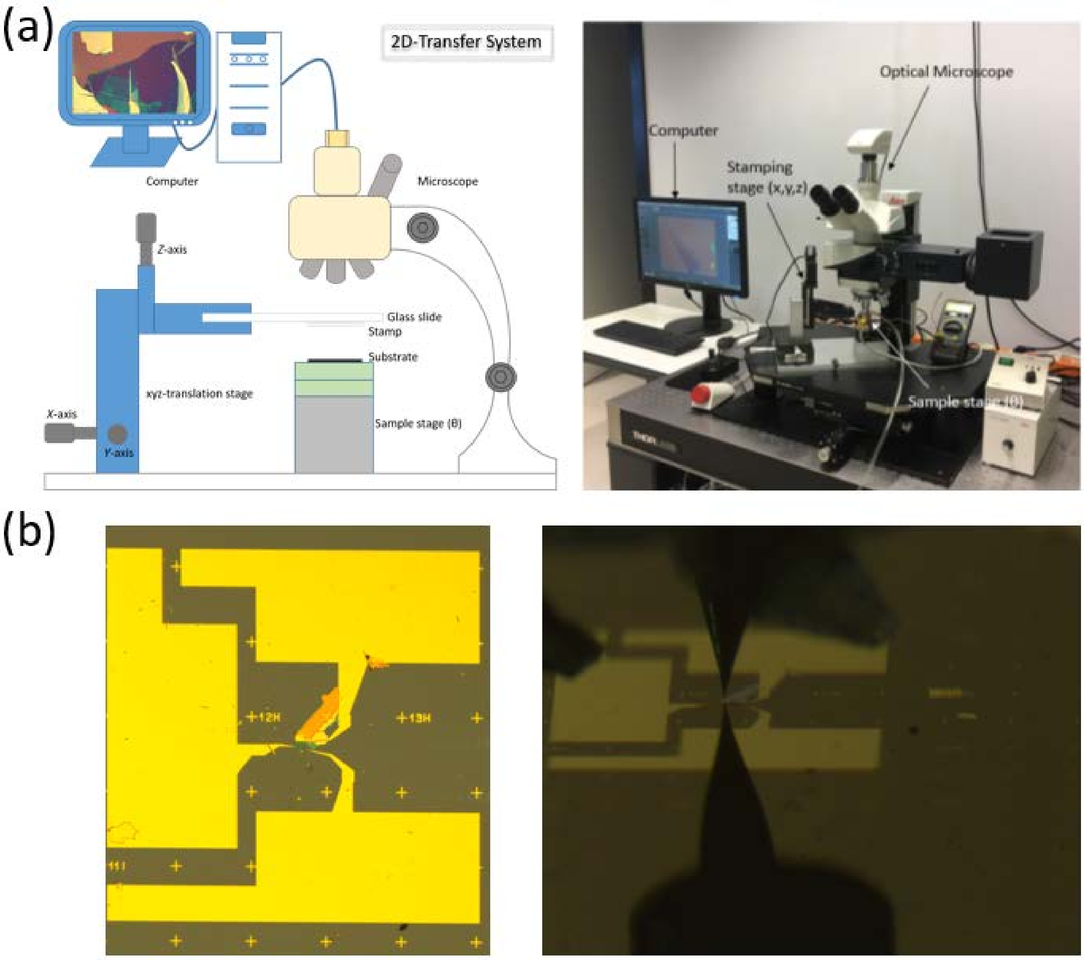

Figure 7.1: (a) Setup of the 2D-transfer system. (b) Images of twisted bilayer graphene with contacts. In the right panel the STM tip is visible.

7.2.2 Germanene

Germanene has been synthesized in two different ways. In the first route we deposited Pt on a Ge(110) substrate and make use of the eutectic phase, which occurs a ratio of 22% Pt and 78% Ge. Upon cooling down this eutectic phase separates in the two phases that are adjacent to the eutectic point in bulk phase diagram, i.e. the Ge_2Pt and Ge phases, respectively. Eventually we end up with micrometer sized Ge_2Pt clusters that are coated with a germanene layer. Although this system is interesting form a scientific viewpoint, the germanene coated Ge_2Pt crystals are far too small for any device application.

In the second route we deposit Ge on MoS_2, a transition metal dichalcogenide with a bulk bandgap of about 1.3 eV. Owing to the band gap of MoS_2, the electronic states of germanene in the vicinity of the Fermi level are decoupled from the underlying substrate. The presence of defects in the MoS_2 is essential since they are required for the nucleation of Ge islands. Unfortunately, these defects are often charged and thus lead to the formation of the charge inhomogeneities, i.e. charge puddles, in the germanene layer. These charge puddles have a negative effect on the electronic properties of germanene since they lead to reduction of the charge carrier mobilities.

We suggest to grow germanene on hexagonal boron nitride. Hexagonal boron nitride has a large bandgap of about 6 eV, is nearly defect-free and has a honeycomb lattice. In addition, the nearest-neighbor distance between the Ge atoms in the germanene honeycomb structure (2.5 Å) perfectly matches with the lattice constant of hexagonal boron nitride.

Bibliography

[1] Li, G.; Luican, A.; Lopes dos Santos, J. M. B.; Castro Neto, A. H.; Reina, A.; Kong, J.; Andrei, E. Y. Observation of Van Hove Singularities in Twisted Graphene Layers. *Nat. Phys.* **2010**, *6* (2), 109–113.

[2] Yin, L.; Qiao, J.; Wang, W., et al. Tuning Structures and Electronic Spectra of Graphene Layers with Tilt Grain Boundaries. *Phys. Rev. B* **2014**, *89*, 205410.

[3] Yin, L.; Qiao, J.; Zuo, W.; Li, W.; He, L. Experimental Evidence for Non-Abelian Gauge Potentials in Twisted Graphene Bilayers. *Phys. Rev. B* **2015**, *92*, 081406(R).

[4] Brihuega, I.; Mallet, P.; González-Herrero, H.; Trambly de Laissardière, G.; Ugeda, M. M.; Magaud, L.; Gómez-Rodríguez, J. M.; Ynduráin, F.; Veuillen, J.-Y. Unraveling the Intrinsic and Robust Nature of van Hove Singularities in Twisted Bilayer Graphene by Scanning Tunneling Microscopy and Theoretical Analysis. *Phys. Rev. Lett.* **2012**, *109* (19), 196802.

[5] Cao, Y.; Fatemi, V.; Fang, S.; Watanabe, K.; Taniguchi, T.; Kaxiras, E.; Jarillo-Herrero, P. Unconventional Superconductivity in Magic-Angle Graphene Superlattices. *Nature* **2018**, *556*, 43-50.

Summary

This thesis deals with the two-dimensional materials. Soon after the discovery of graphene, the first two-dimensional material, many other two-dimensional materials have been synthesized and characterized.

In chapter 3 we studied the structural and electronic properties of a twisted graphene. The top layer of Bernal stacked highly-oriented pyrolytic graphite sample was twisted by an angle of 2.3^{o}. This twist angle results in a moiré pattern with a periodicity of 6.2 nm. The twisted graphene layer has electronic properties that are distinctly different from that of a single layer graphene due to the nonzero interlayer coupling. The integrated differential conductivity spectrum exhibits two well-defined van Hove singularities, one located just above the Fermi level and the other just below the Fermi level. Spatial maps of the differential conductivity that are recorded at energies near the Fermi level exhibit a honeycomb structure that is comprised of two inequivalent hexagonal sublattices. For energies near the Fermi level the hexagonal structure in the differential conductivity maps vanishes. We have performed tight-binding calculations of the twisted graphene system using the propagation method, in which a third graphene layer is added to mimic the substrate. This third layer lowers the symmetry and explains the development of the two hexagonal sublattices in the moiré pattern. Our experimental results are in excellent agreement with the tight-binding calculations.

In chapter 4 and 5 we have studied the two novel elemental two-dimensional materials that are based on silicon and germanium, respectively. Owing to their sp^2 type of electronic structure the elements of the 'carbon' column of the periodic system i.e. silicon, germanium and tin are of particular of interest as potential two-dimensional materials. The silicon and germanium analogues of graphene are referred to as silicene and germanene, respectively, and share many properties with graphene. In thesis we have attempted to synthesize these materials. Silicon was deposited on WSe_2, a transition metal dichalcogenide with an indirect bandgap of about 1.2-1.3 eV. After the deposition of silicon the WSe_2 transform from an atomically flat substrate to a substrate that exhibit a hill-and-valley structure. Since the lattice constant of the corrugated WeS_2 substrate is exactly same as that of the flat substrate we conjectured that the deposited Si atoms have been intercalated between the WSe_2 layers. In order to validate this conjecture we have recorded spatial maps of *dI/dz*. The *dI/dz* signal is proportional to the square root of the work function and does not contain any topographic information. The homogeneous *dI/dz* map provides compelling evidence that the top layer is indeed pure WSe_2.

In chapter 5 we focus on the other elemental two-dimensional material, germanene. Germanene has been successfully synthesized on Ge_2Pt and MoS_2 substrates. The density of states of the germanene layer exhibits a well-defined V shape around the Fermi level, which hints to a two-dimensional Dirac system. We found that germanene grown on MoS_2 substrate exhibits charge puddles, analogous to the charge puddles which have been reported for graphene on SiO_2. By using the Dirac point mapping technique were able to map out the charge puddles in real space. The Dirac point varies from -30 meV to +15 meV for the germanene/MoS_2 system, corresponding to a charge density in the puddles in the range of 2.6×10^{-3} electrons to 6.6×10^{-4} holes per nm^2. The radius of these puddles is about 10-20 nm, resulting in a total charge of the order of one charge carrier per puddle. The defect concentration in the top layer of the MoS_2 substrate is very comparable to the density of charge puddles, suggesting that the charge puddles are caused by the charged defects in the top layer of the MoS_2 substrate. In addition, we have studied the hydrogenation of germanene synthesized on Ge_2Pt crystals using scanning tunneling microscopy and spectroscopy. The germanene honeycomb lattice is buckled and consists of two hexagonal sub-lattices that are slightly displaced with respect to each other. The hydrogen atoms adsorb exclusively on the Ge atoms of the upward buckled hexagonal sub-lattice. At a hydrogen exposure of about 100 L, the (1×1) buckled honeycomb structure of germanene converts to a (2×2) structure. Scanning tunneling spectra recorded on this (2×2) structure reveal the opening of a bandgap of about 0.2 eV. A fully (half) hydrogenated germanene surface is obtained after an exposure of about 9000 L hydrogen. The hydrogenated germanene, also referred to as germanane, has a sizeable bandgap of about 0.5 eV and is slightly n-type.

In chapter 6, the defects and air-stability of hafnium diselenide ($HfSe_2$) have been studied. $HfSe_2$ is a very appealing material for field-effect based applications owing to its moderate band gap of about 1 eV and its high-κ dielectric native oxide. Unfortunately, the experimentally determined charge carrier mobility is about 3 orders of magnitude lower than the theoretically predicted value. This strong deviation calls for a detailed investigation of the physical and electronic properties of $HfSe_2$. Here, we have studied the structure, density, and density of states of several types of defects that are abundant on the $HfSe_2$ surface using scanning tunneling microscopy and spectroscopy. Compared to MoS_2 and WSe_2, $HfSe_2$ exhibits similar type of defects, albeit with a substantially higher density of 9×10^{11} cm^{-2}. The most abundant defect is a subsurface defect, which shows up as a dim feature in scanning tunneling microscopy images. These dim dark defects have a substantially larger band gap (1.25 eV) than the pristine surface

(1 eV), suggesting a substitution of the Hf atom by another atom. The high density of defects on the $HfSe_2$ surface leads to very low Schottky barrier heights. Conductive atomic force microscopy measurements reveal a very small dependence of the Schottky barrier height on the work function of the metals, suggesting a strong Fermi-level pinning. We attribute the observed Fermi-level pinning (pinning factor ∼0.1) to surface distortions and Se/Hf defects. In addition, we have also studied the $HfSe_2$ surface after the exposure to air by scanning tunneling microscopy and conductive atomic force microscopy. Partly oxidized layers with bandgaps of 2 eV and Schottky barrier heights of ∼0.6 eV were readily found on the surface. Our experiments reveal that $HfSe_2$ is very air-sensitive, implying that capping or encapsulating of $HfSe_2$, in order to protect it against oxidation, is a necessity for technological applications.

Samenvatting

In dit proefschrift heeft betrekking op tweedimensionale materialen. Kort na de ontdekking van grafeen, het eerste tweedimensionale materiaal, zijn vele andere tweedimensionale materialen gesynthetiseerd en gekarakteriseerd. In dit proefschrift zullen we een aantal van deze nieuwe tweedimensionale materialen onder de loep nemen.

In hoofdstuk 3 hebben we de structurele en elektronische eigenschappen van gedraaid grafeen bestudeerd. De bovenste laag van Bernal gestapeld hoog-georiënteerd pyrolytisch grafietmonster werd gedraaid met een hoek van 2,3°. Deze draaihoek resulteert in een moiré-patroon met een periodiciteit van 6,2 nm. De gedraaide grafeenlaag heeft elektronische eigenschappen die duidelijk verschillen van die van een enkele laag grafeen vanwege de koppeling tussen de lagen. Het geïntegreerde differentiële geleidbaarheidsspectrum (dI/dV) vertoont twee goed gedefinieerde van Hove-singulariteiten, één die zich net boven het Fermi-niveau bevindt en de andere vlak onder het Fermi-niveau. Ruimtelijke maps van de differentiële geleidbaarheid die worden geregistreerd bij energieën nabij het Fermi-niveau vertonen een honingraatstructuur die bestaat uit twee ongelijke hexagonale subroosters. Voor energieën in de buurt van het Fermi-niveau verdwijnt de hexagonale structuur in de maps van differentiële geleidbaarheid. We hebben tight-binding berekeningen uitgevoerd aan het gedraaide grafeensysteem met behulp van de propagatiemethode, waarbij een derde grafeenlaag wordt toegevoegd om het substraat na te bootsen. Deze derde laag verlaagt de symmetrie en verklaart de ontwikkeling van de twee hexagonale subroosters in het moiré-patroon. Onze experimentele resultaten zijn in uitstekende overeenstemming met de tight-binding berekeningen.

In hoofdstuk 4 en 5 hebben we de twee nieuwe elementaire tweedimensionale materialen bestudeerd die respectievelijk zijn gebaseerd op silicium en germanium. Vanwege hun sp^2 type elektronische structuur zijn de elementen van de 'koolstof' kolom van het periodieke systeem, d.w.z. silicium en germanium, interessant als potentiële tweedimensionale materialen. De grafeen-achtige allotropen van silicium en germanium worden respectievelijk aangeduid als siliceen en germaneen en delen veel eigenschappen met grafeen. In het proefschrift hebben we geprobeerd deze materialen te synthetiseren. Silicium werd gedeponeerd op WSe_2, een overgangsmetaal dichalcogenide met een indirecte bandgap van ongeveer 1.2-1.3 eV. Na de depositie van silicium transformeert het WSe_2 van een atomair vlak substraat naar een substraat dat een heuvel-en-dal structuur vertoont. Omdat de roosterconstante van het gegolfde WeS_2 substraat exact hetzelfde is als die van het vlakke substraat, veronderstelden we dat de gedeponeerde Si-atomen tussen de WSe_2 lagen zijn geïntercaleerd. Om dit vermoeden te valideren, hebben we ruimtelijke maps van dI/dz opgenomen. Het dI/ z-signaal is evenredig met de wortel van de werkfunctie en bevat geen topografische informatie. De homogene dI/dz-map biedt overtuigend bewijs dat de bovenste laag inderdaad puur WSe_2 is.

In hoofdstuk 5 concentreren we ons op het andere elementaire tweedimensionale materiaal, germaneen. Germaneen is met succes gesynthetiseerd op Ge_2Pt en MoS_2 substraten. De dichtheid van toestanden van de germaneenlaag vertoont een goed gedefinieerde V-vorm rond het Fermi-niveau, die hint naar een tweedimensionaal Dirac-systeem. We ontdekten dat germeen gegroeid op MoS_2-substraat charge puddles vertoont, analoog aan decharge puddles die zijn gerapporteerd voor grafeen op SiO_2. Door het gebruik van de Dirac-punt mappingstechniek konden de charge puddles ruimtelijk in kaart worden gebracht. Het Dirac-punt varieert van -30 meV tot +15 meV voor het germaneen / MoS_2-systeem, wat overeenkomt met een ladingsdichtheid in de charge puddles in het bereik van 2.6×10^{-3} elektronen tot 6.6×10^{-4} gaten per m^2. De straal van deze charge puddles is ongeveer 10-20 nm, wat resulteert in een totale lading in de orde van één ladingsdrager per puddle. De defectconcentratie in de toplaag van het MoS_2 substraat is zeer vergelijkbaar met de dichtheid van charge puddles, hetgeen suggereert dat de charge puddles worden veroorzaakt door de geladen defecten in de toplaag van het MoS_2 substraat. Daarnaast hebben we de hydrogenering van germaneen gesynthetiseerd op Ge_2Pt kristallen bestudeerd met behulp van scanning tunneling microscopie en spectroscopie. Het germaneen honingraatrooster is buckled en bestaat uit twee zeshoekige subroosters die enigszins ten opzichte van elkaar zijn verplaatst. De waterstofatomen adsorberen exclusief op de Ge-atomen van het opwaarts gebuckled zeshoekige subrooster. Bij een waterstofblootstelling van ongeveer 100 L zet de (1 x 1) gebuckled honingraatstructuur van germaneen zich om in een (2 × 2) structuur. Scanning tunneling spectra die zijn opgenomen op deze (2 × 2) structuur onthullen de opening van een bandgap van ongeveer 0,2 eV. Een volledig (half) gehydrogeneerd germaneenoppervlak wordt verkregen na een blootstelling van ongeveer 9000 L aan waterstof. Het gehydrogeneerde germaneen, ook aangeduid als germanaan, heeft een aanzienlijke bandgap van ongeveer 0.5 eV en is enigszins n-type.

In hoofdstuk 6 zijn de defecten en luchtstabiliteit van hafniumdiselenide ($HfSe_2$) bestudeerd. $HfSe_2$ is een zeer aantrekkelijk materiaal voor toepassingen op basis van veldeffecten dankzij de moderate bandgap van ongeveer 1 eV en het hoge K-diëlektrische natuurlijke oxide. Helaas is de experimenteel bepaalde ladingdragersmobiliteit ongeveer 3 ordes van grootte lager dan de theoretisch voorspelde waarde. Deze sterke afwijking vereist een gedetailleerd onderzoek van de fysieke en elektronische eigenschappen van $HfSe_2$. Hier hebben we de structuur, dichtheid en dichtheid van toestanden van verschillende soorten defecten bestudeerd die overvloedig aanwezig zijn op het $HfSe_2$ oppervlak met behulp van scanning tunneling microscopie en spectroscopie. Vergeleken met MoS_2 en WSe_2 vertoont $HfSe_2$ soortgelijke type defecten, zij het met een aanzienlijk hogere dichtheid van 9×10^{11} cm^{-2}. Het meest voorkomende defect is een subsurface defect, dat zich voordoet als een dim protusion in e tunneling microscopiebeelden. Deze zwakke donkere defecten hebben een aanzienlijk grotere bandafstand (1.25 eV) dan het oorspronkelijke oppervlak (1 eV), wat duidt op een substitutie van het Hf-atoom door een ander atoom. De hoge dichtheid van defecten op het $HfSe_2$ oppervlak leidt tot zeer lage Schottky-barrièrehoogten. Geleidende atomaire krachtmicroscopie metingen onthullen een zeer kleine afhankelijkheid van de Schottky-barrièrehoogte op de werkfunctie van de metalen, wat duidt op een sterke fixatie op Fermi-niveau. We schrijven de waargenomen Fermi-level pinning (pinning factor ~0.1) toe aan oppervlaktevervormingen en Se/Hf defecten. Daarnaast hebben we ook het $HfSe_2$ oppervlak bestudeerd na blootstelling aan lucht gebuikmakend van scanning tunneling microscopie en geleidende atomaire krachtmicroscopie. Gedeeltelijk geoxideerde lagen met bandafstanden van 2 eV en Schottky barrièrehoogtes van ~ 0.6 eV werden gevonden op het oppervlak. Onze experimenten laten zien dat $HfSe_2$ zeer luchtgevoelig is, wat betekent dat het bedekken of coaten van $HfSe_2$, om het te beschermen tegen oxidatie, een noodzaak is voor technologische toepassingen.

List of publications

- **Q. Yao**, Z. Jiao, P. Bampoulis, L. Zhang, A. N. Rudenko, M. I. Katsnelson, H. J. W. Zandvliet. *Charge Puddles in Germanene*. Applied Physics Letters 114, 041601 (2019).
- **Q. Yao**, L. Zhang, P. Bampoulis, and H. J. W. Zandvliet. *Nanoscale Investigation of Defects and Oxidation of* $HfSe_2$. The Journal of Physical Chemistry C 122, 25498 (2018).
- **Q. Yao**, L. Zhang, N. S. Kabanov, A. N. Rudenko, T. Arjmand, H. Rahimpour Soleimani, A. L. Klavsyuk, and H. J. W. Zandvliet. *Bandgap opening in hydrogenated germanene*. Applied Physics Letters 112, 171607 (2018).
- **Q. Yao**, R. van Bremen, G. J. Slotman, L. Zhang, S. Haartsen, K. Sotthewes, P. Bampoulis, P. L. de Boeij, A. van Houselt, S. Yuan, and H. J. W. Zandvliet. *Spatially resolved electronic structure of twisted graphene*. Physical Review B 95, 245116 (2017).
- **Q. Yao**, R. van Bremen, and H. J. W. Zandvliet. *Growth of silicon on tungsten diselenide*. Applied Physics Letters 109, 243105 (2016).
- R. van Bremen*, **Q. Yao***, S. Banerjee, D. Cakir, N. Oncel, and H. J. W. Zandvliet. *Intercalation of Si Between* MoS_2 *Layers*. Beilstein Journal of Nanotechnology 8, 1952 (2017).
- L. Zhang, P. Bampoulis, A. N. Rudenko, **Q. Yao**, A. van Houselt, B. Poelsema, M. I. Katsnelson, and H. J. W. Zandvliet. *Structural and Electronic Properties of Germanene on* MoS_2. Physical Review Letters 116, 256804 (2016).
- P. Bampoulis, R. van Bremen, **Q. Yao**, B. Poelsema, H. J. W. Zandvliet, K. Sotthewes. *Defect Dominated Charge Transport and Fermi Level Pinning in* MoS_2*/Metal Contacts*. ACS Applied Materials & Interfaces 9, 19278 (2017).
- Z. Jiao, **Q. Yao**, L. M. Balescu, Q. Liu, B. Tang, H. J. W. Zandvliet. *Structural and electronic properties of the α-GeSe surface*. Surface Science 686, 17 (2019).
- P. Bampoulis, L. Zhang, Q. Yao, R. van Breman, C. J. Walhout, A. Acun, A. van Houselt, and H. J. W. Zandvliet. *Germanene: Silicene's twin sister*. (Book Chapter, Silicene: prediction, synthesis, application, 255-267).

Acknowledgements

This thesis would not be possible without the help and support of many individuals, to whom I owe my gratitude. In this part, I would like to thank and acknowledge them for their support, collaboration and comfort.

First of all, I would like to express my sincere thanks from the bottom of my heart to my supervisor Prof. Harold Zandvliet. Harold, I truly appreciate the opportunity you gave to me to join PIN group as a PhD student and continuous support throughout my PhD study. Thank you so much for giving me the freedom and trust to carry out my ideas and for giving me courage to go on. Your immense knowledge, patience, and considerate behavior impressed me a lot. Your guidance helped me in all the time of research and writing of this thesis. I could not have imagined having a better supervisor for my PhD study.

I would also like to thank a lot to the other staff in PIN group. Dr. Arie, thank you so much for your kind help in the last four years. It is my pleasure that you are also the committee member of my defense. I like your jokes always although I did not totally understand them sometimes. Dr. Kai, your encouragement and helps impressed me a lot, many thanks to such a gentle man. Dr. Stefan, I really enjoyed the group outing you arranged together with other committee members (Kai and Simone) each time. I got a lot of fun from all the nice trips, thank you very much. Martin and Hans, the technical staff of the group, thanks to both of you for your innumerable help to order the experimental materials and fix the experimental devices. I appreciate your trouble-shooting in the lab, since I am often a trouble-maker. I would like to thank Simone, the secretary of the group, for her care and help in the past four years.

Prof. B. Poelsema, Prof. M.A. Stöhr, Prof. O. Gurlu, Prof. J.W.M. Hilgenkamp and Prof. J.E. ten Elshof: I would like to thank you for agreeing to be members of my graduation committee and thoroughly reviewing my thesis.

I would like to acknowledge the China Scholar Council for the financial support of this research.

I thank my following group colleagues for the scientific and non-scientific discussions, and for all the fun we have had in the last four years. I acknowledge Rik and Xingchen to be my paranymphs.

Rik, thanks for the fruitful and fun collaboration. I really enjoy working and having sports with you. We had a lot of fun from tennis, badminton, beach volleyball and ping-pong. I am always happy when I do the experiments together with you and Dr. Kai, because I know we are going to make our experimental plan be true. Thank you so much for your help with LT-STM measurement. I wish you all the best.

Xingchen, as a master student, you are smart and hard-working. I appreciate having you as my student. Since you have a chance to start your PhD career, I would like to express my best wishes to you.

Lijie, many thanks for the care and fruitful collaboration during my first two years in PIN group. I still remember that we had a wonderful trip in Italy after the graphene conference in Genoa. I wish your family to grow and always be happy. Zhen and Zhiguo, my fellow countrymen, thank you very much for your help in Enschede, and I hope you will publish a lot of nice papers in PIN group and wish both of you to enjoy your life of study abroad.

My utmost appreciation goes to Edwin, Pantelis, Adil, Özlem, Tabassom, Nikolai, Carolien, Wojciech, Martina, Jorn, Gerjan, Thomas, Ruben, Maarten, Daniel, Valent, and all the past and present members of PIN group, for helpful and pleasant working environment.

Thanks to my friends, Lianci in Utrecht University, Yan in Queen Mary University of London and Mengjiao in RWTH Aachen University, for all the happy time we had together. We knew each other and became friends in China. I truly appreciate our friendship. Thank you so much and best wishes to all of you.

I would also like to thank the Chinese friends I meet in Enschede, Qian Li, Shu Zhang, Shuqin Cao, Chuan Li, Shuijing Jie, Jianfeng Huang, Jun Wang, Yan Liu, Yang Wang, Sizhao Huang, Zhengchao Guo and many more, for all the moments we have shared.

I want to thank my parents, Tingbo and Lianxiang, and my sister, Qijiao, for their comfort, support and unconditional love. I would also like to take this opportunity to express my gratitude to my uncle, Tingwu. Without your help, I maybe even did not have the chance to study further after my primary school.

At last, my deepest gratitude goes to my girlfriend, Zhenping. I appreciate everything you did for me. I feel lucky to have you in my life. Thank you very much for everything!